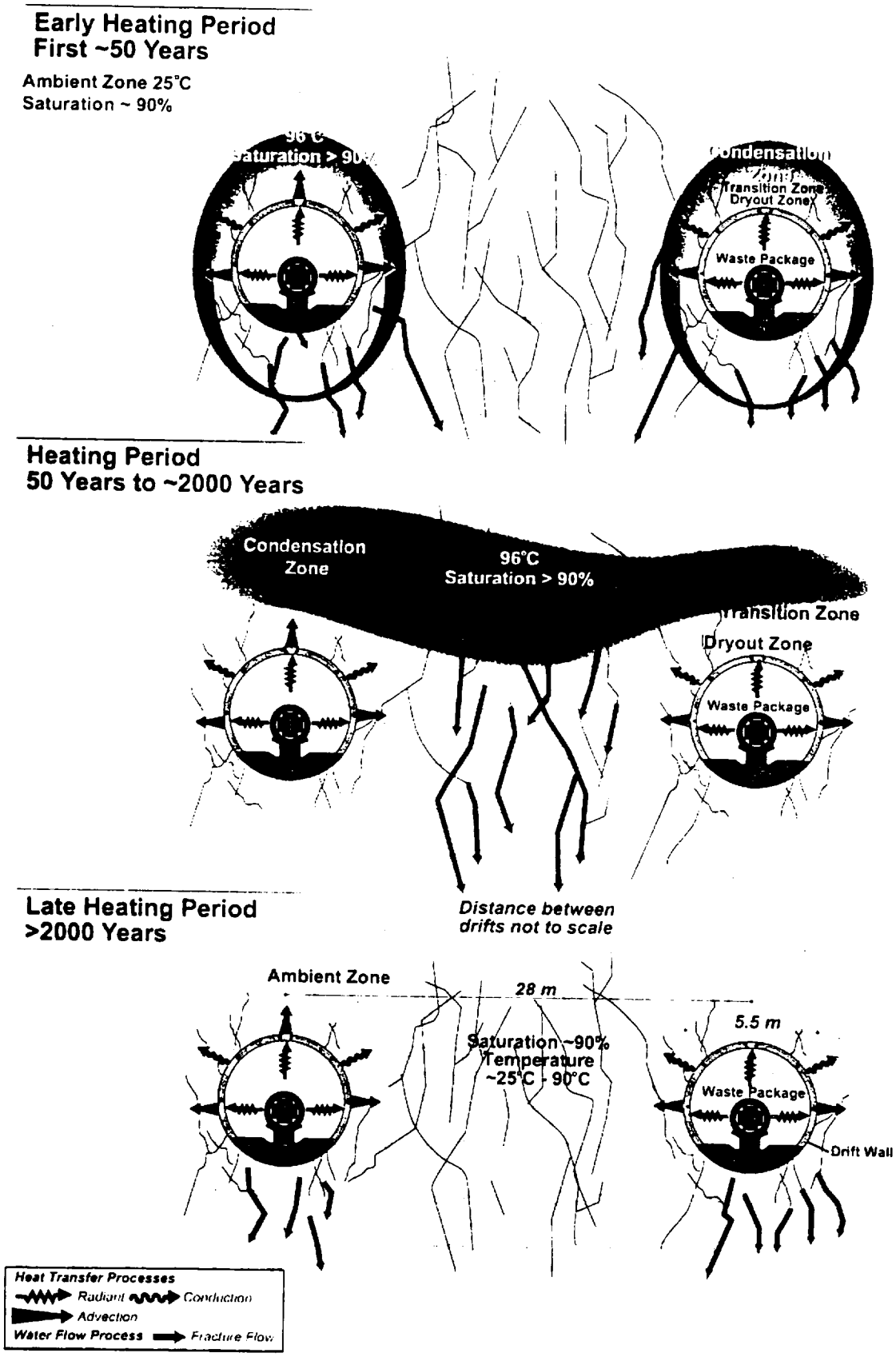

Figure 3-1. Conceptual diagram of TH processes at three stages (not to scale).

98Φ917Φ113 - Part 2

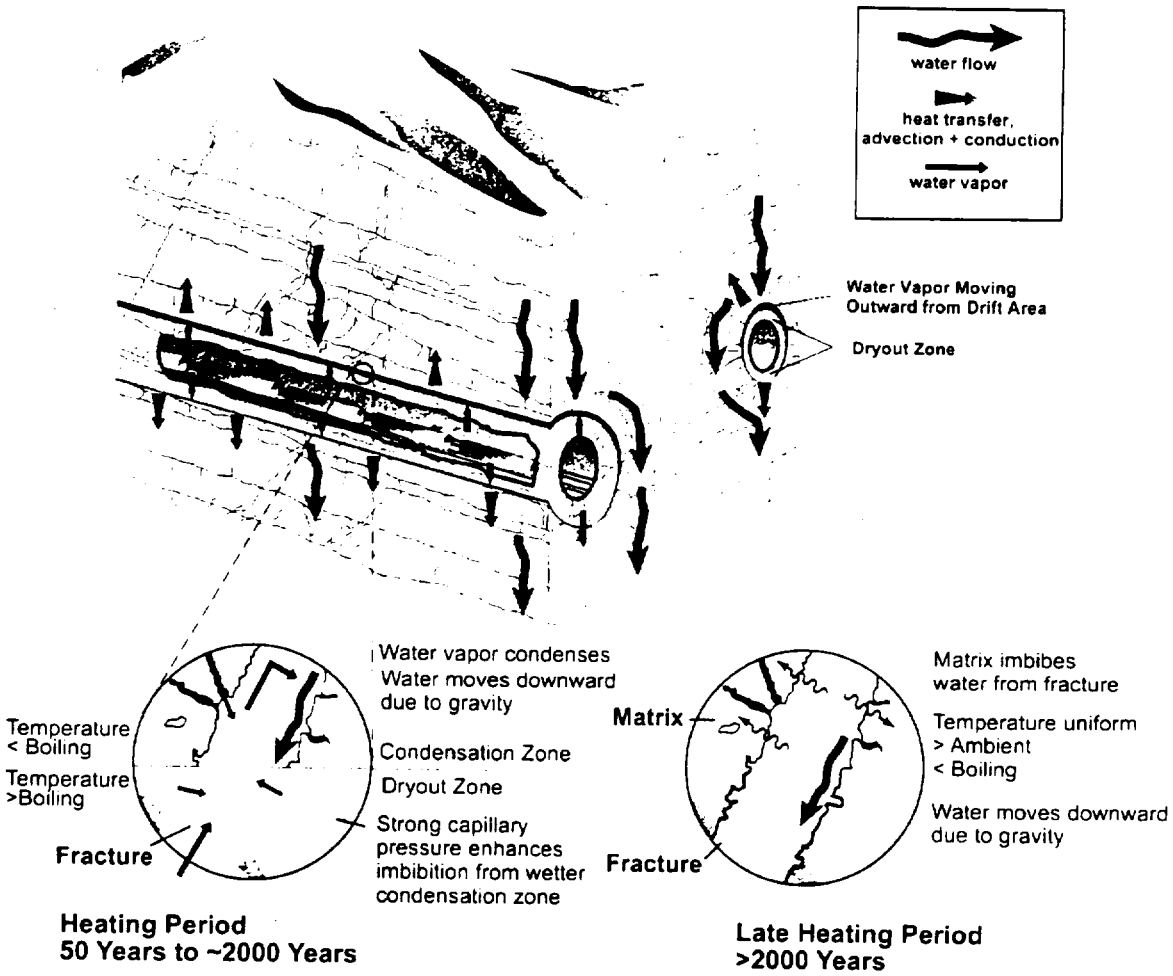

Figure 3-2. Conceptual diagram of water mass transfer processes in the above and below boiling zones.

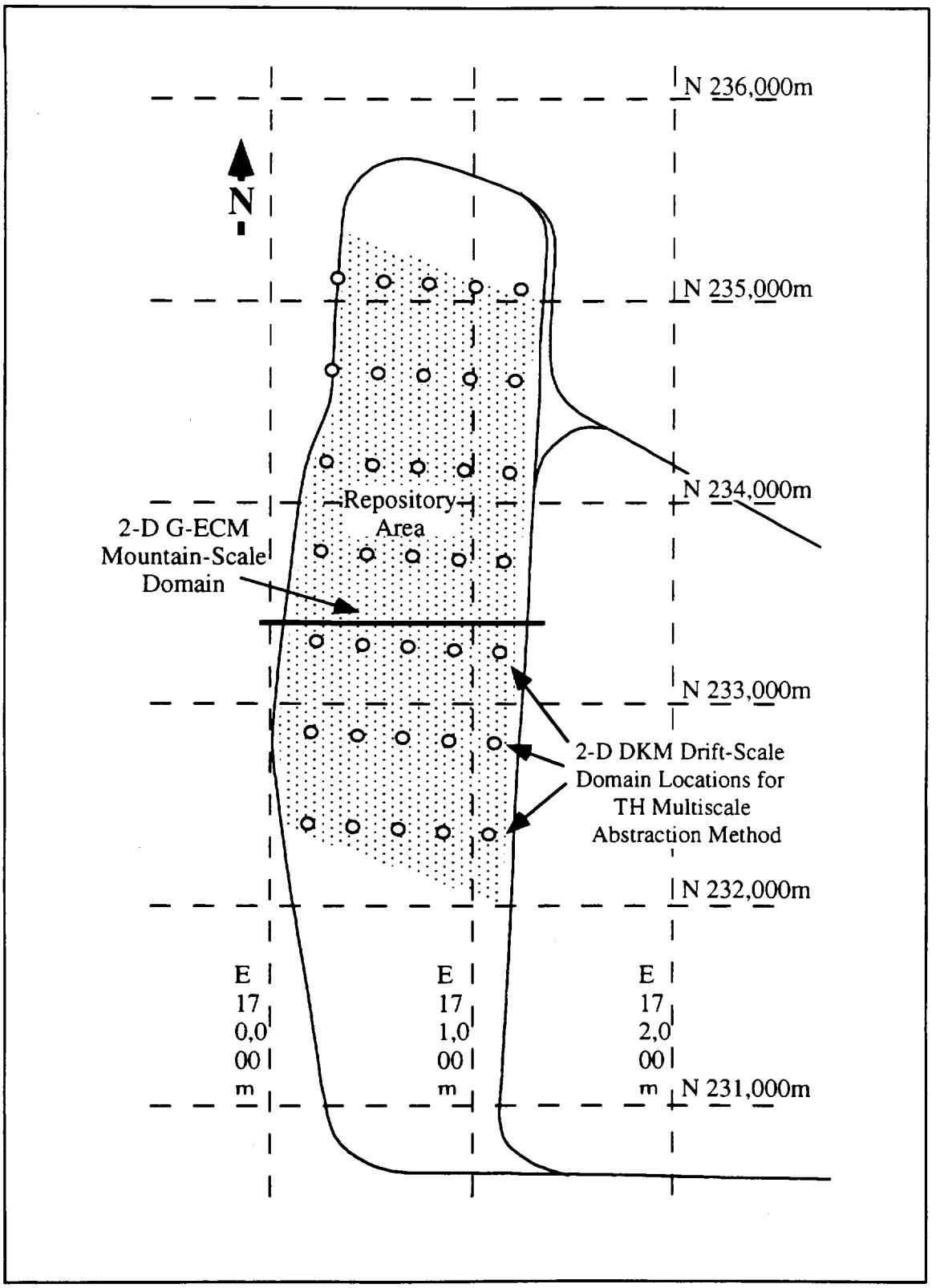

Figure 3-3. Repository layout and locations of several Performance Assessment (PA) TH models.

Mountain-Scale Thermal Hydrology

- *Repository edge effects*
- *Repository center effects*
- *Generalized Equivalent Continuum Flow Model (reduced matrix saturation)*

Unsaturated Zone Flow
- Climate
- Infiltration
- Hydrologic properties

Subsurface Design

Waste Package Design

Inputs

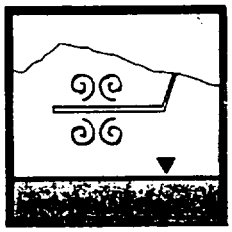

Outputs

Near-Field Geochemical Environment
- Air mass fraction
- Gas phase mass flux

- Thermal properties from laboratory measurements
- Single-heater-test results

Model Confidence Foundation

Drift-Scale Thermal Hydrology

- *Waste package variability*
- *Dual-Permeability Flow Model*
- *Comparison with Generalized Equivalent Continuum Model*

Unsaturated Zone Flow
- Climate
- Infiltration
- Hydrologic properties

Subsurface Design

Waste Package Design

Inputs

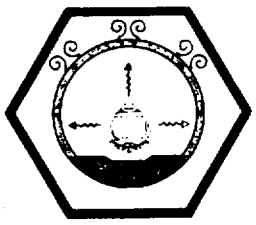

Outputs

Near-Field Geochemical Environment
- Drift-wall temperature

Waste Package Degradation
- Waste package temperature
- Waste package relative humidity

Waste Form Degradation
- Waste package temperature

Engineered Barrier System Transport
- Invert liquid saturation

- Thermal properties from laboratory measurements
- Single-heater-test results
- Comparison with independent model

Model Confidence Foundation

Figure 3-4. Coupling of TH to other TSPA-VA components.

3-D SMT Process Model

- Mountain-scale effects of rock and topography.
- No water or gas effects

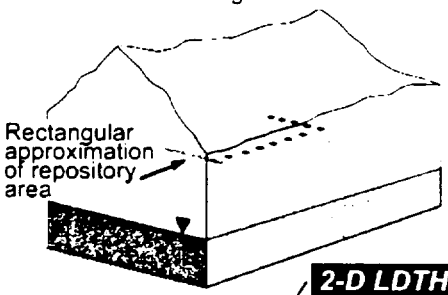

2-D LDTH Process Model

- Adds water and gas effects

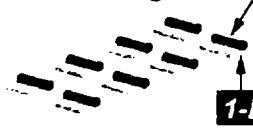

1-D SDT Process Model

- At each of 35 locations, LDTH and SDT models are run
  Results are compared between
- models
  SMT heat is adjusted
- using the results.

3-D LMTH Abstraction

- Mountain-scale effects of rock and topography
- Gas and water effects
- Heat discretized into cylinders averaged over several packages

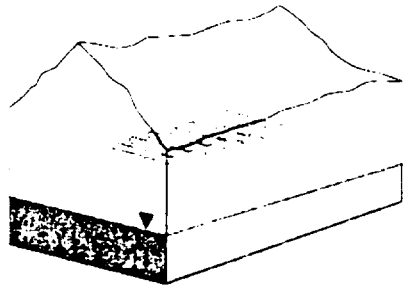

3-D DDT Process Model

- Discretizes heat distribution at the individual package level
- See Figure 3.2-4 for heat distribution

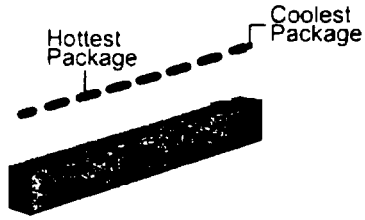

3-D DMTH Abstraction

- Mountain-scale effects of rock and topography
- Gas and water effects
- Discretizes heat distribution at the individual package level

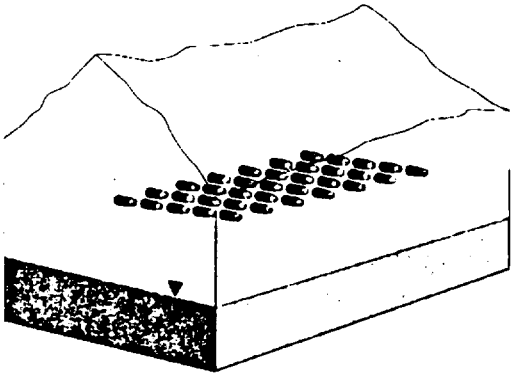

Table of Model Attributes

		Areal Distribution of Heat			Scale		Heat Transfer Mechanisms		
		Smeared Plate	Smeared Line	Discrete Waste Package	Drift	Mountain	Conduction	Radiation	Advection Water, Gas
Process Model	SMT	✓				✓	✓		
	SDT	✓			✓		✓		
	LDTH		✓		✓		✓	✓	✓
	DDT			✓	✓		✓	✓	
Abstraction	LMTH		✓			✓	✓	✓	✓
	DMTH			✓		✓	✓	✓	✓

Model Acronym
1st letter = Areal distribution of heat smeared or discrete
2nd letter = Scale: mountain or drift
3rd letter = Thermal
4th letter = Includes hydrology = H

Figure 3-5. The submodels used in the TH multiscale modeling and abstraction method

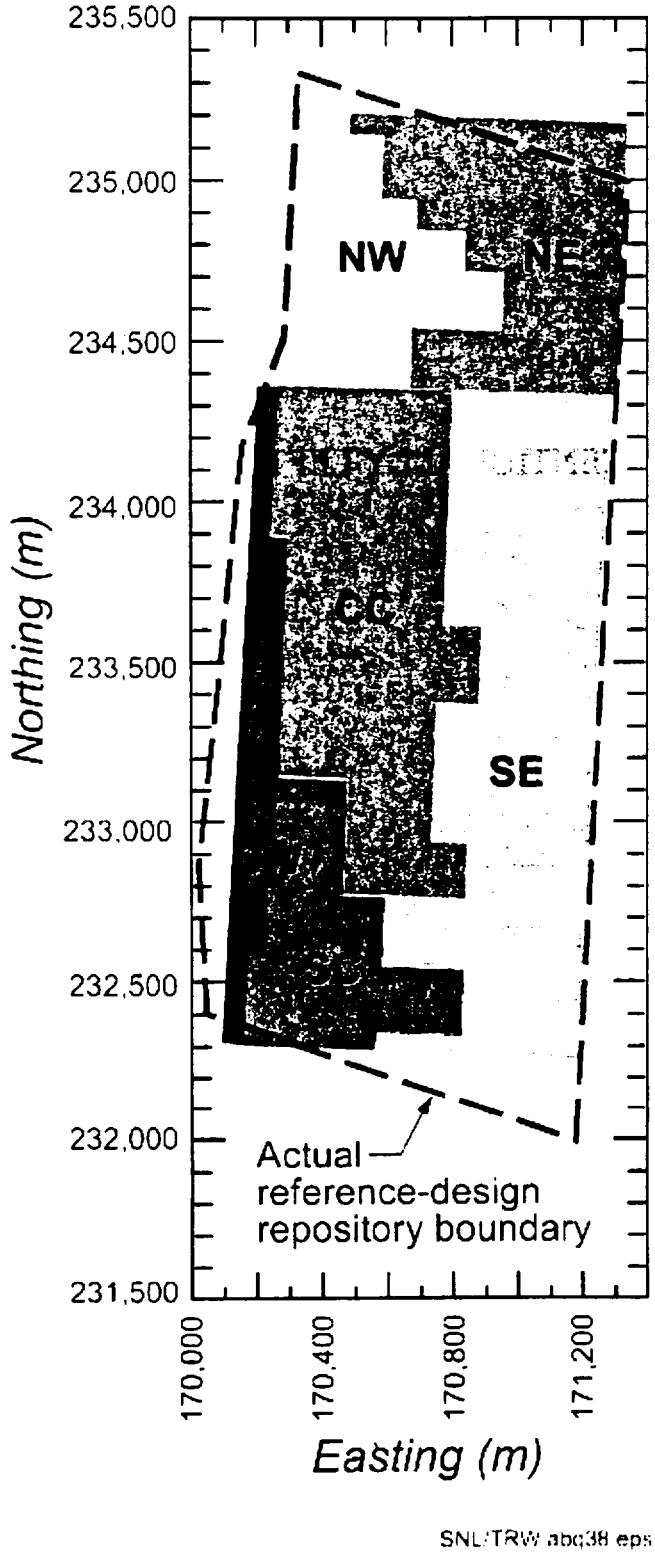

Figure 3-6. The dashed line shows the actual reference-design repository boundary; the solid lines show the idealization of the repository by a rectangle and the division into six repository subregions.

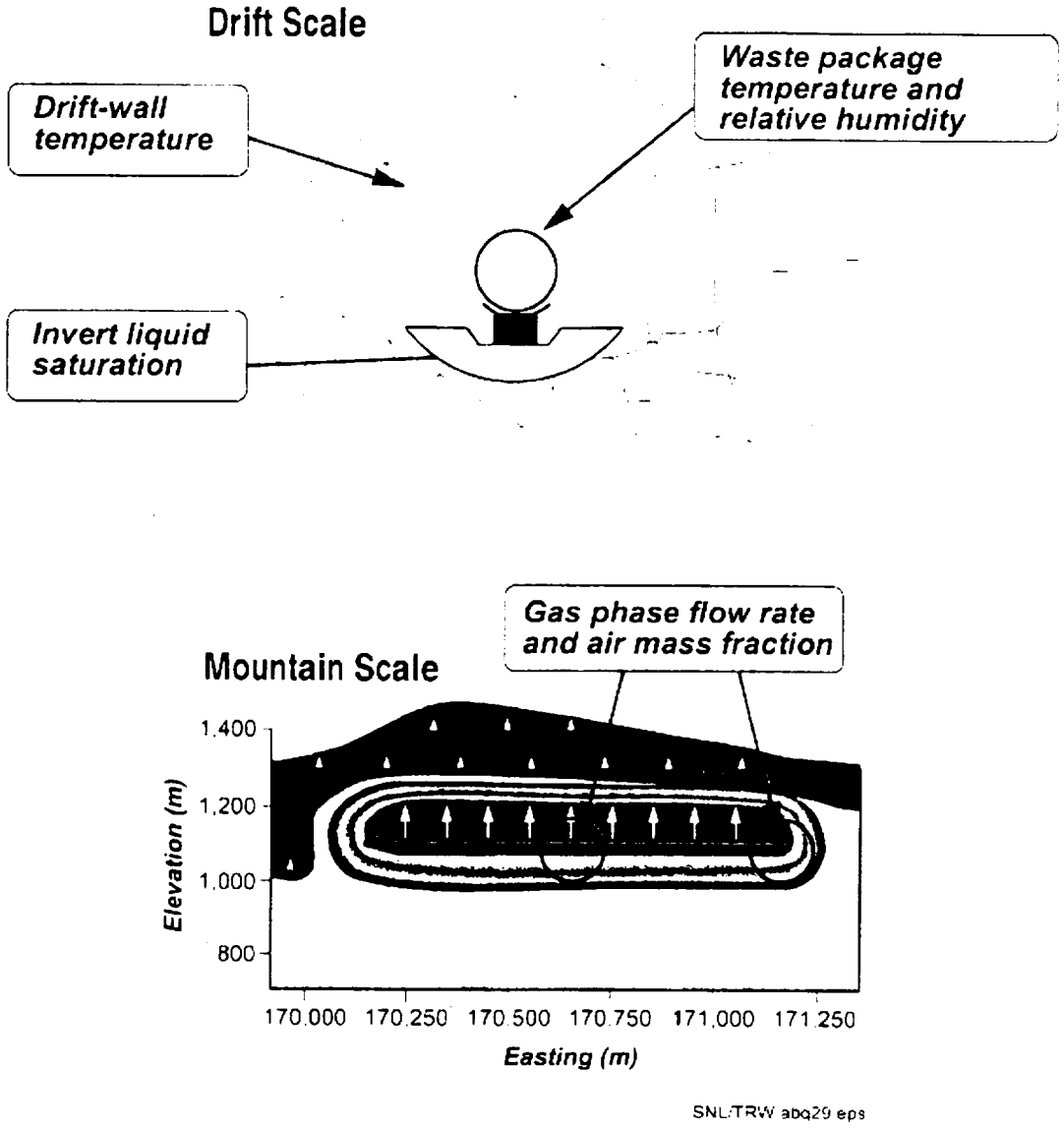

Figure 3-7. Quantities passed to other TSPA-VA components.

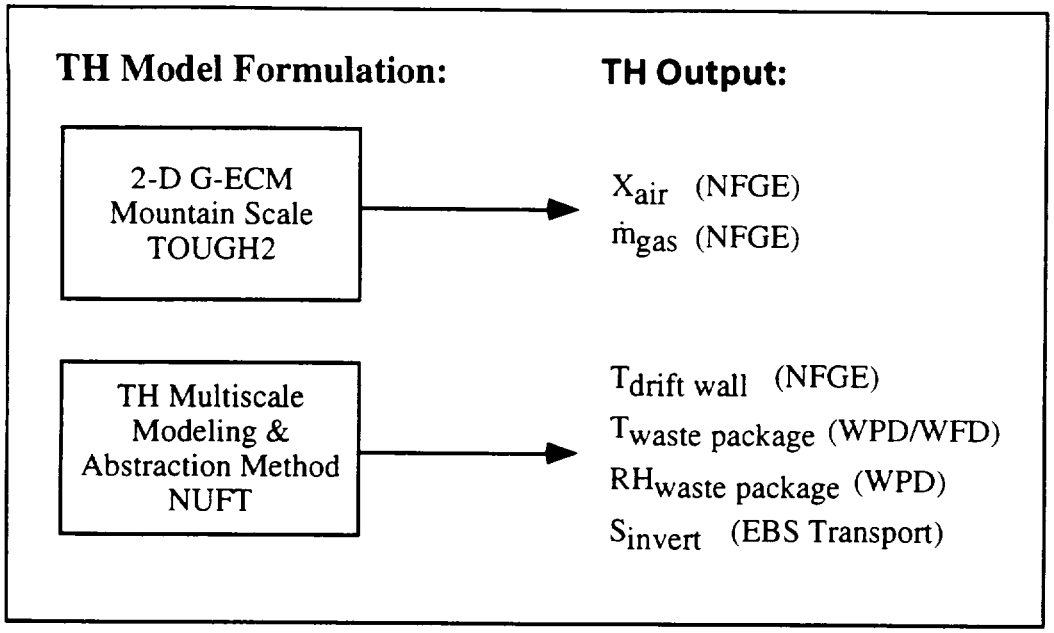

Figure 3-8. Schematic of the TH models and the results that are abstracted from each model.

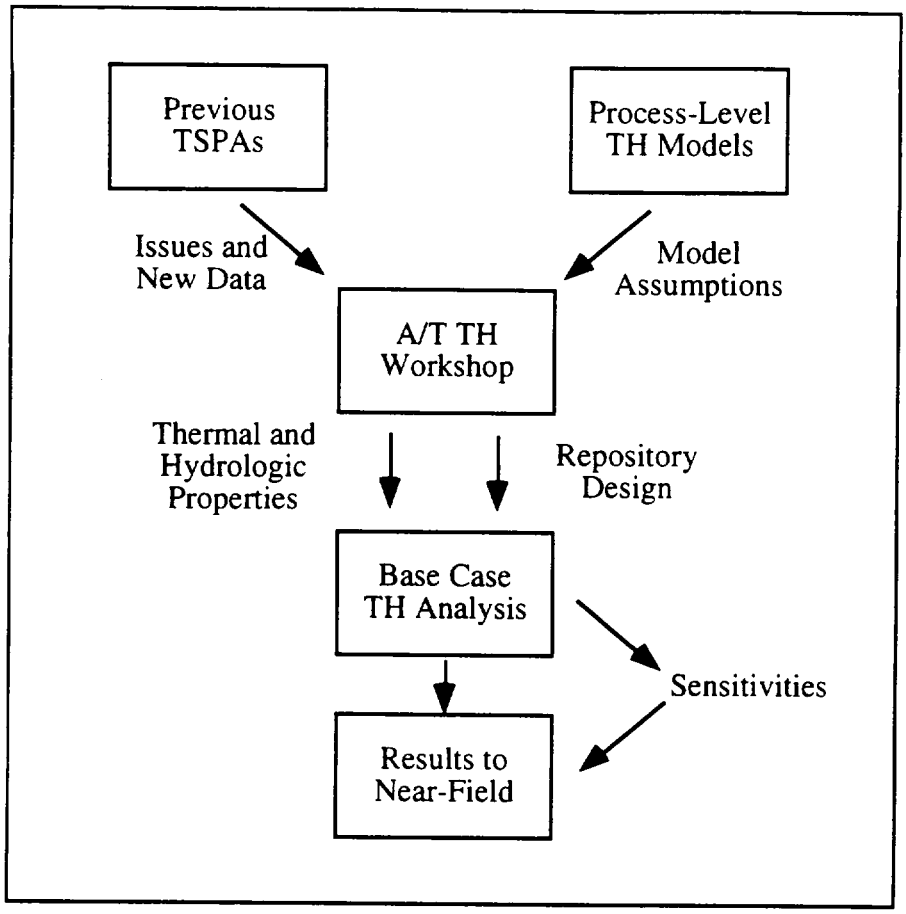

Figure 3-9. The TH process for TSPA-VA.

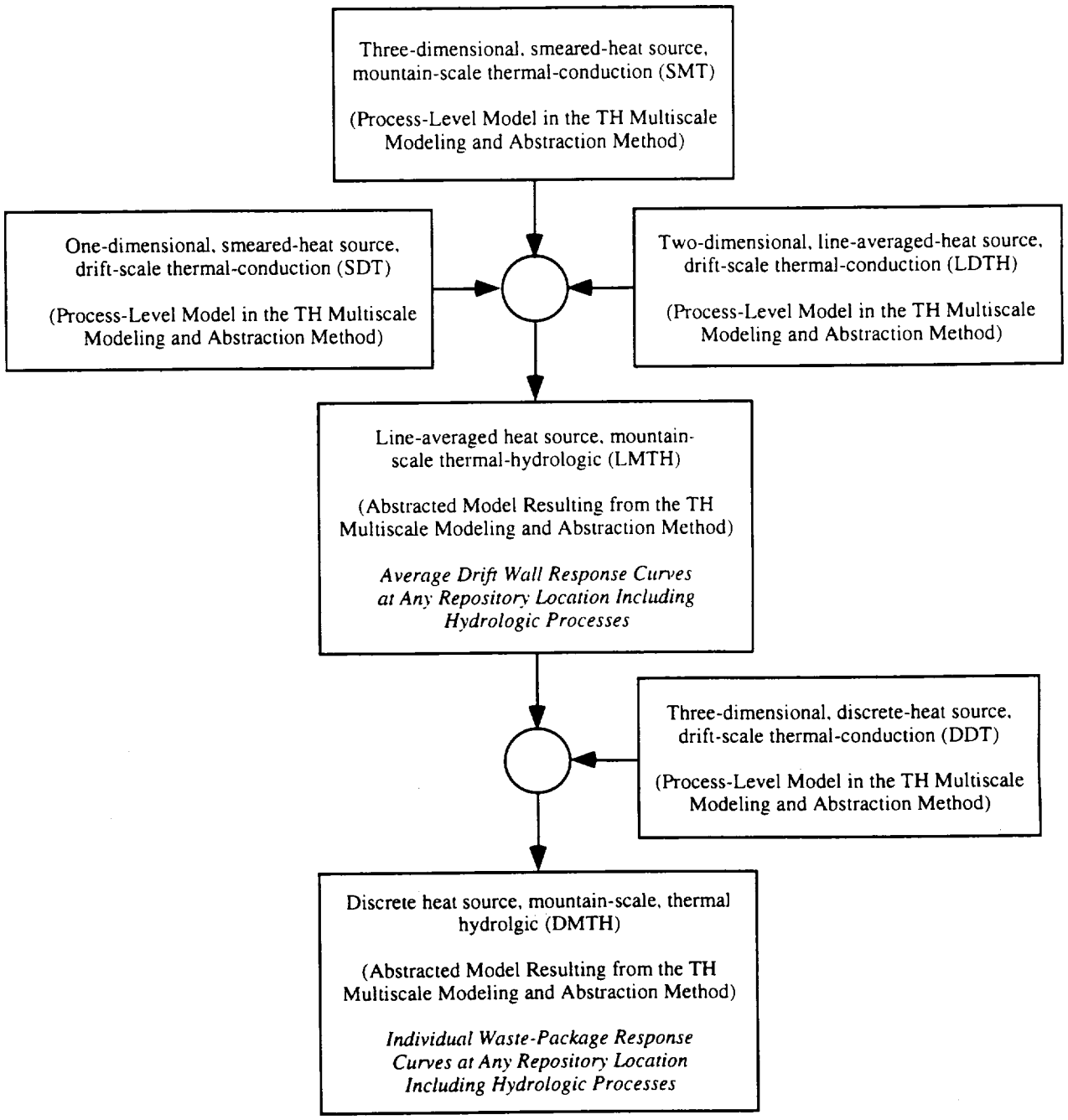

Figure 3-10. Models in the TH Multiscale Modeling and Abstraction Method.

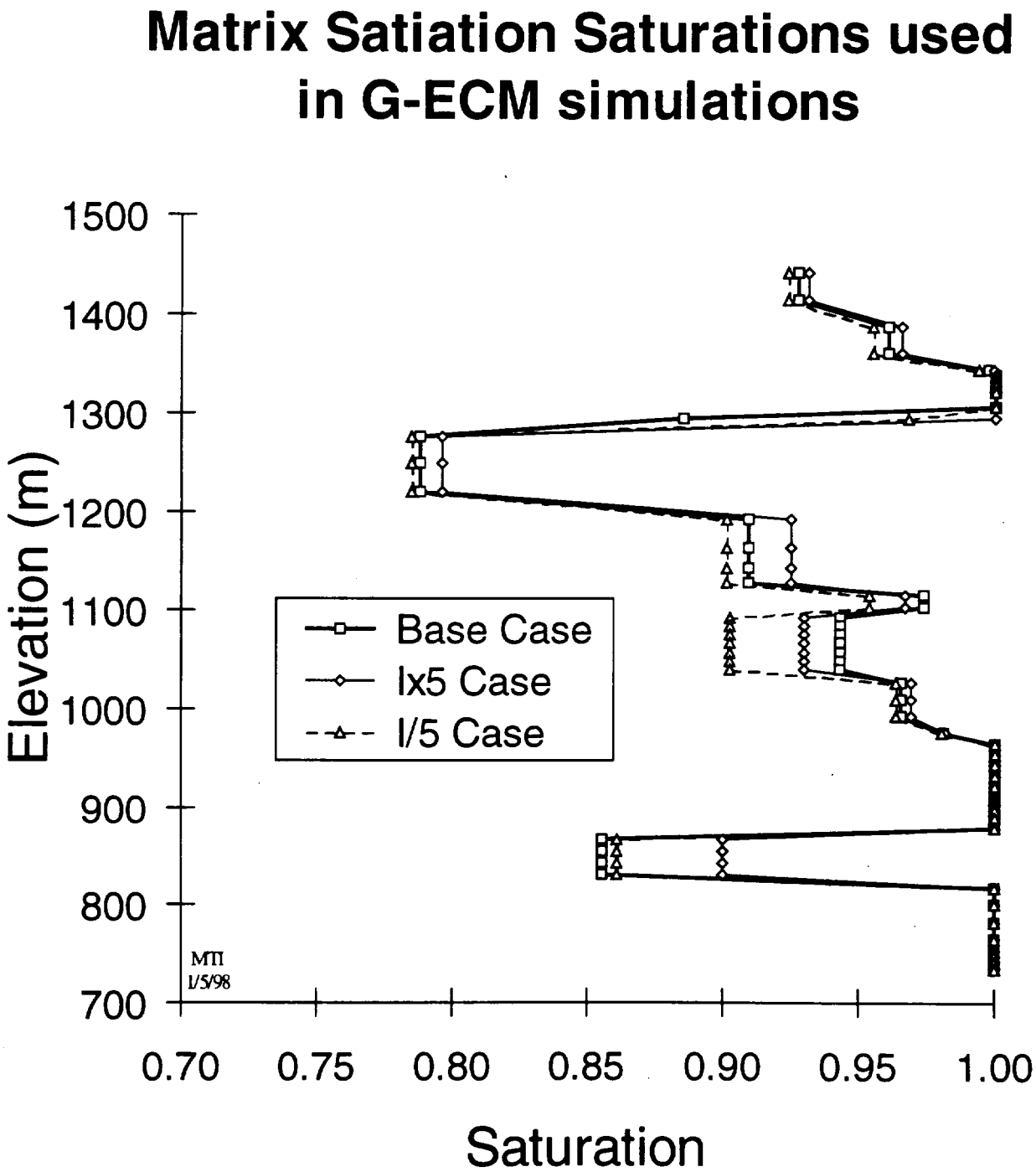

Figure 3-11. Matrix satiation saturations for the three preliminary base case property sets.

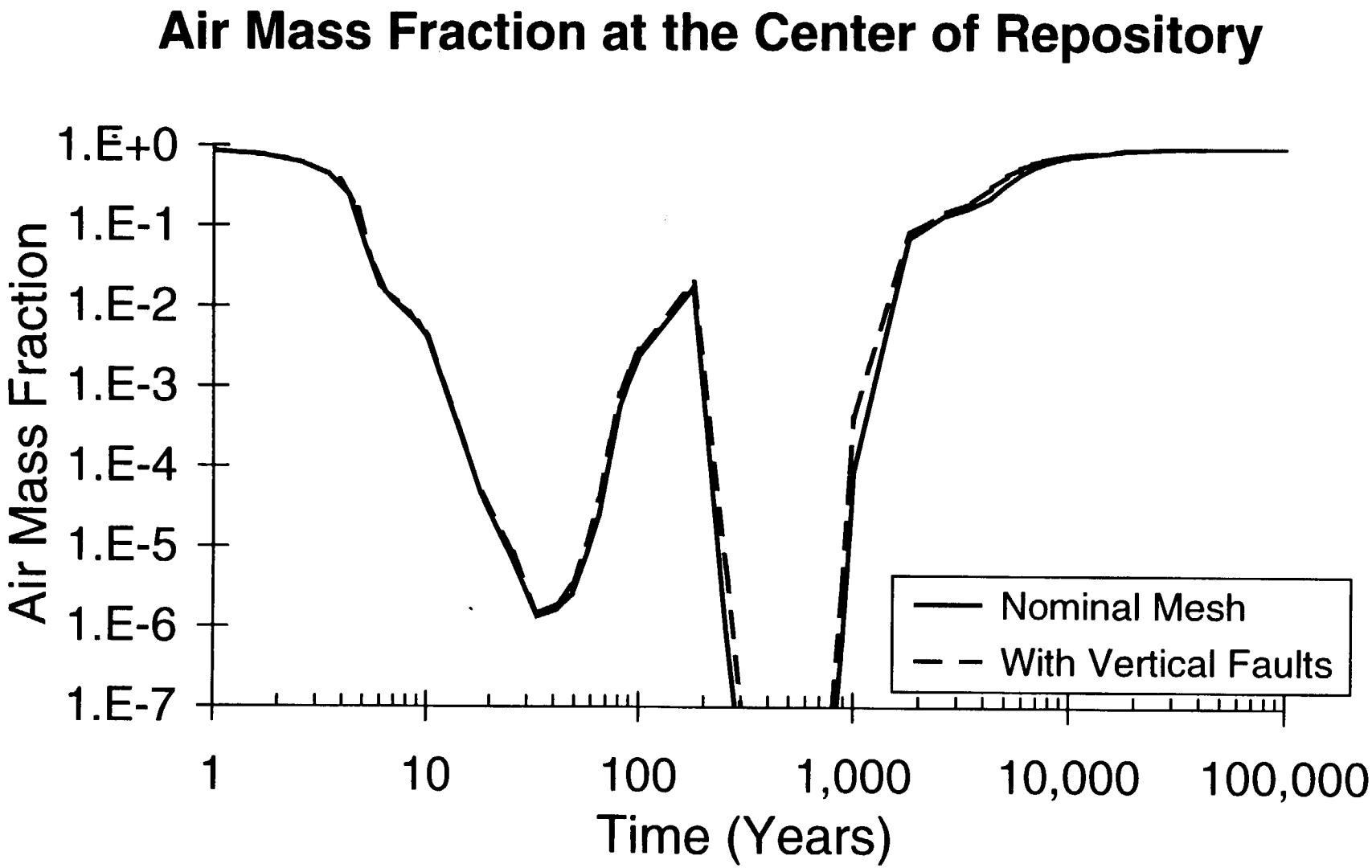

Figure 3-12. Air mass fraction at the center of the repository in the case with vertical faults and when the nominal simulation domain is used. Preliminary base-case property set at the nominal I infiltration rate.

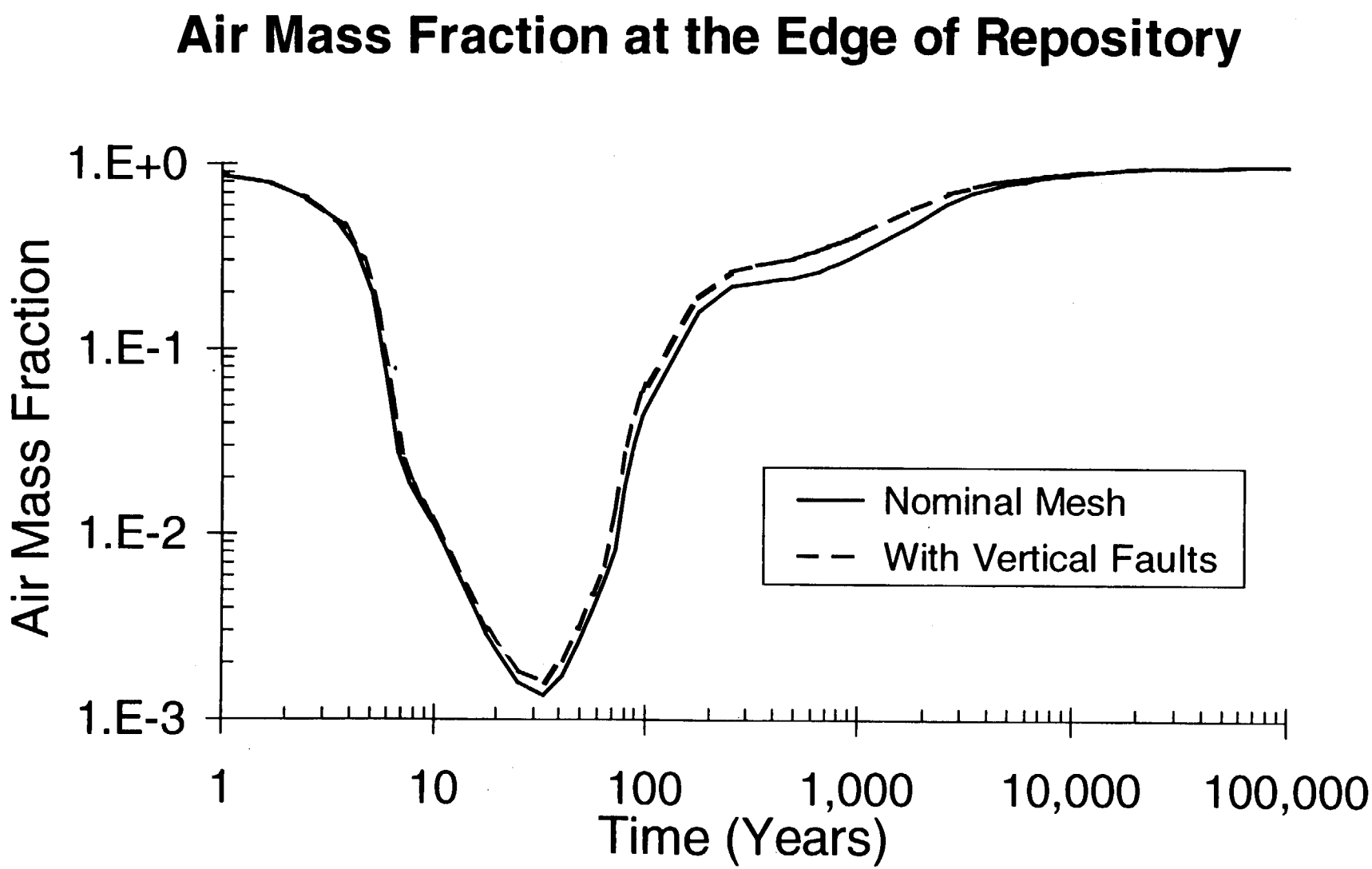

Figure 3-13. Air mass fraction at the edge of the repository in the case with vertical faults and when the nominal simulation domain is used. Preliminary base-case property set at the nominal I infiltration rate.

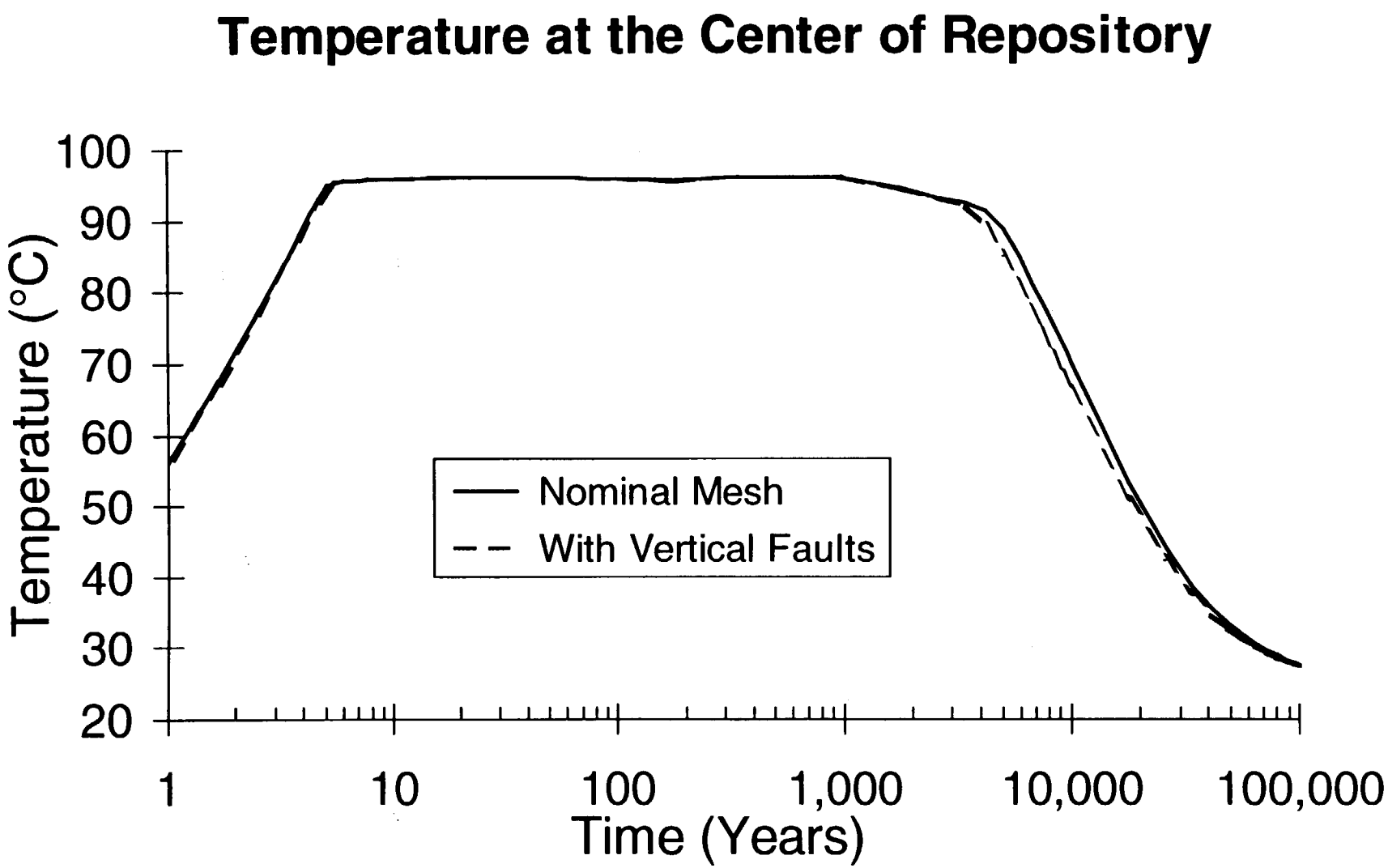

Figure 3-14. Temperature at the center of the repository in the case with vertical faults and when the nominal simulation domain is used. Preliminary base-case property set at the nominal I infiltration rate.

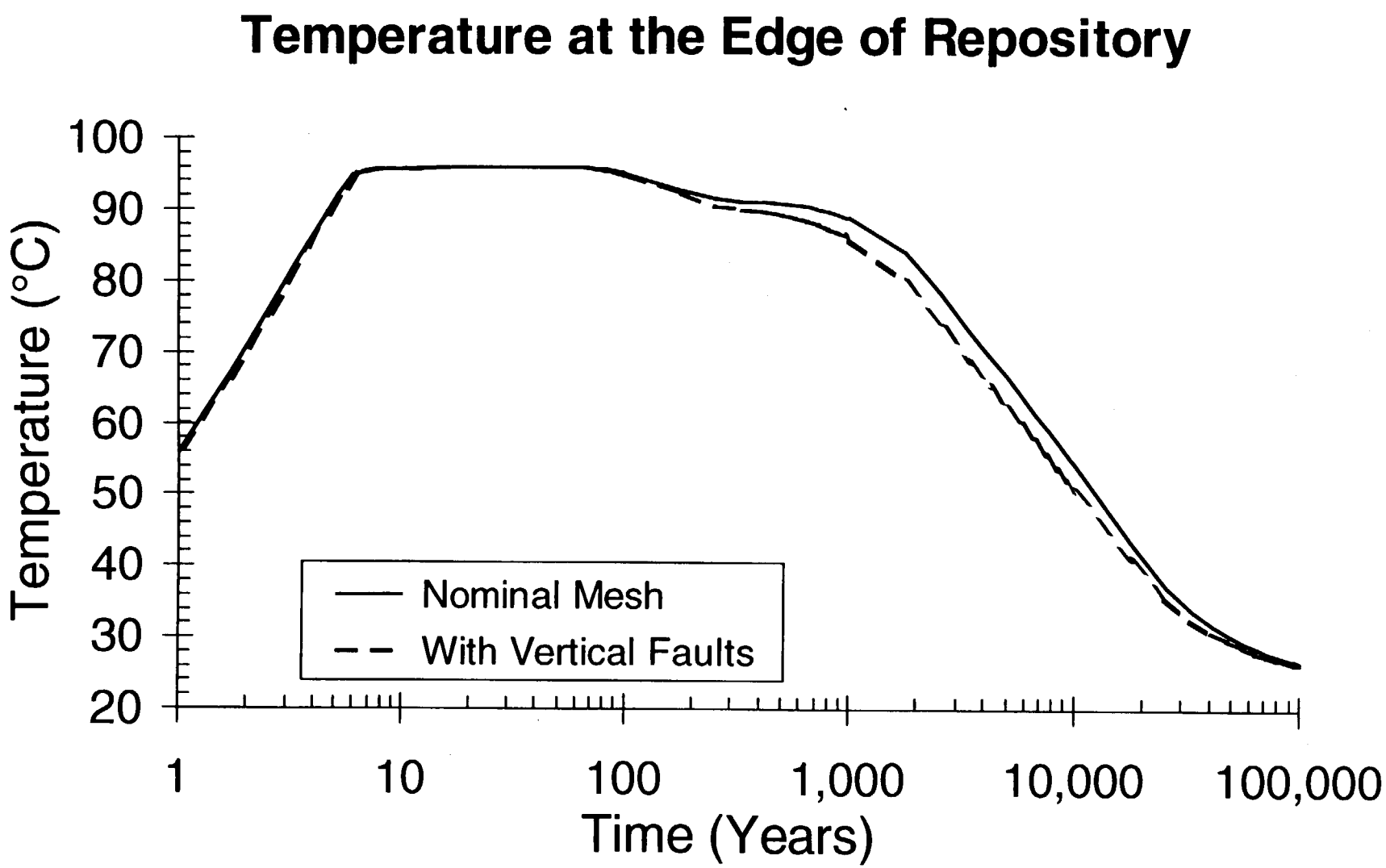

Figure 3-15. Temperature at the edge of the repository in the case with vertical faults and when the nominal simulation domain is used. Preliminary base-case property set at the nominal I infiltration rate.

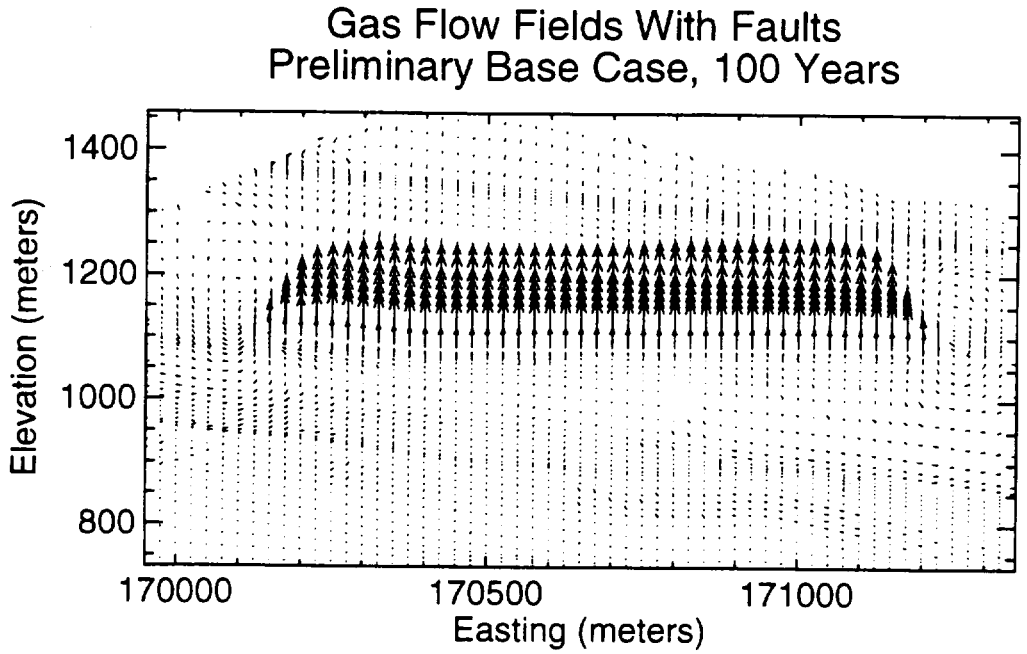

Figure 3-16. Gas flux across the simulation domain at 100 years for the simulation domains with faults. Preliminary base case property set at the nominal I infiltration rate.

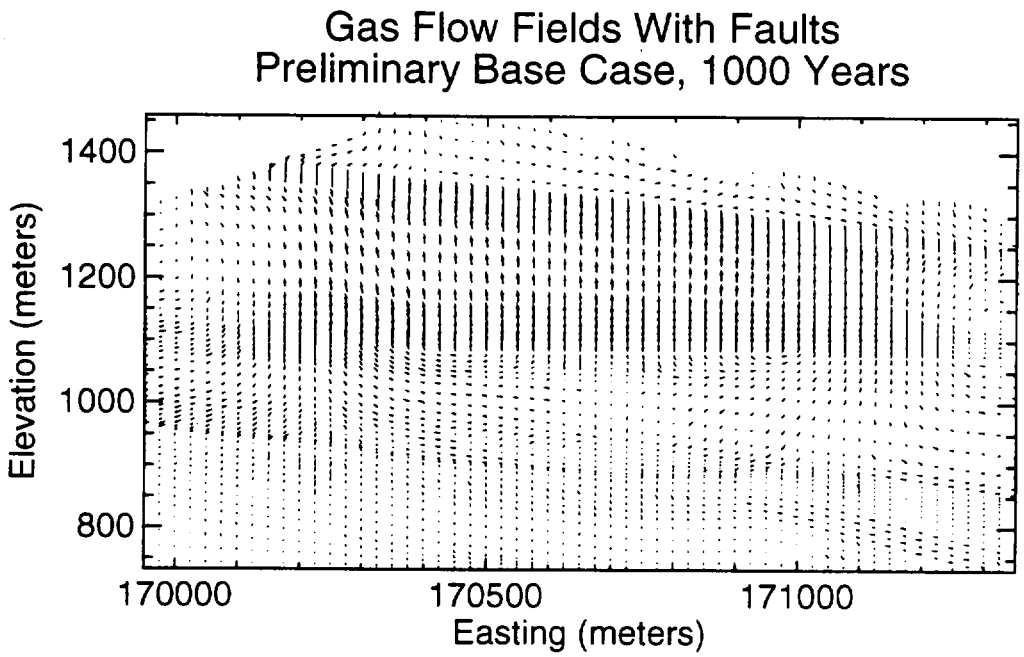

Figure 3-17. Gas flux across the simulation domain at 1000 years for the simulation domains with faults. Preliminary base case property set at the nominal I infiltration rate.

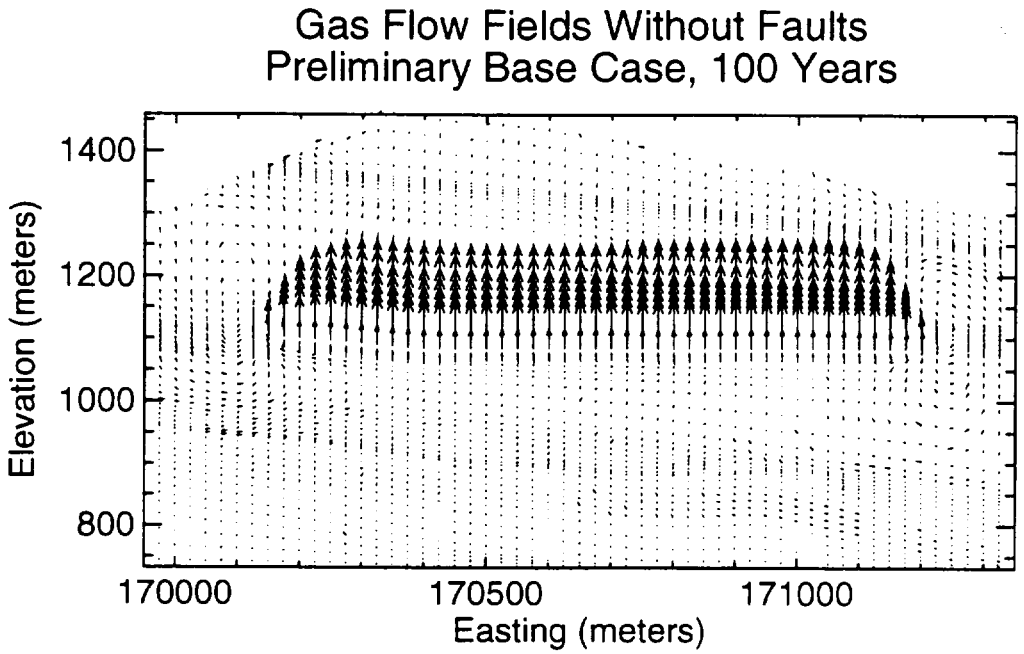

Figure 3-18. Gas flux across the simulation domain at 100 years for the nominal simulation domains. Preliminary base case property set at the nominal I infiltration rate.

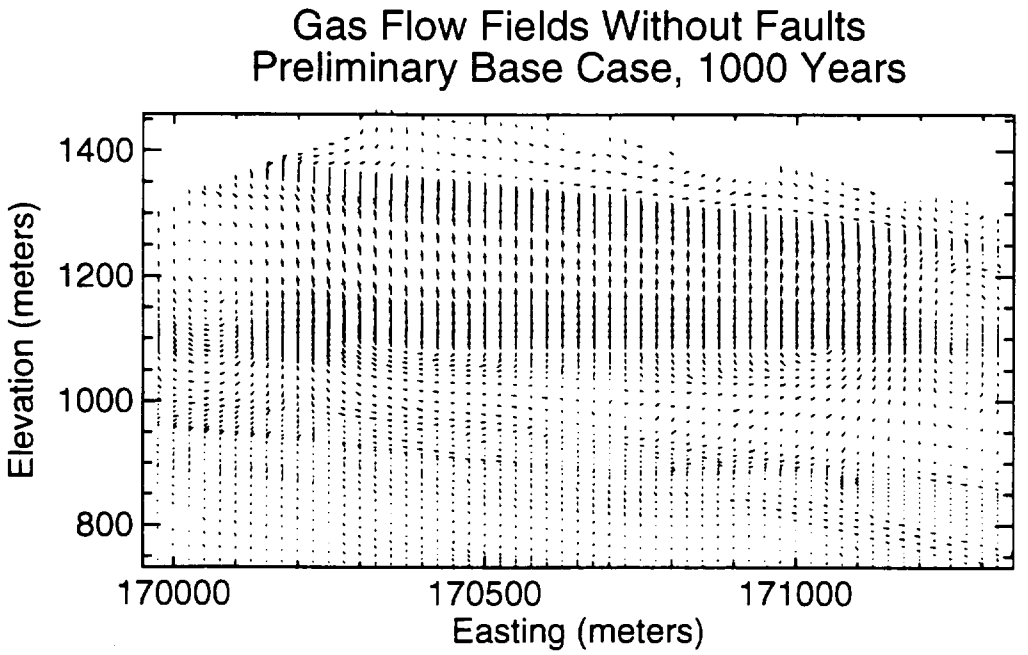

Figure 3-19. Gas flux across the simulation domain at 1000 years for the nominal simulation domains. Preliminary base case property set at the nominal I infiltration rate.

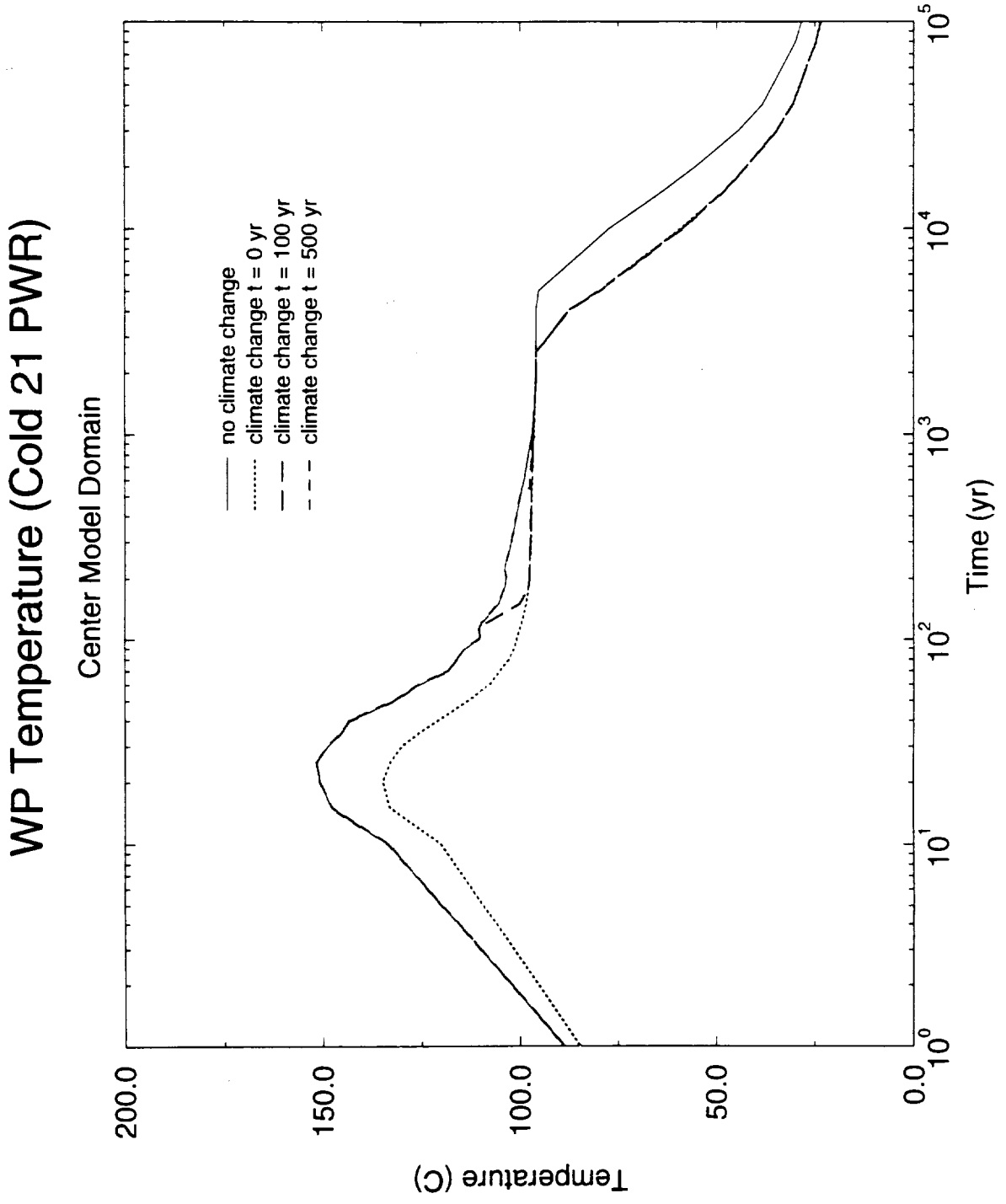

Figure 3-20. Surface temperature of a cold 21 PWR waste package located at the repository center for the present-day climate, for a climate change at 0 years, 100 years, and 500 years. Preliminary base-case nominal I property set.

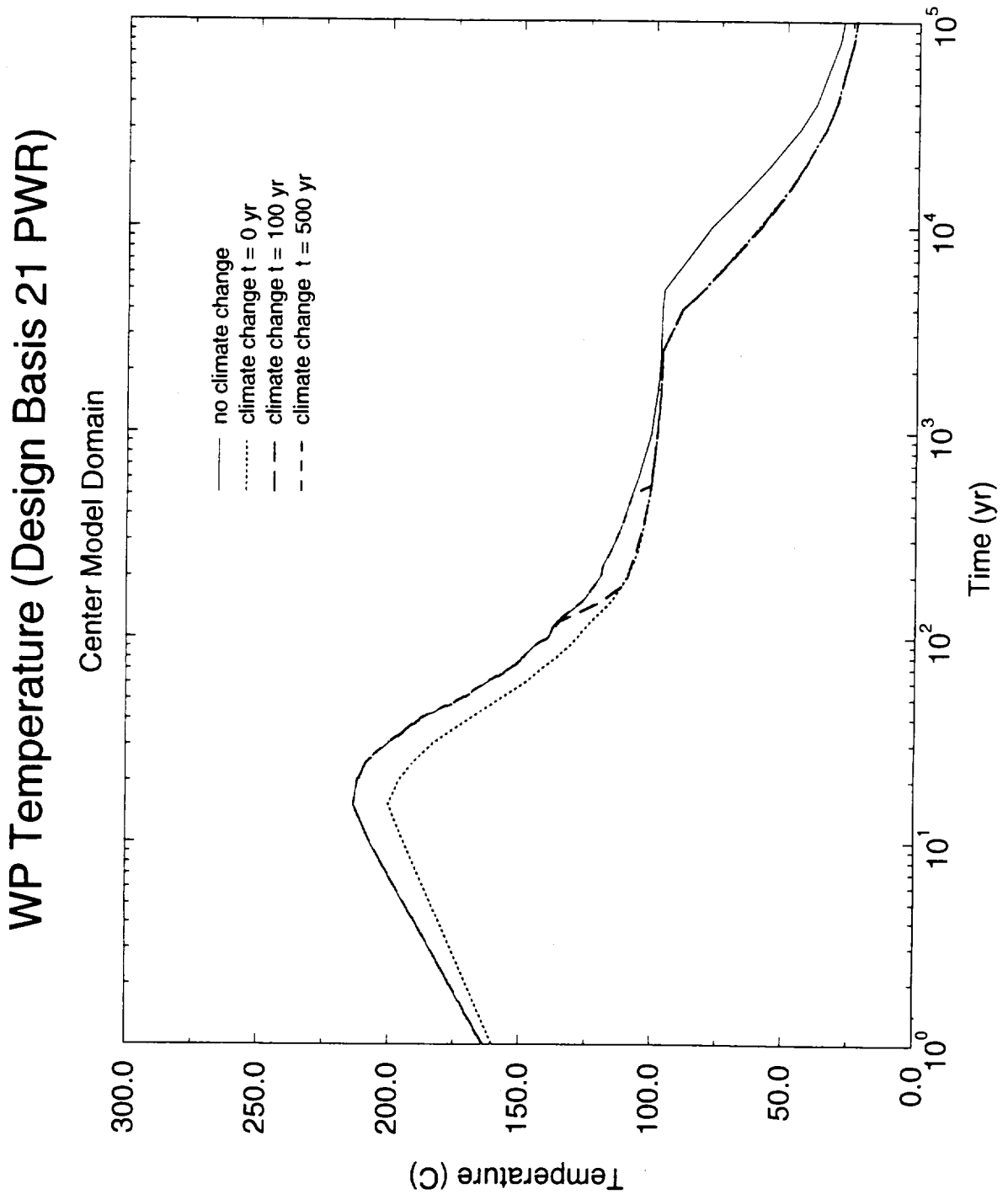

Figure 3-21. Surface temperature of a design basis 21 PWR waste package located at the repository center for the present-day climate, for a climate change at 0 years, 100 years, and 500 years. Preliminary base-case nominal I property set.

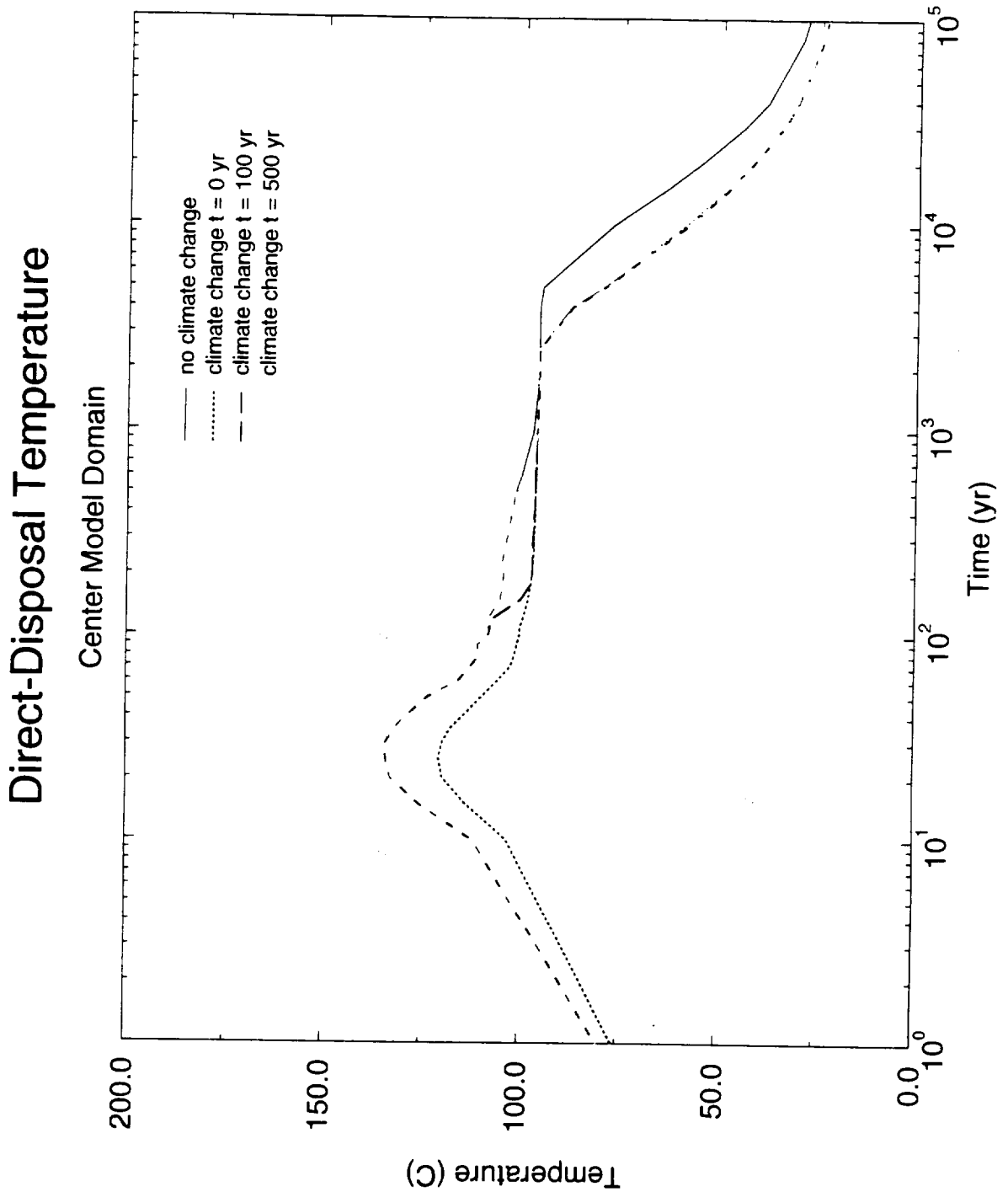

Figure 3-22. Surface temperature of a separate- (direct-) disposal waste package located at the repository center for the present-day climate, for a climate change at 0 years, 100 years, and 500 years. Preliminary base-case nominal I property set.

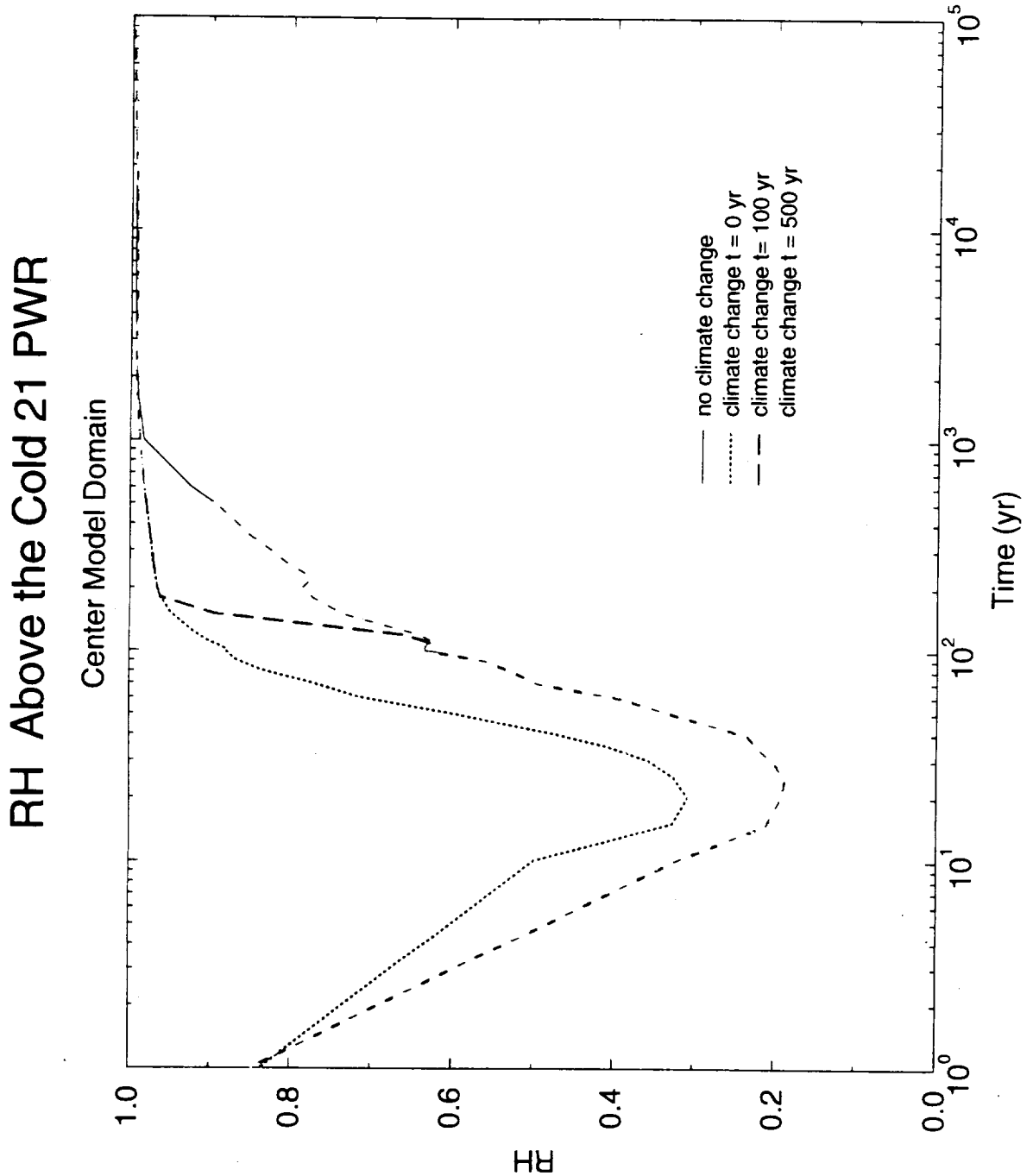

Figure 3-23. Surface relative humidity above a cold 21 PWR waste package located at the repository center for the present-day climate, for a climate change at 0 years, 100 years, and 500 years. Preliminary base-case nominal I property set.

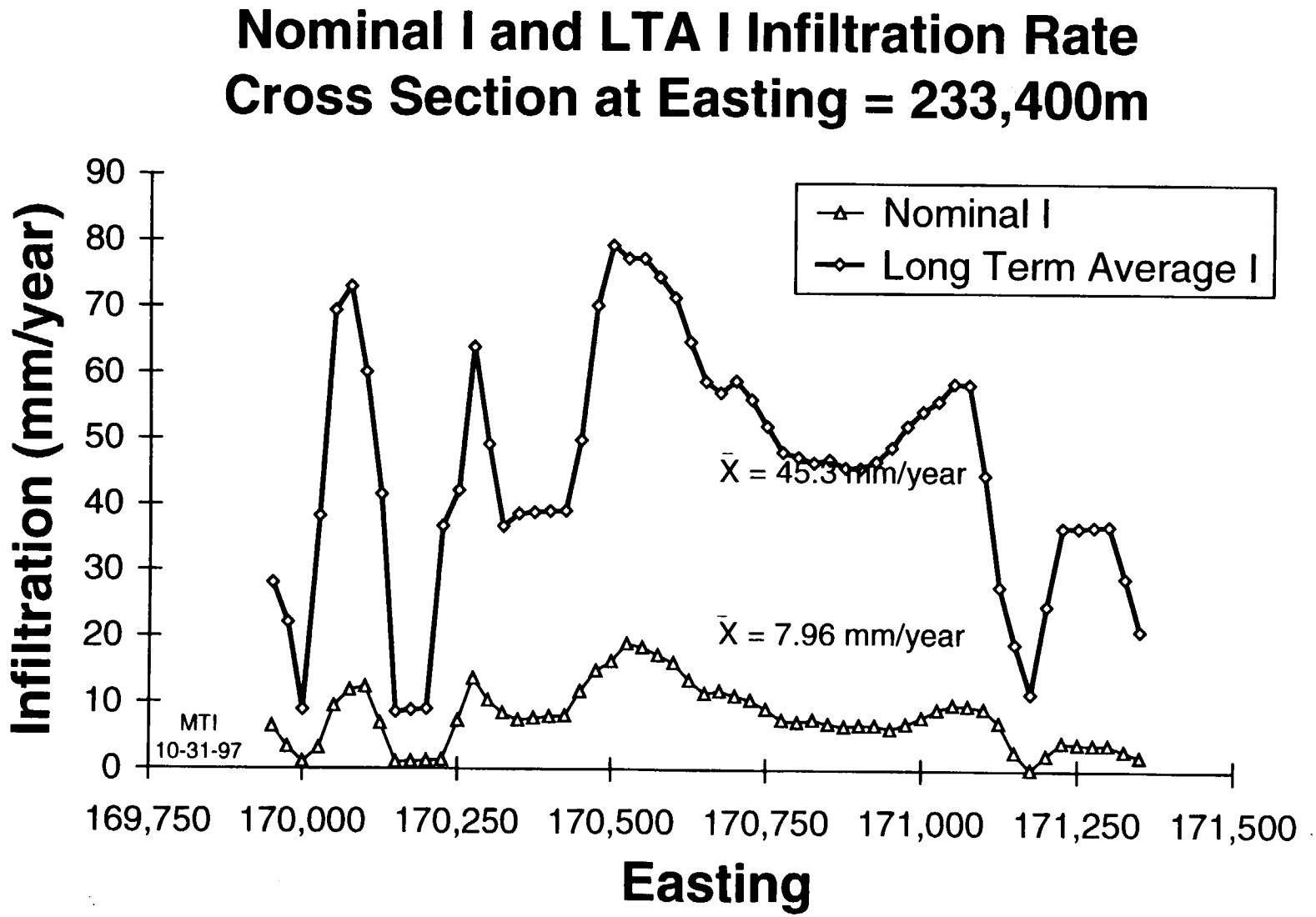

Figure 3-24. Infiltration rate over the two-dimensional mountain-scale TH simulation domain.

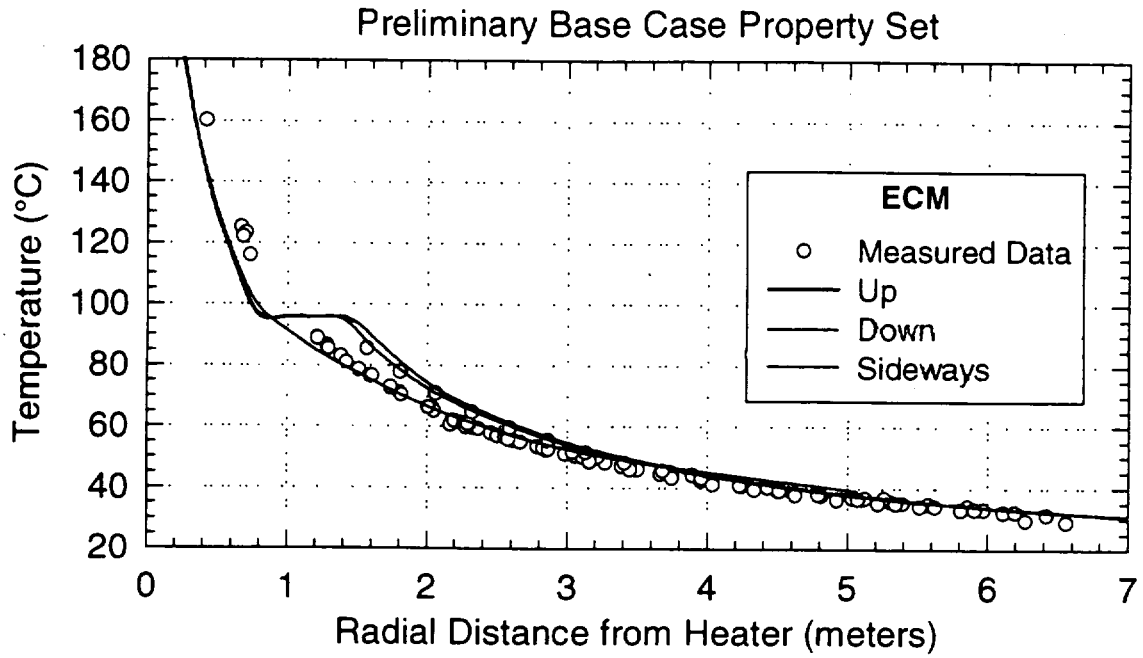

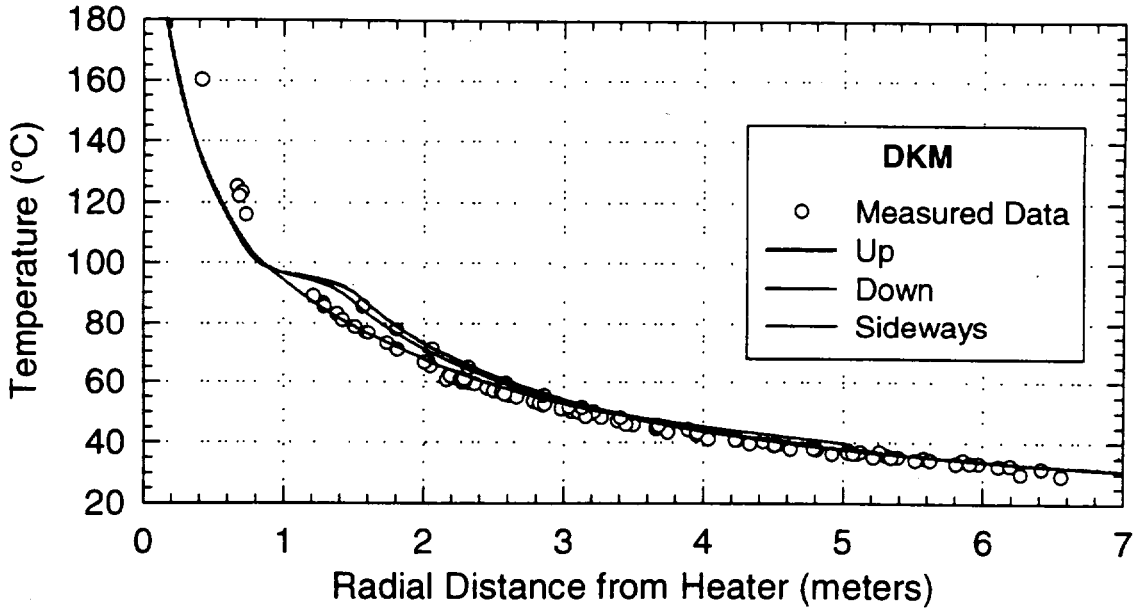

Figure 3-25. Comparison of measured data from the single-heater test to simulation results using both ECM and DKM formulations with the preliminary base-case property set.

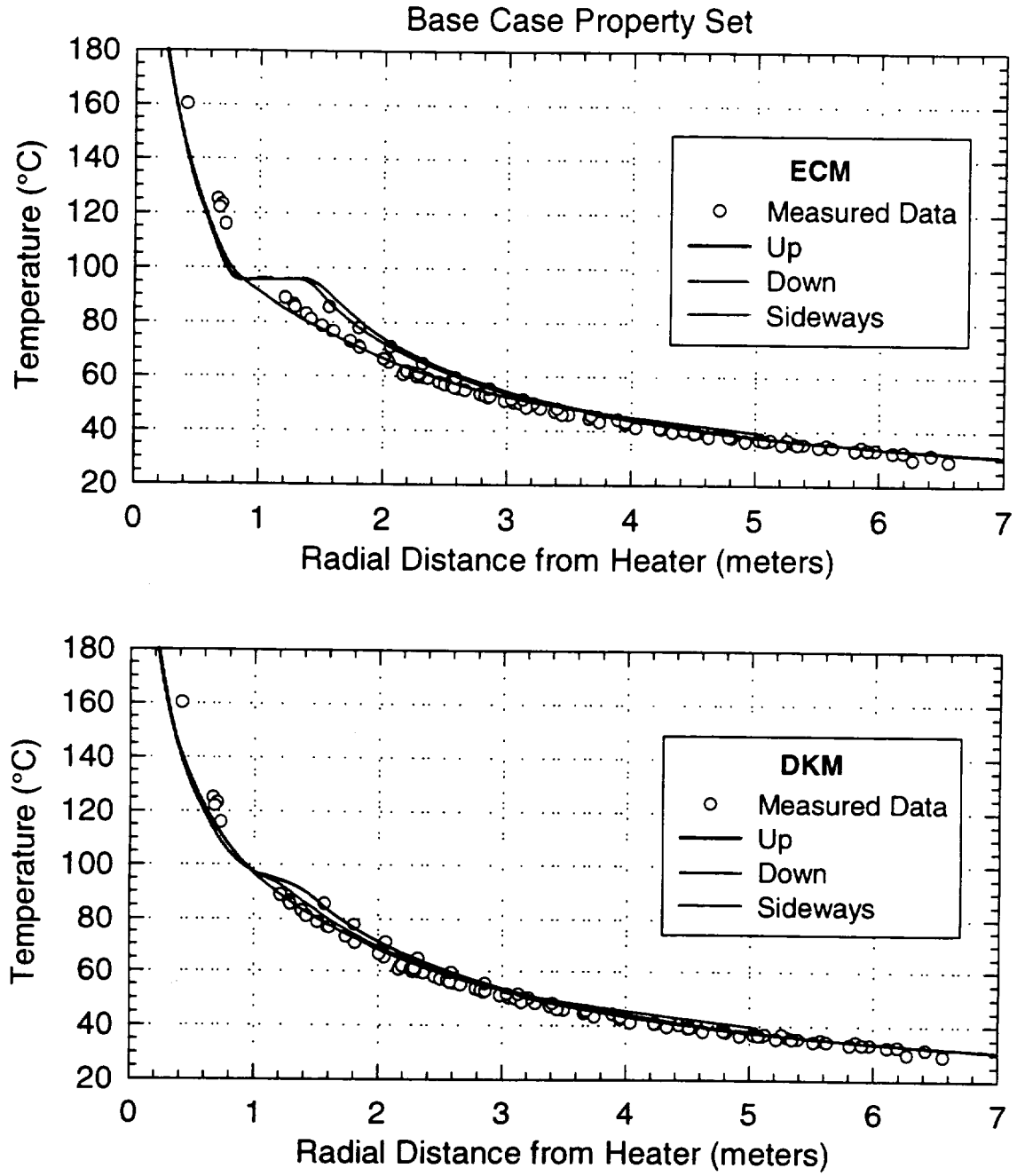

Figure 3-26. Comparison of measured data from the single-heater test to simulation results using both ECM and DKM formulations with the base-case property set.

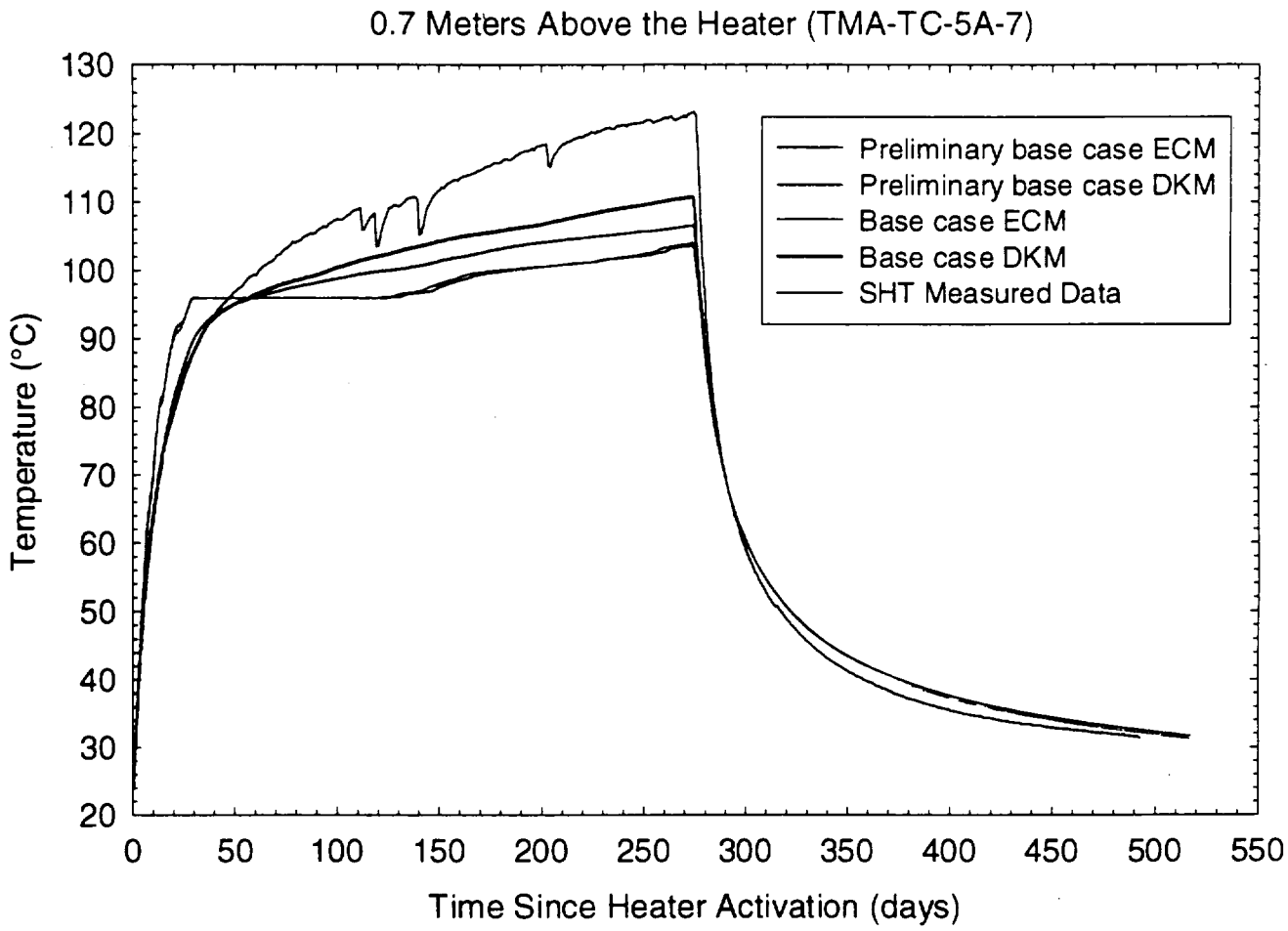

Figure 3-27. Comparison of measured data above the single-heater test to simulation results using both ECM and DKM formulations with the preliminary base case and base-case property sets.

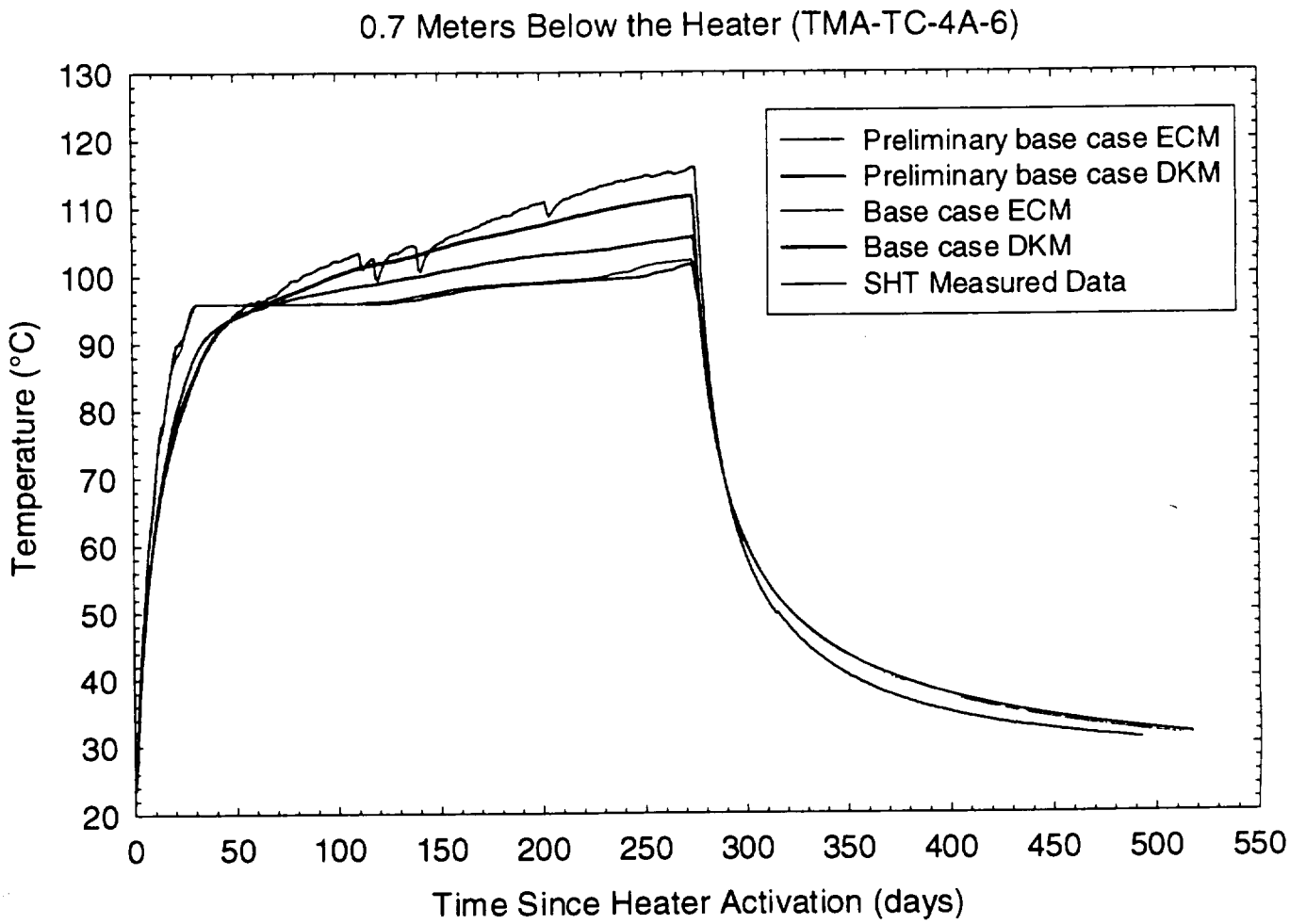

Figure 3-28. Comparison of measured data below the single-heater test to simulation results using both ECM and DKM formulations with the preliminary base case and base-case property sets.

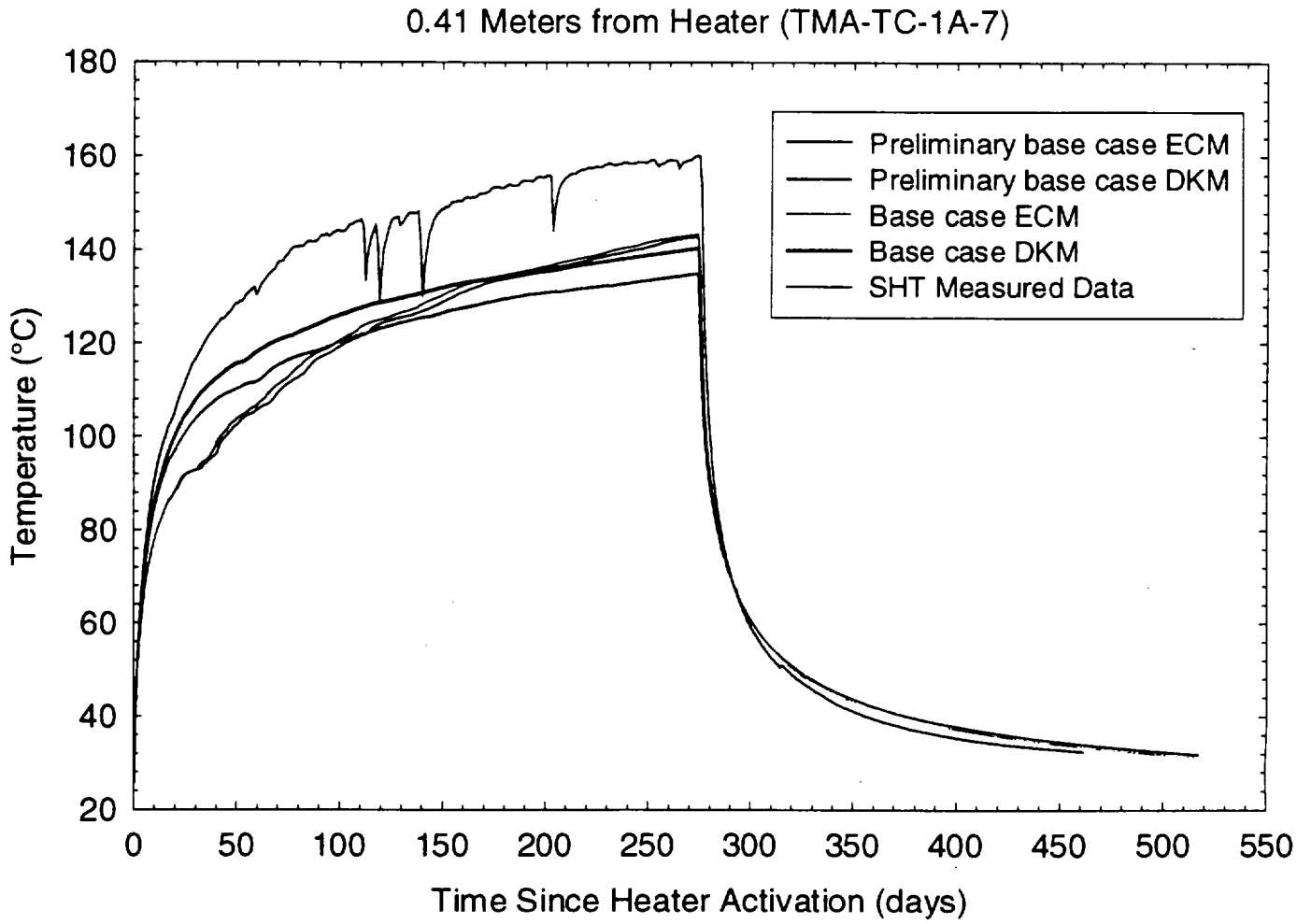

Figure 3-29. Comparison of measured data off the vertical of the single-heater test to simulation results using both ECM and DKM formulations with the preliminary base case and base-case property sets.

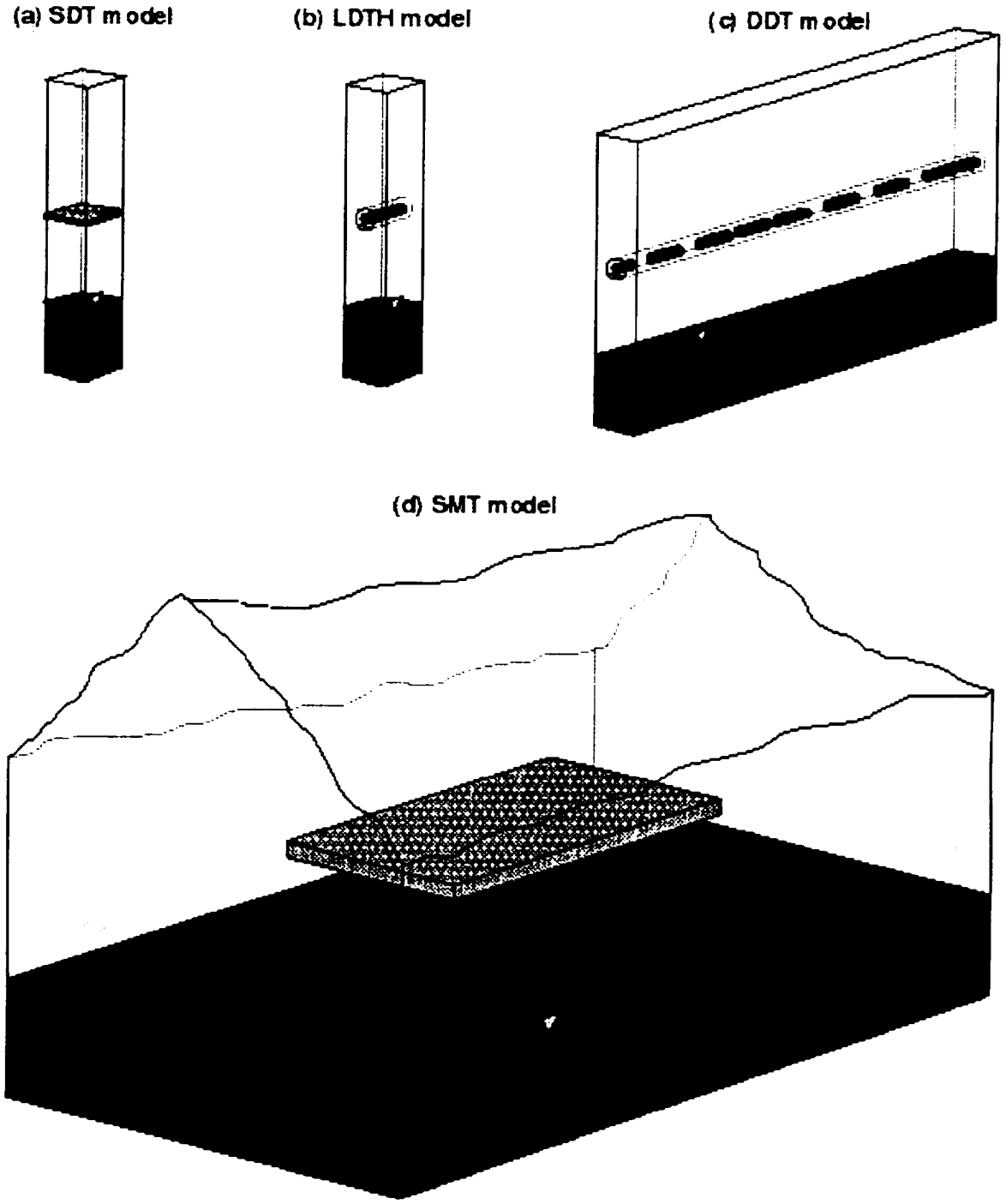

Figure 3-30. Schematic of conceptual models used by the TH multiscale modeling and abstraction method, including (a) SDT model, (b) LDTH model, (c) DDT model, and (d) SMT model (Hardin 1998).

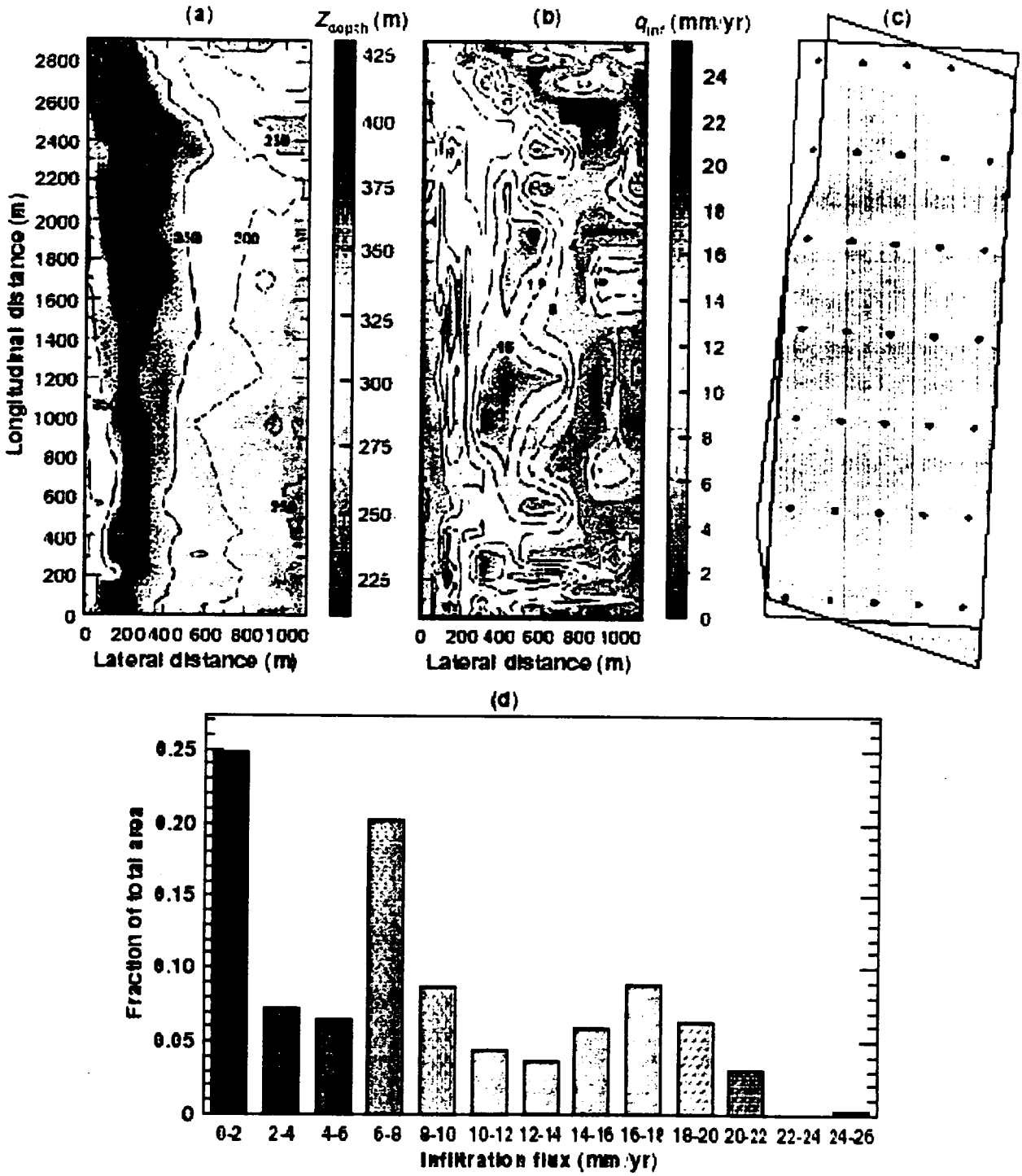

Figure 3-31. Surface topography, shallow infiltration, repository footprint, and model domain for site-scale thermal modeling at Yucca Mountain: (a) contour map showing repository depth Z_{rep} below the ground surface; (b) contour map of infiltration-flux distribution [Flint et al., 1996a] plotted over the SMT-model representation of the repository area; (c) SMT-model representation of the repository area compared with the actual repository area (depicted in gray); also shown—the 35 drift-scale-model locations in the 5 □ 7 grid used in the TH multiscale modeling and abstraction method; (d) frequency histogram for the shallow infiltration flux, corresponding to the contour map of (b) (Hardin 1998).

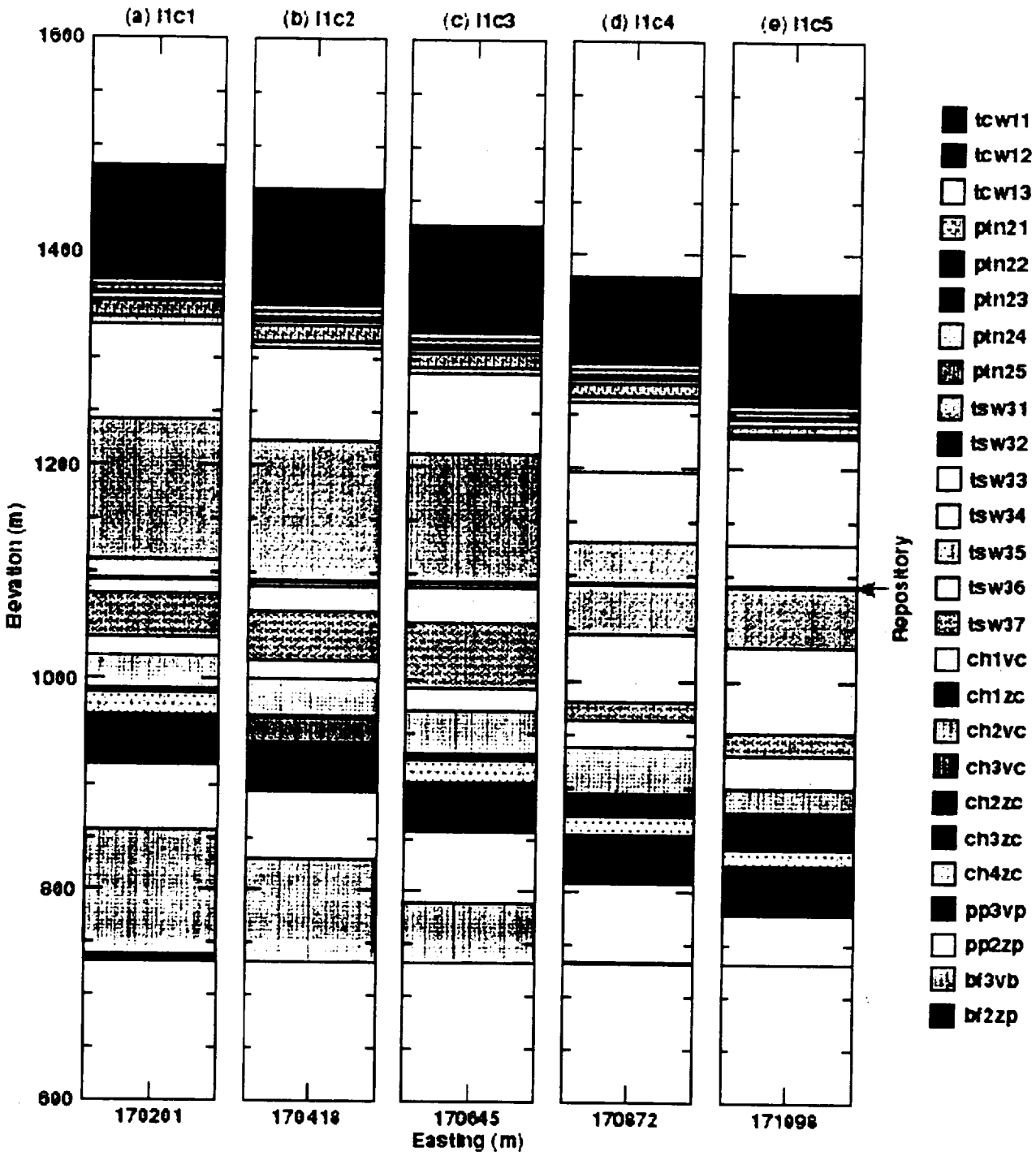

Figure 3-32. Vertical distribution of hydrostratigraphic model units shown for several drift-scale model locations (in Nevada-State coordinates), including (a) l1c1 at Northing = 232406 m, (b) l1c2 at Northing = 232394 m, (c) l1c3 at Northing = 232382 m, (d) l1c4 at Northing = 232370 m, and (e) l1c5 at Northing = 232358 m (Hardin 1998).

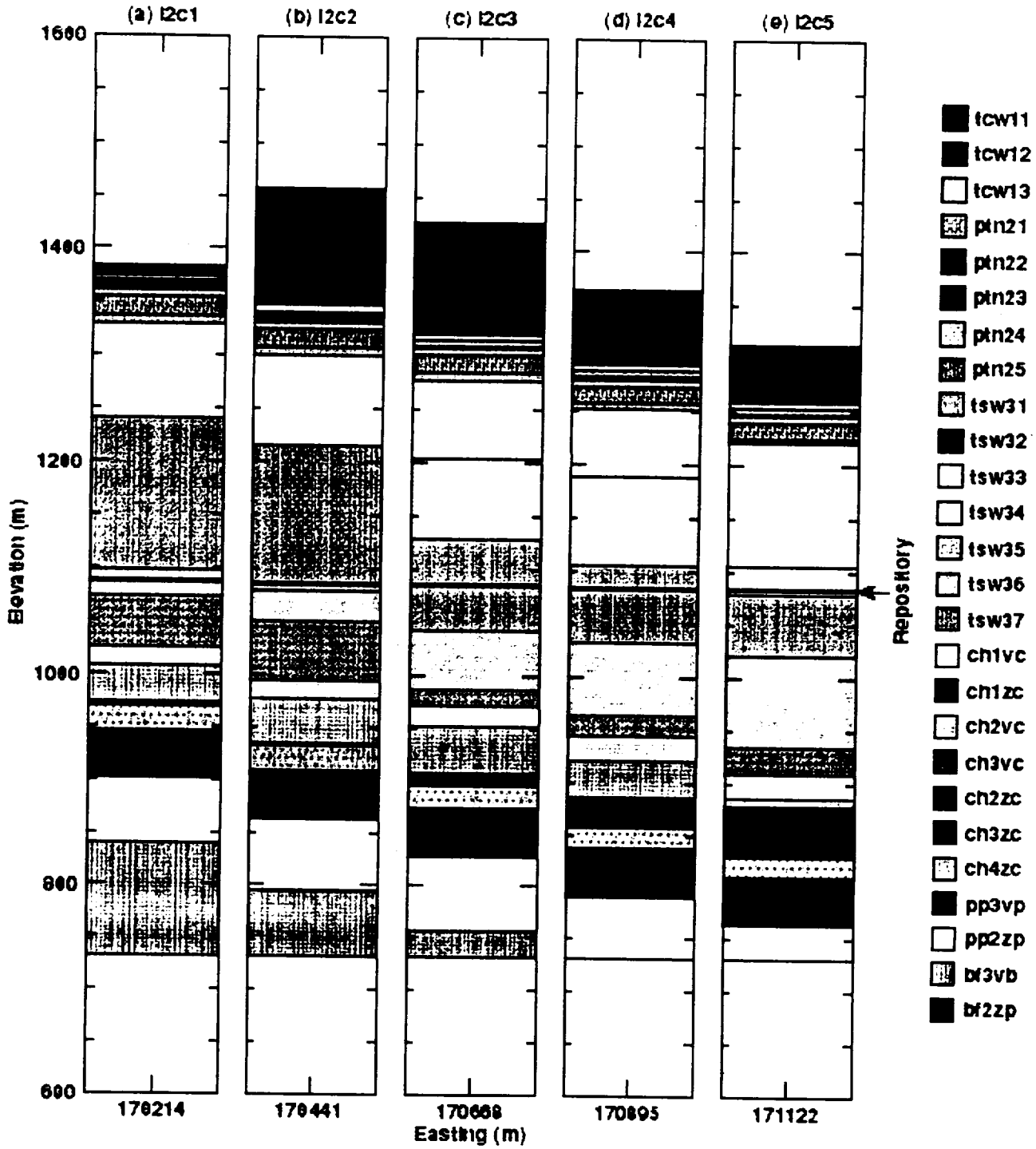

Figure 3-33. Vertical distribution of hydrostratigraphic model units shown for drift-scale model locations (in Nevada-State coordinates), including (a) I2c1 at Northing = 232857 m, (b) I2c2 at Northing = 232845 m, (c) I2c3 at Northing = 232833 m, (d) I2c4 at Northing = 232821 m, and (e) I2c5 at Northing = 232809 m (Hardin 1998).

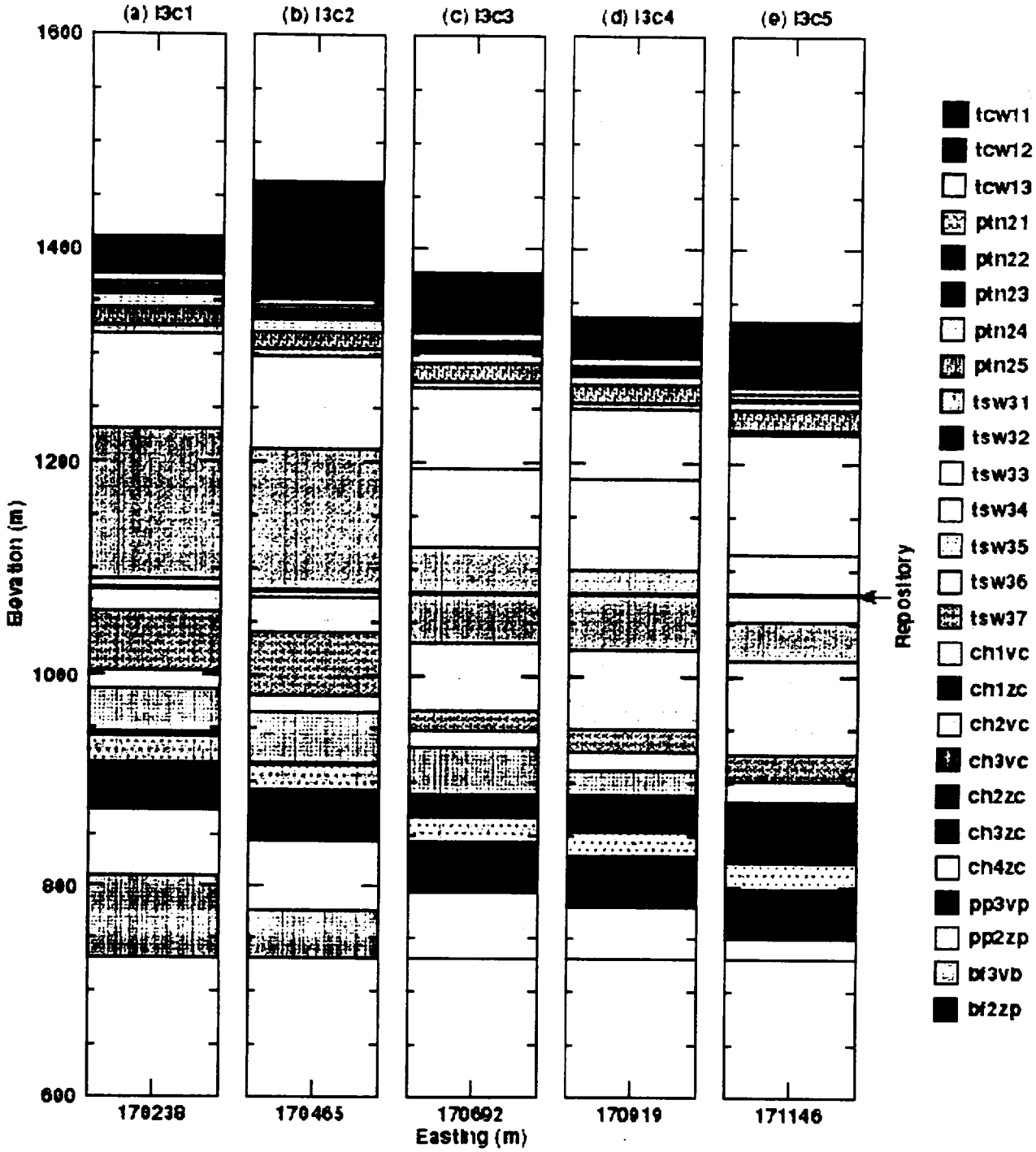

Figure 3-34. Vertical distribution of hydrostratigraphic model units shown for drift-scale model locations (in Nevada-State coordinates), including (a) I3c1 at Northing = 233308 m, (b) I3c2 at Northing = 233296 m, (c) I3c3 at Northing = 233285 m, (d) I3c4 at Northing = 233273 m, and (e) I3c5 at Northing = 233261 m (Hardin 1998)

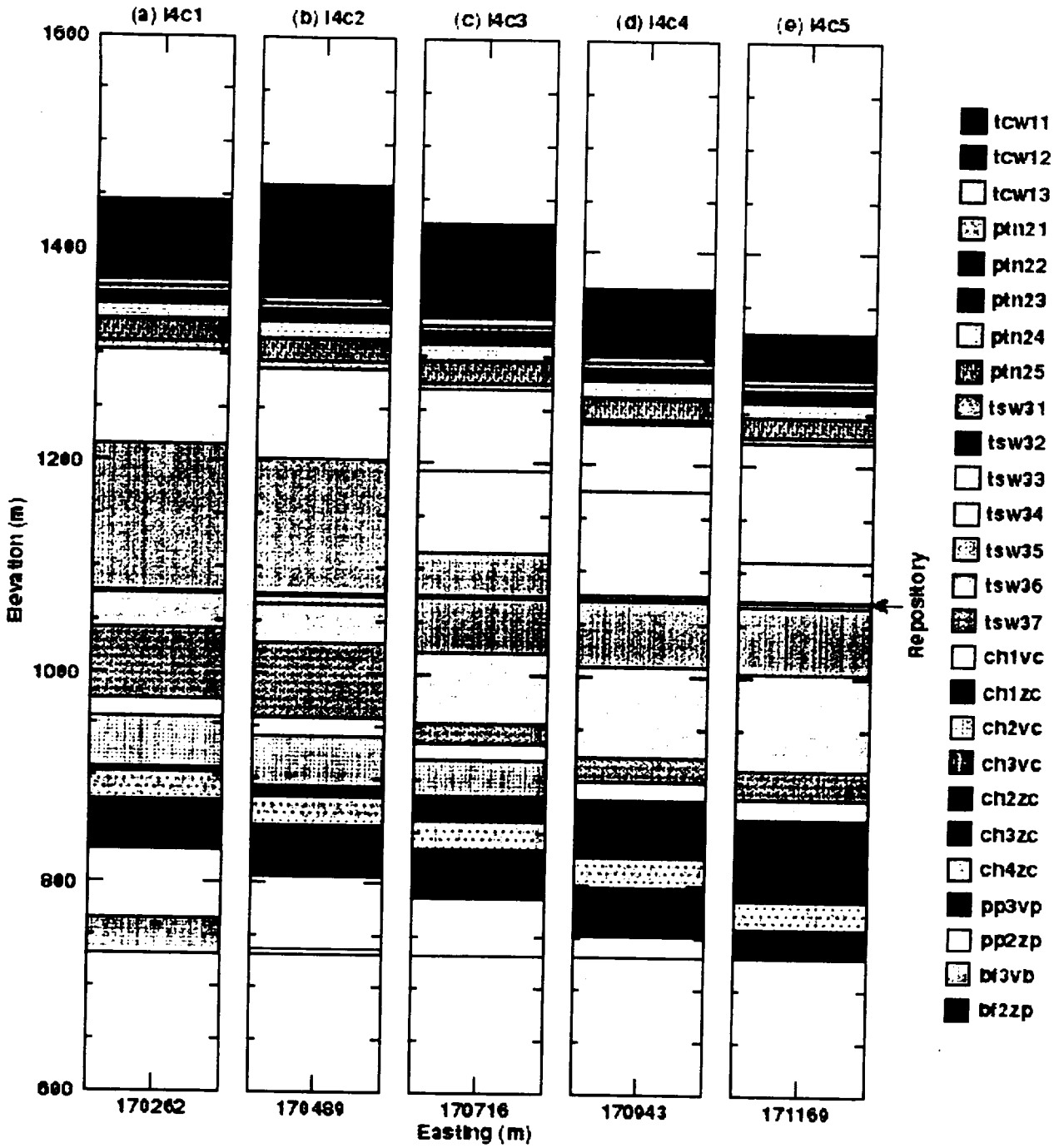

Figure 3-35. Vertical distribution of hydrostratigraphic model units shown for drift-scale model locations (in Nevada-State coordinates), including (a) I4c1 at Northing = 233760 m, (b) I4c2 at Northing = 233748 m, (c) I4c3 at Northing = 233736 m, (d) I4c4 at Northing = 233724 m, and (e) I4c5 at Northing = 233712 m (Hardin 1998).

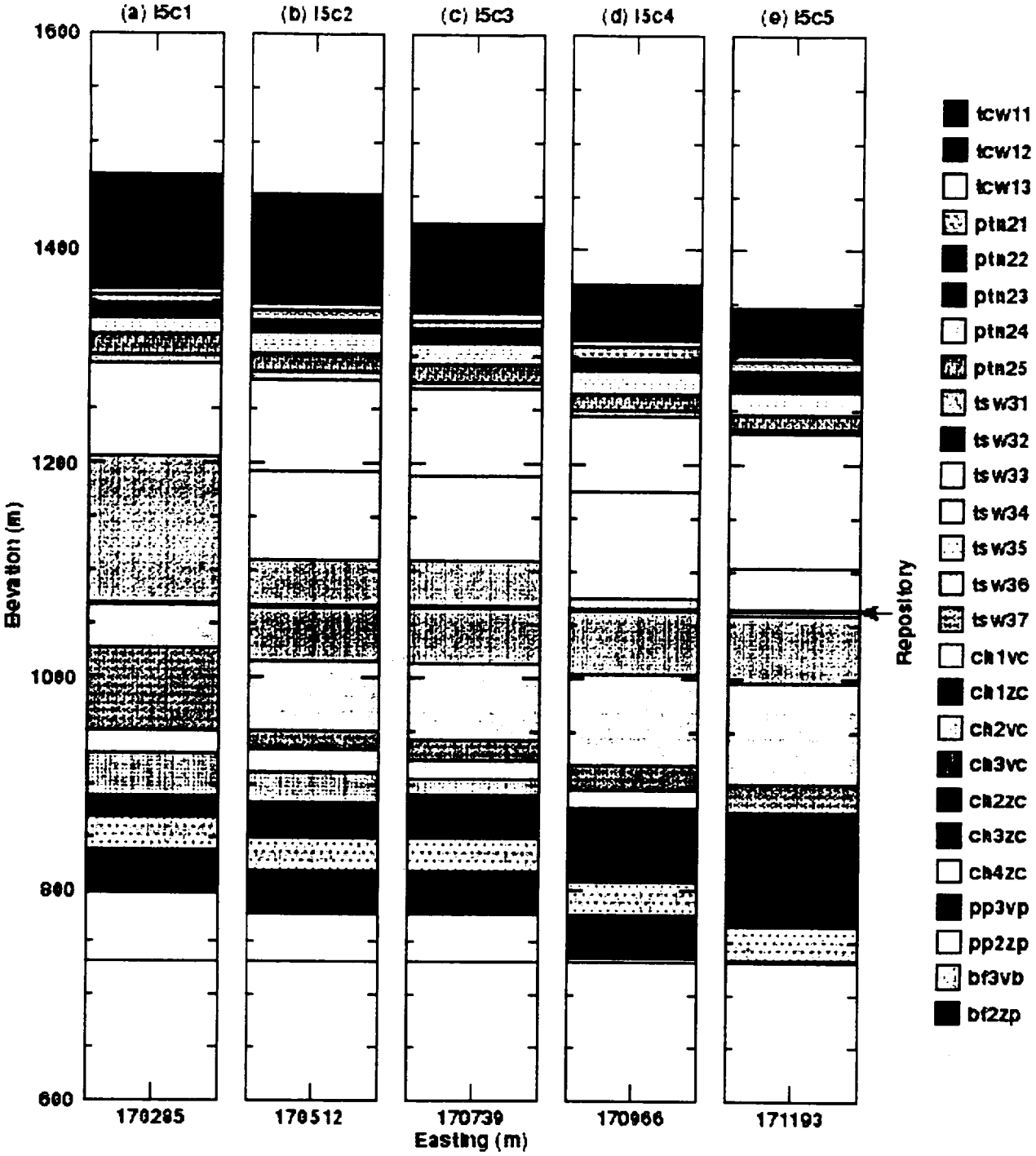

Figure 3-36. Vertical distribution of hydrostratigraphic model units shown for drift-scale model locations (in Nevada-State coordinates), including (a) I5c1 at Northing = 234211 m, (b) I5c2 at Northing = 234199 m, (c) I5c3 at Northing = 234187 m, (d) I5c4 at Northing = 234175 m, and (e) I5c5 at Northing = 234164 m (Hardin 1998).

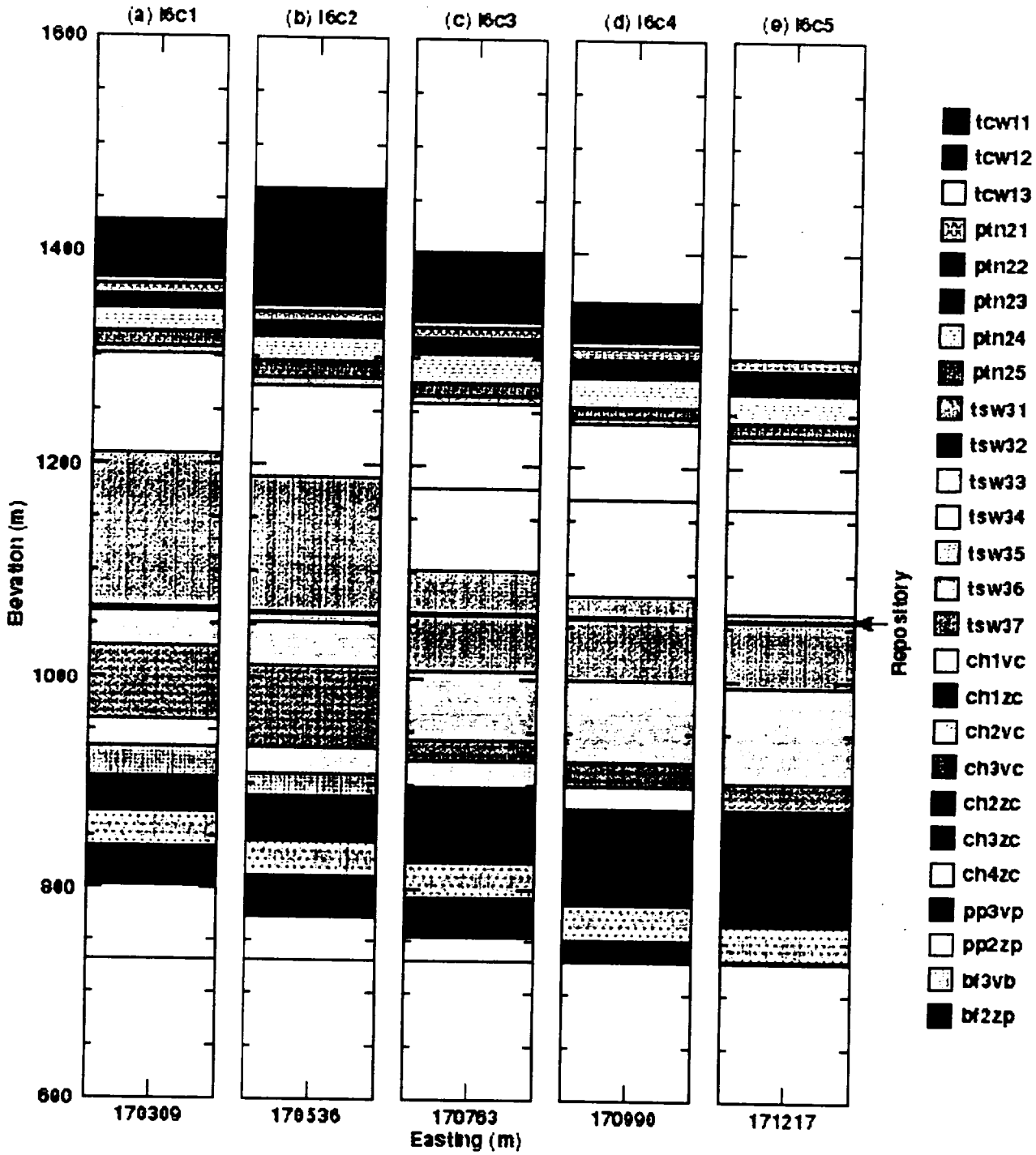

Figure 3-37. Vertical distribution of hydrostratigraphic model units shown for drift-scale model locations (in Nevada-State coordinates), including (a) I6c1 at Northing = 234663 m, (b) I6c2 at Northing = 234651 m, (c) I6c3 at Northing = 234639 m, (d) I6c4 at Northing = 234627 m, and (e) I6c5 at Northing = 234615 m (Hardin 1998).

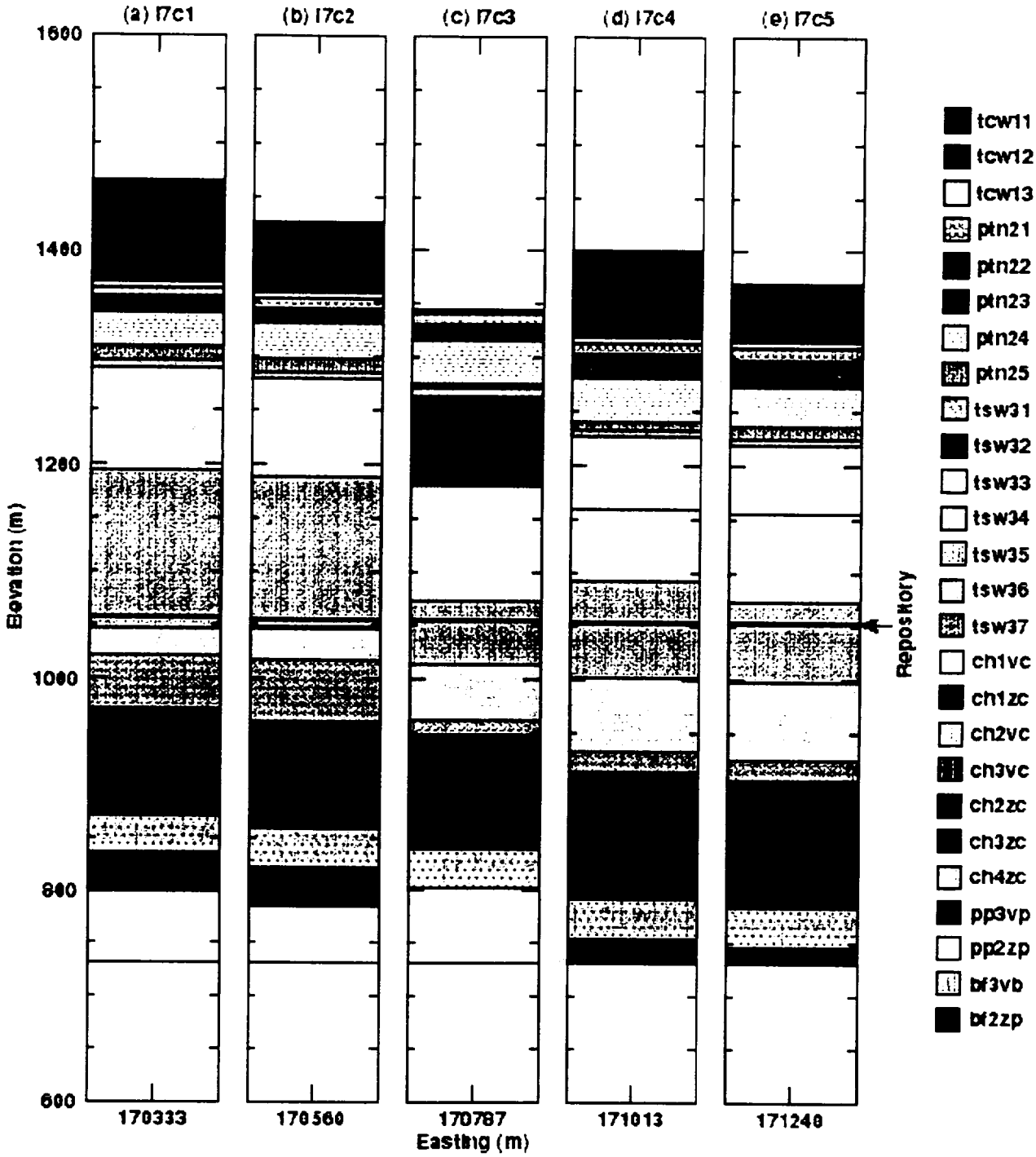

Figure 3-38. Vertical distribution of hydrostratigraphic model units shown for drift-scale model locations (in Nevada-State coordinates), including (a) I7c1 at Northing = 235114 m, (b) I7c2 at Northing = 235102 m, (c) I7c3 at Northing = 235090 m, (d) I7c4 at Northing = 235078 m, and (e) I7c5 at Northing = 235066 m (Hardin 1998).

Typical Emplacement Drift Segment
85 MTU/acre (CSNF)

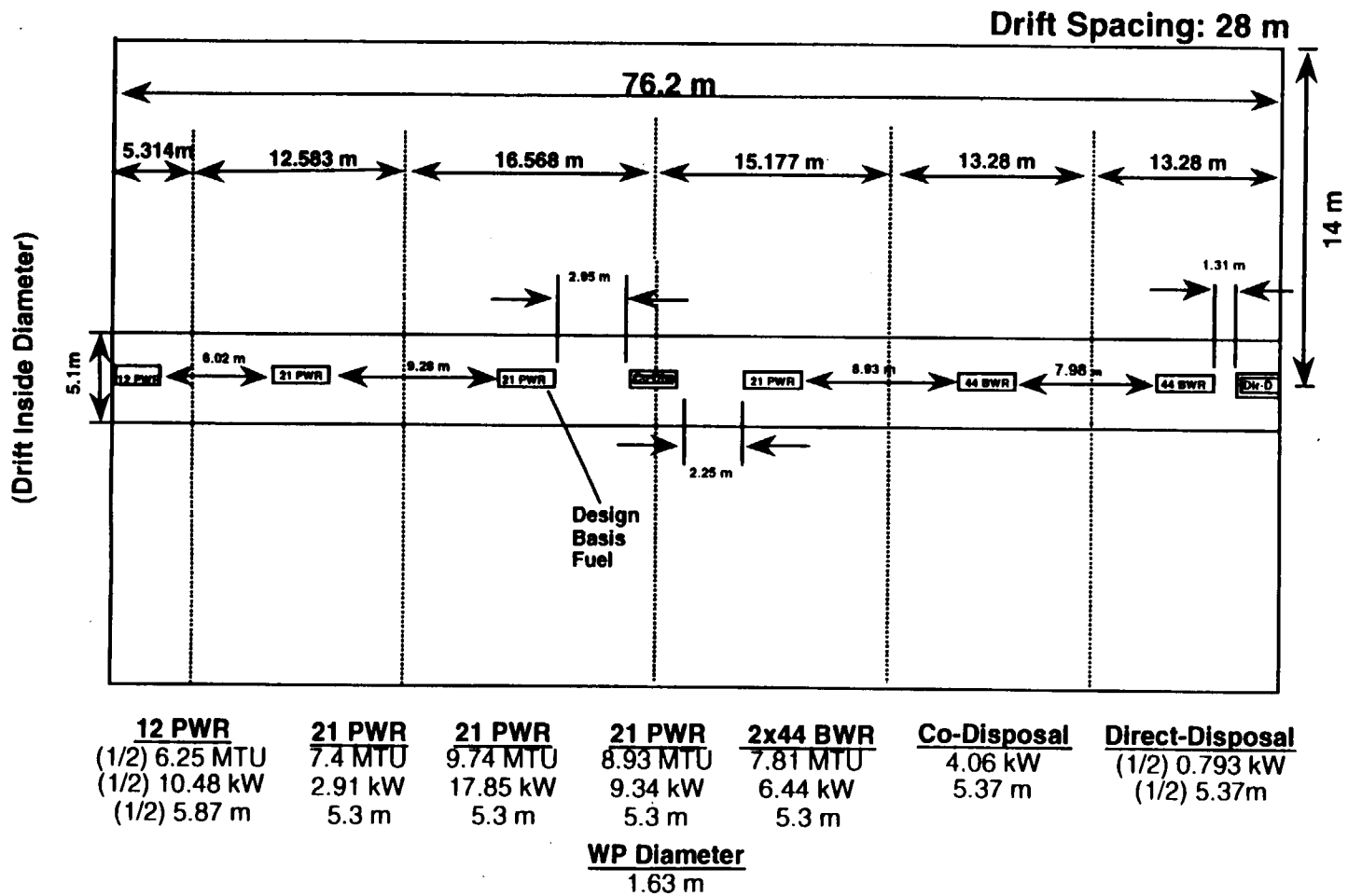

12 PWR	21 PWR	21 PWR	21 PWR	2x44 BWR	Co-Disposal	Direct-Disposal
(1/2) 6.25 MTU	7.4 MTU	9.74 MTU	8.93 MTU	7.81 MTU	4.06 kW	(1/2) 0.793 kW
(1/2) 10.48 kW	2.91 kW	17.85 kW	9.34 kW	6.44 kW	5.37 m	(1/2) 5.37m
(1/2) 5.87 m	5.3 m	5.3 m	5.3 m	5.3 m		

WP Diameter
1.63 m

Figure 3-39. Drift-scale model emplacement drift segment.

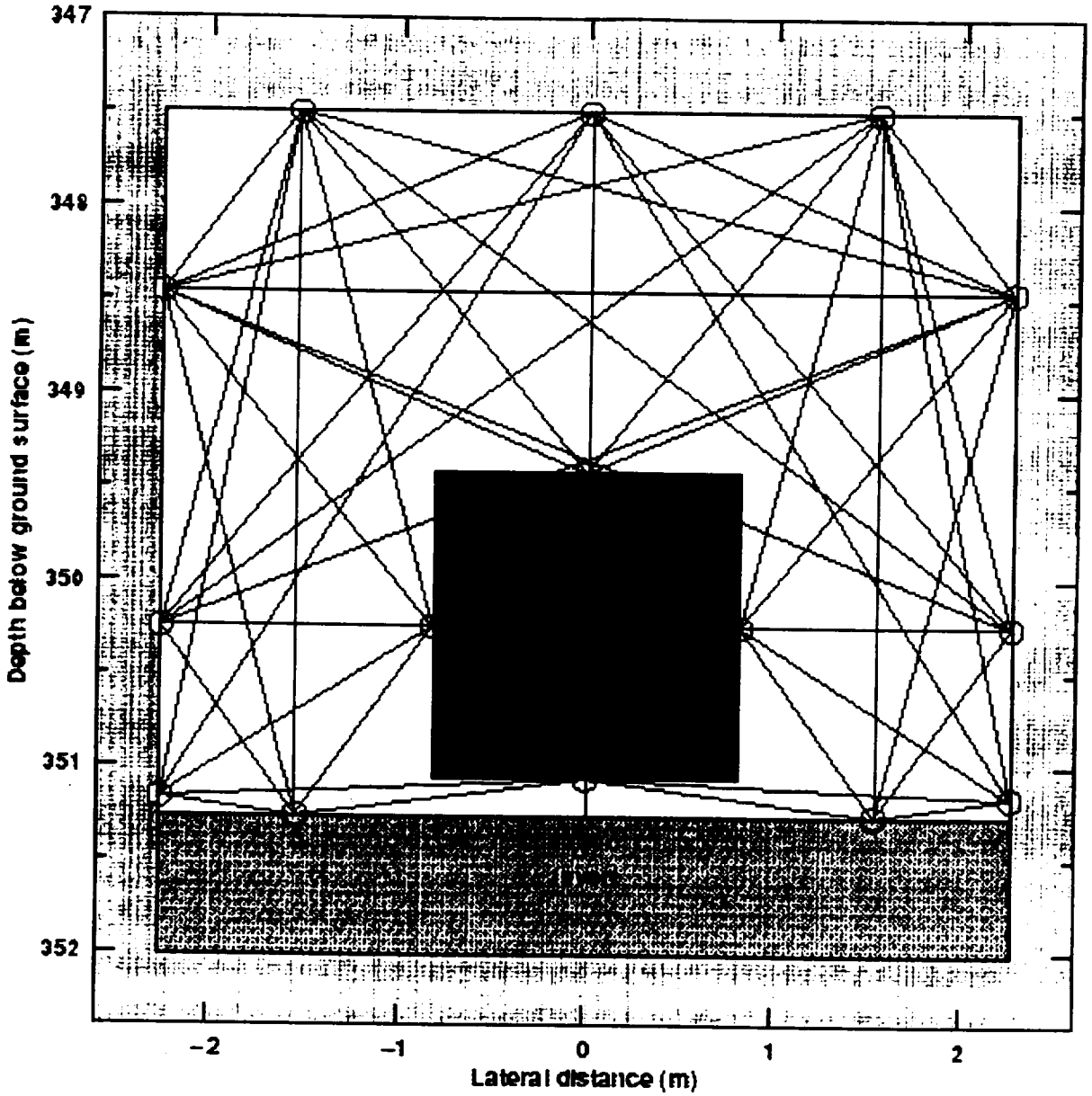

Figure 3-40. Vertical cross-section of the emplacement drift in the DDT and LDTH model showing the thermal radiation connections among the surfaces in the drift that are used in thermal simulations (Hardin 1998).

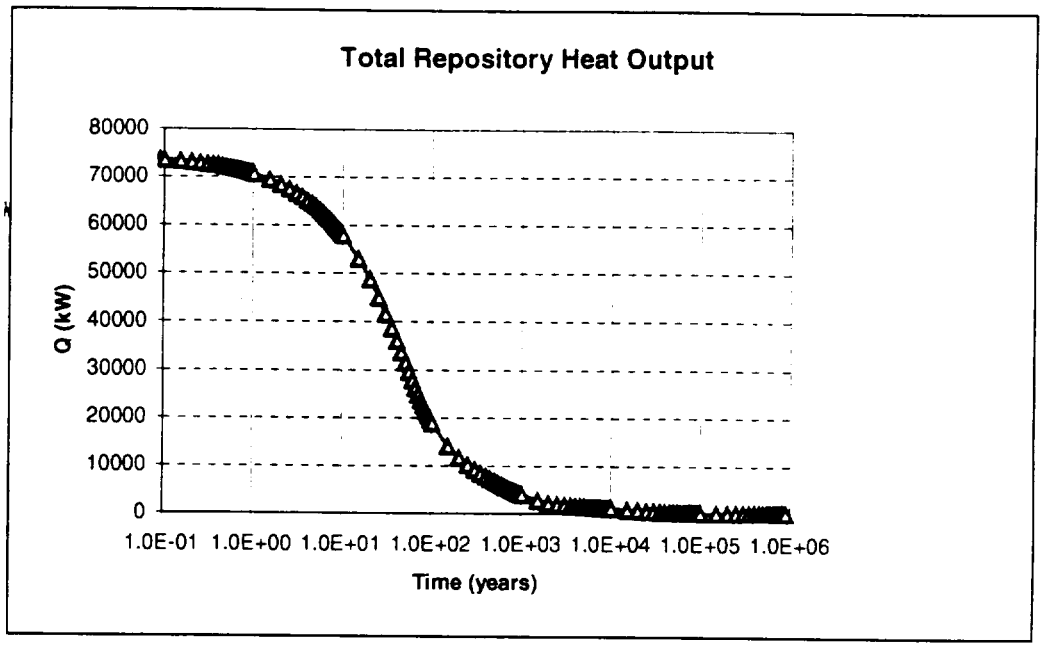

Figure 3-41. Repository-wide heat output based on average characteristics of all fuel types.

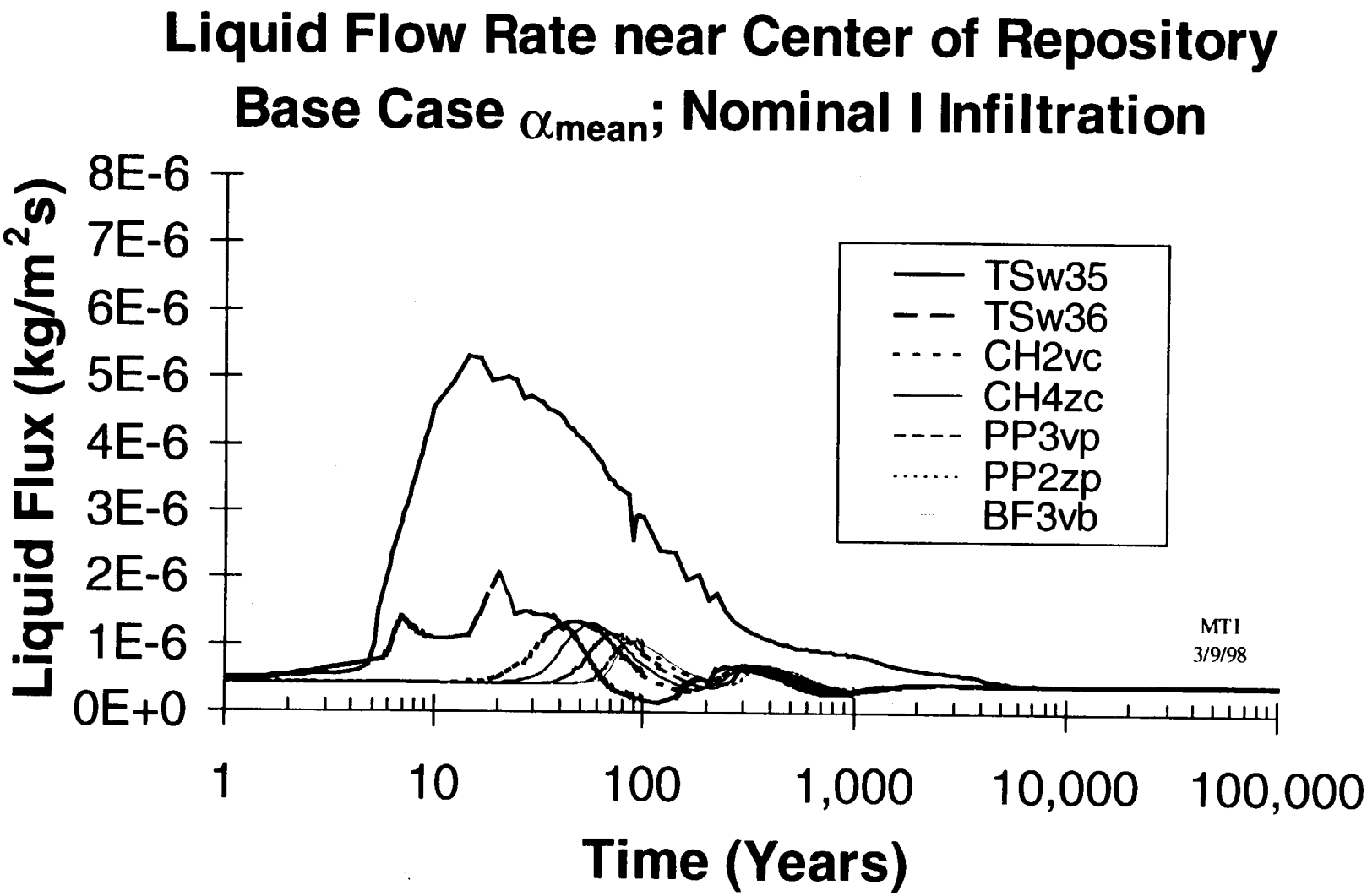

Figure 3-42. Vertical liquid flux rate through various geologic layers below the center of the repository. Base case a_f mean property set at Nominal I infiltration.

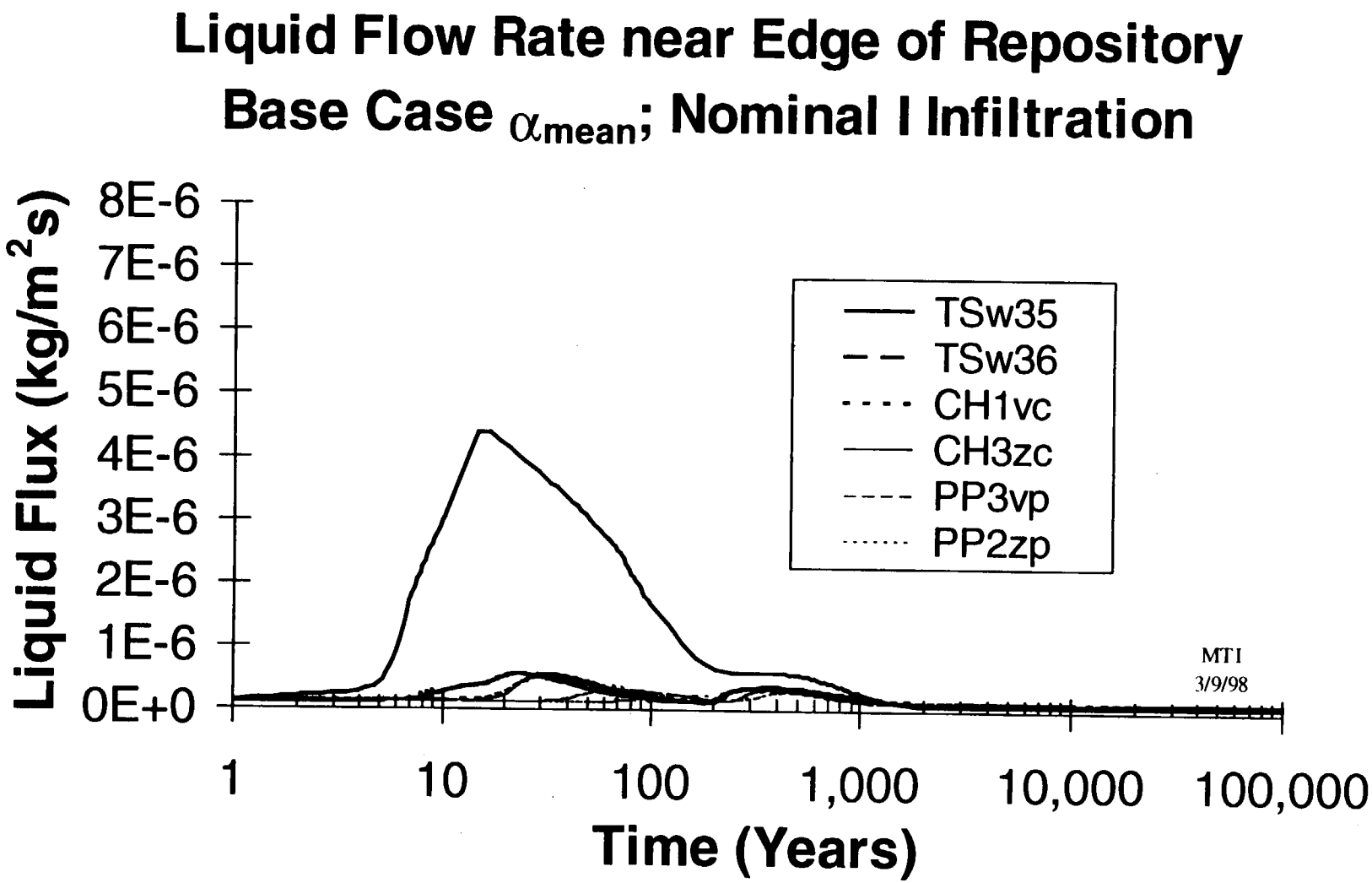

Figure 3-43. Vertical liquid flux rate through various geologic layers below the eastern edge of the repository. Base case a_l mean property set at Nominal I infiltration.

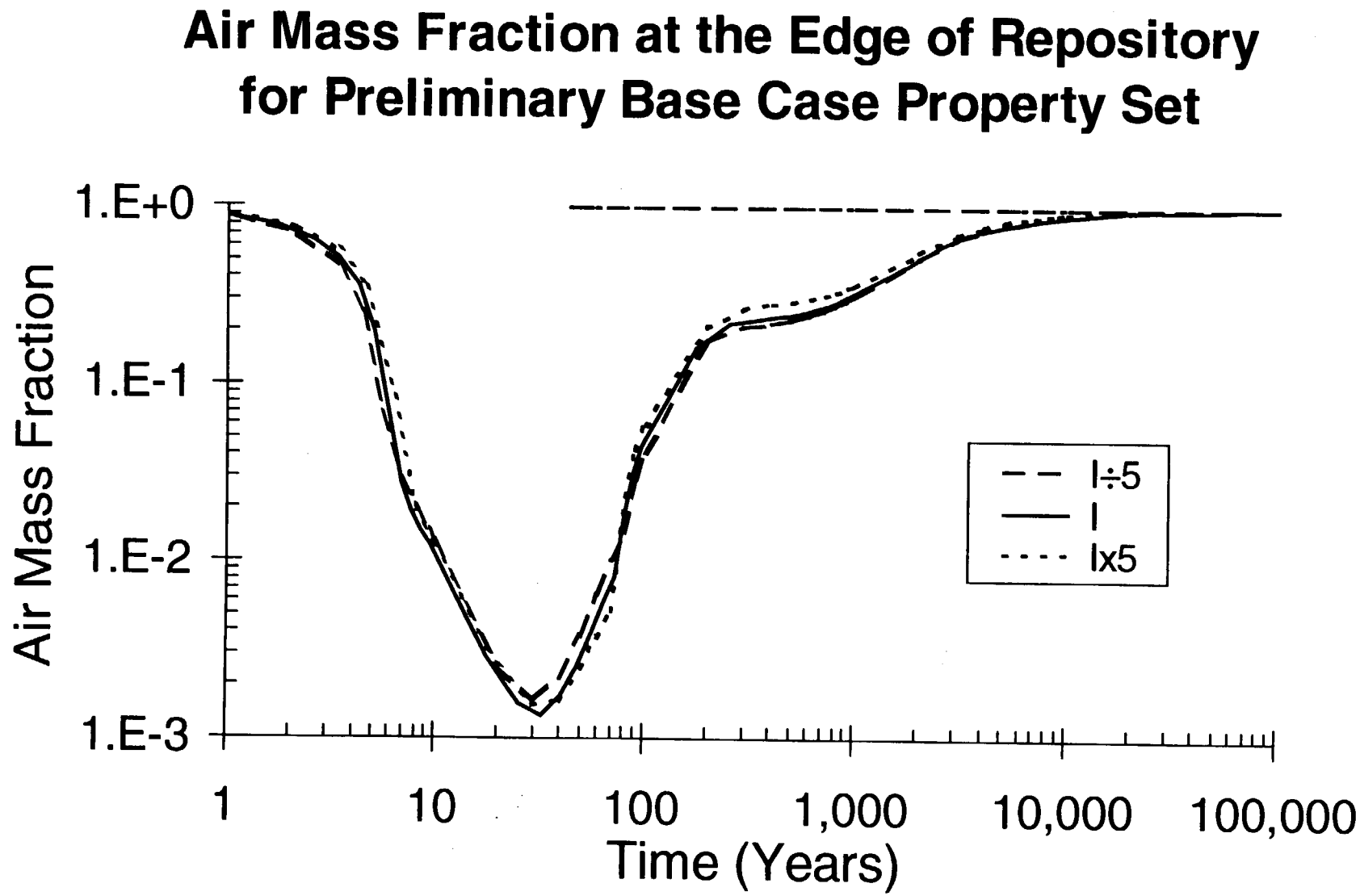

Figure 3-44. Air mass fraction at the edge of the repository for the preliminary base-case property set at the present day infiltration rate.

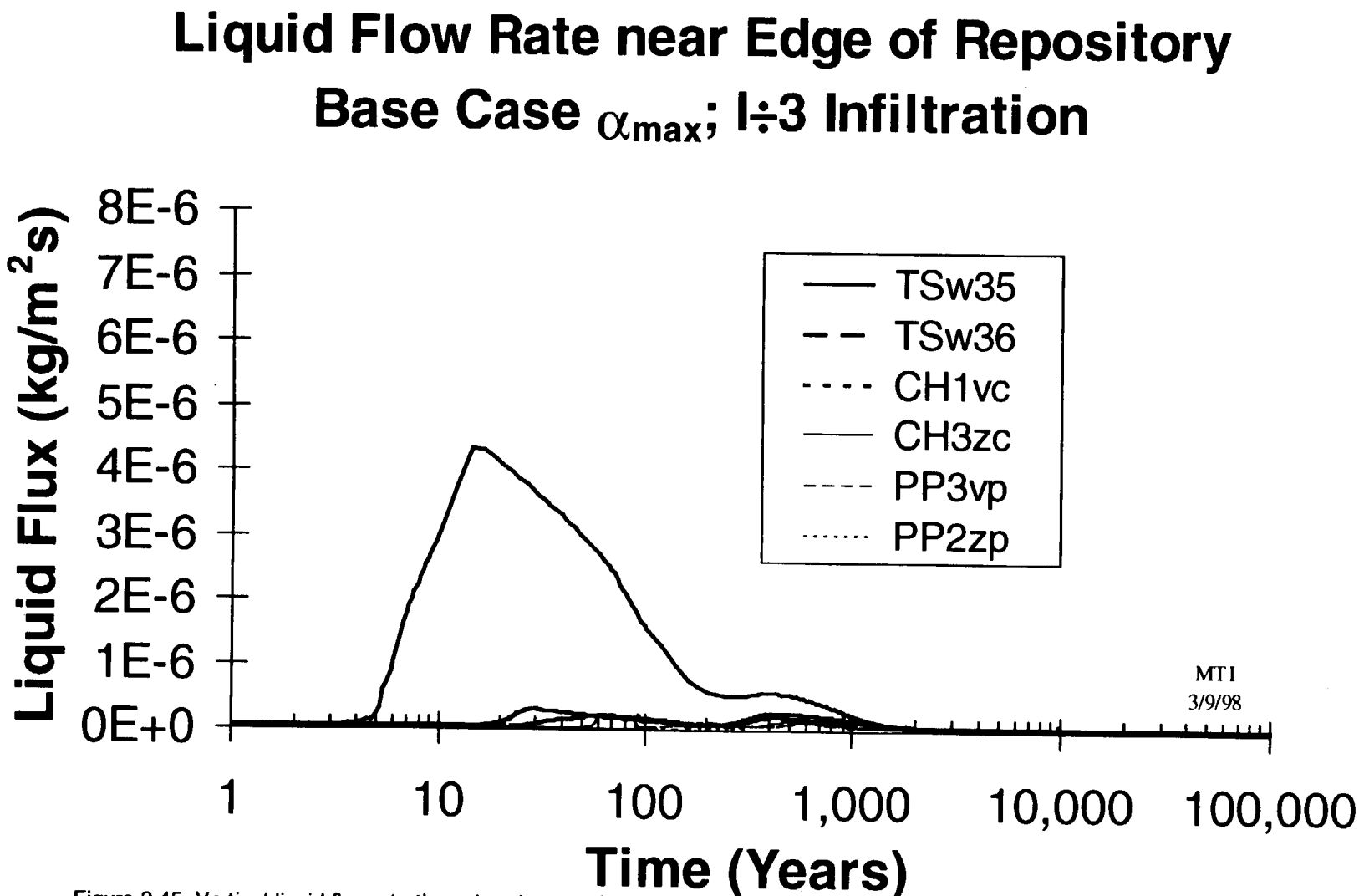

Figure 3-45. Vertical liquid flux rate through various geologic layers below the eastern edge of the repository. Base case a_f max property set at I÷3 infiltration.

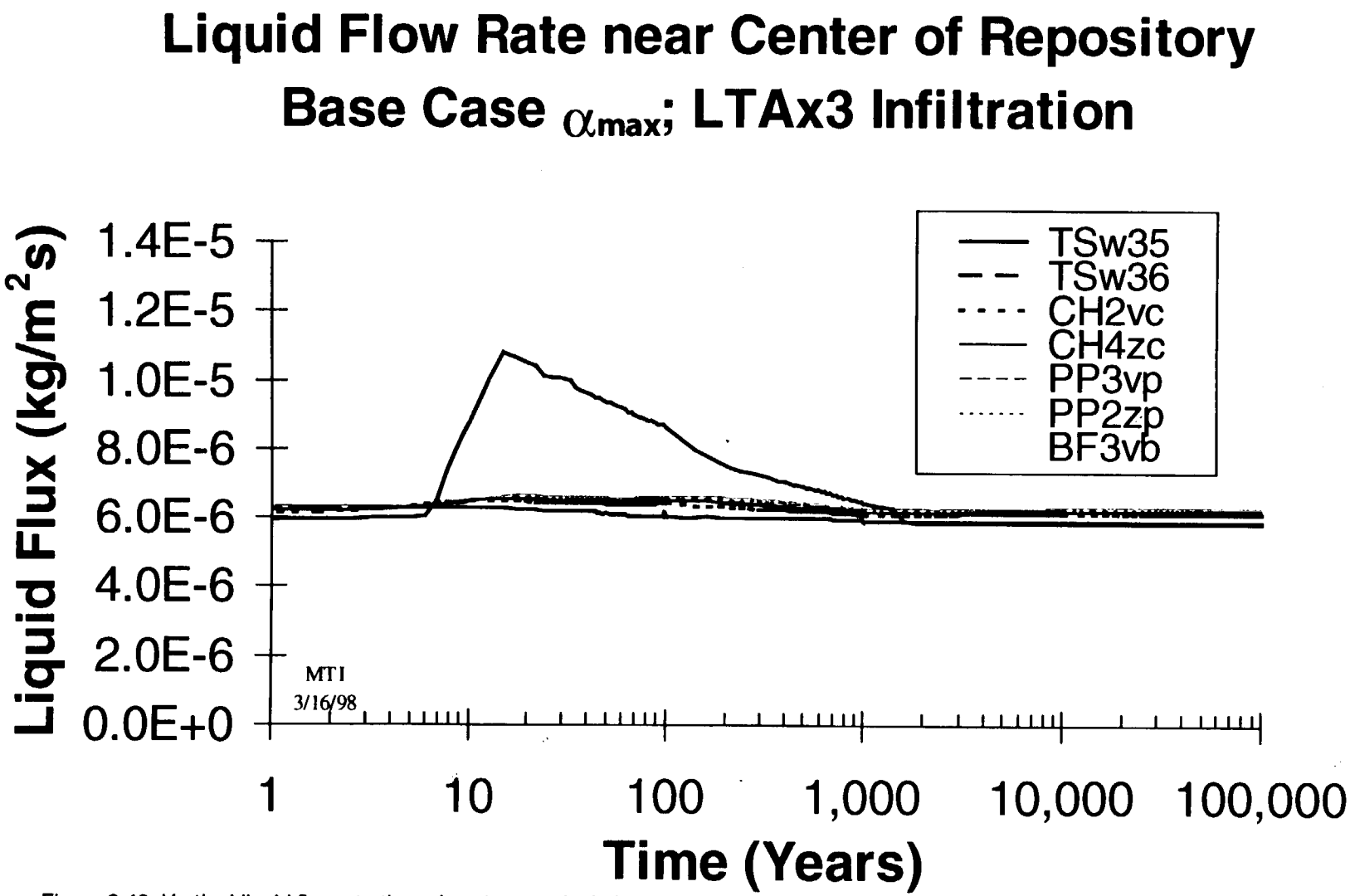

Figure 3-46. Vertical liquid flux rate through various geologic layers below the center of the repository. Base case a_f max property set at three times long term average infiltration.

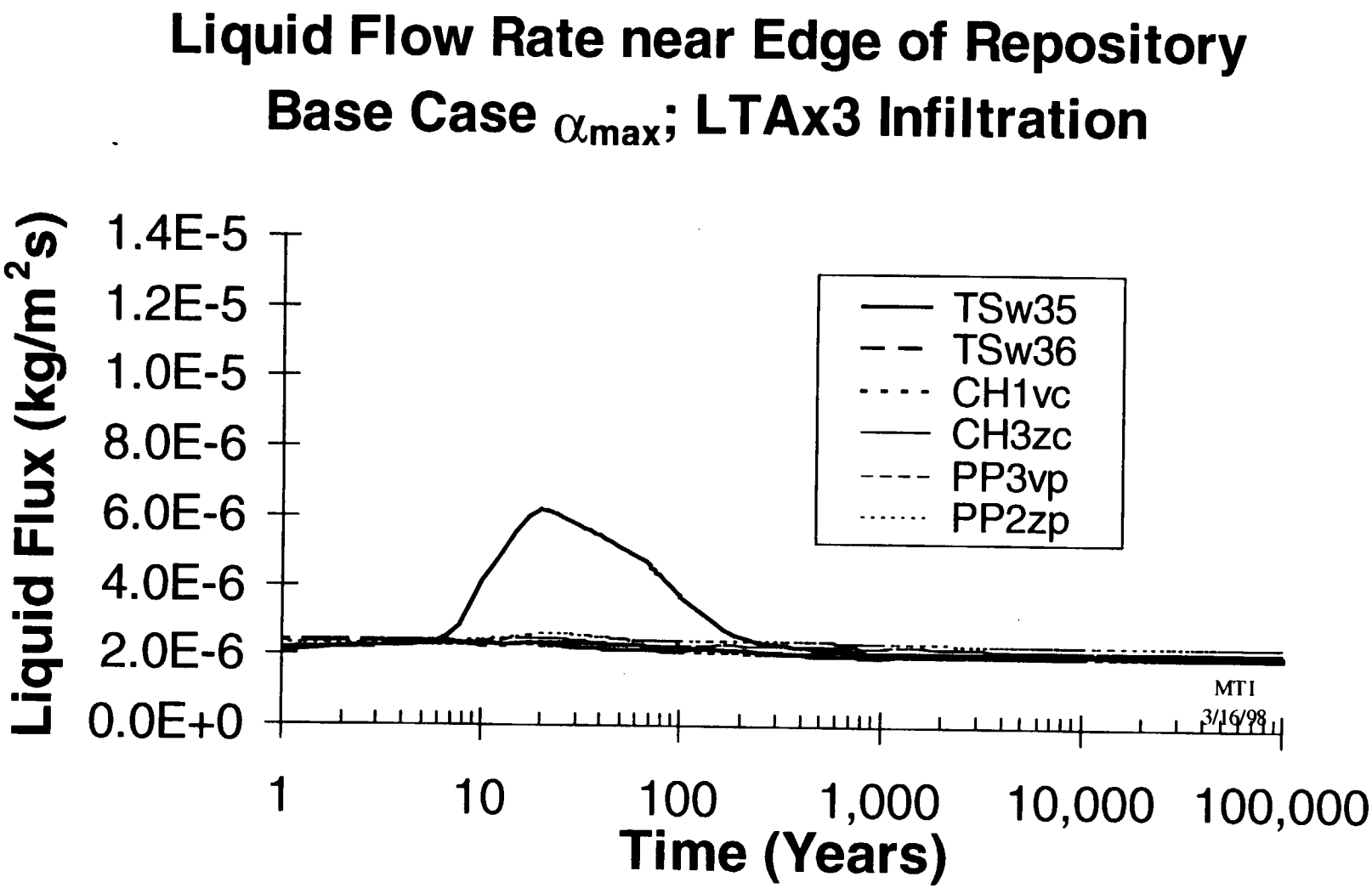

Figure 3-47. Vertical liquid flux rate through various geologic layers below the eastern edge of the repository. Base case a_f max property set at three times long term average infiltration.

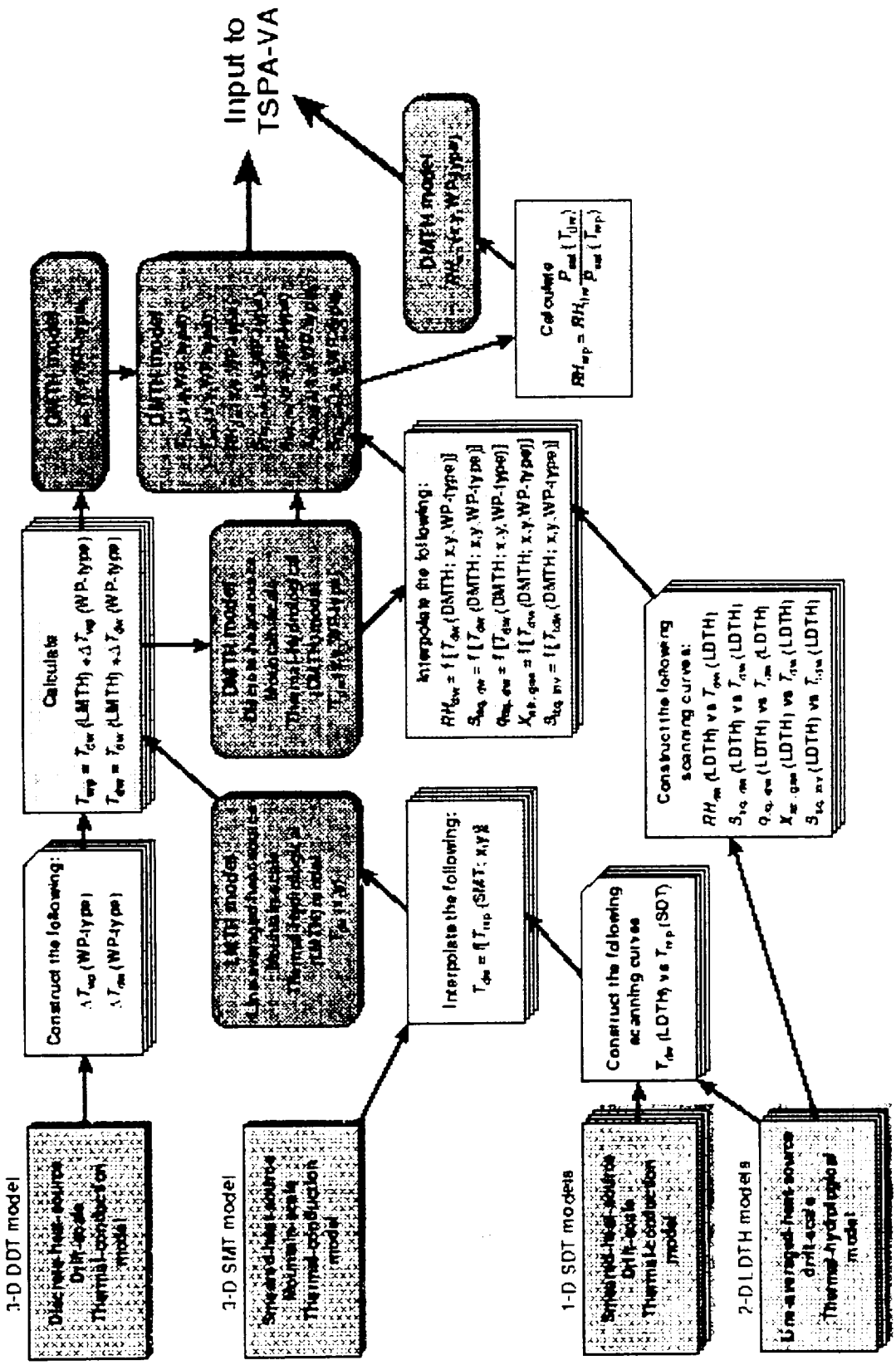

Figure 3-48. Flow chart for the TH multiscale modeling and abstraction method for (a) cases with no engineered backfill and (b) cases with engineered backfill (Hardin 1998).

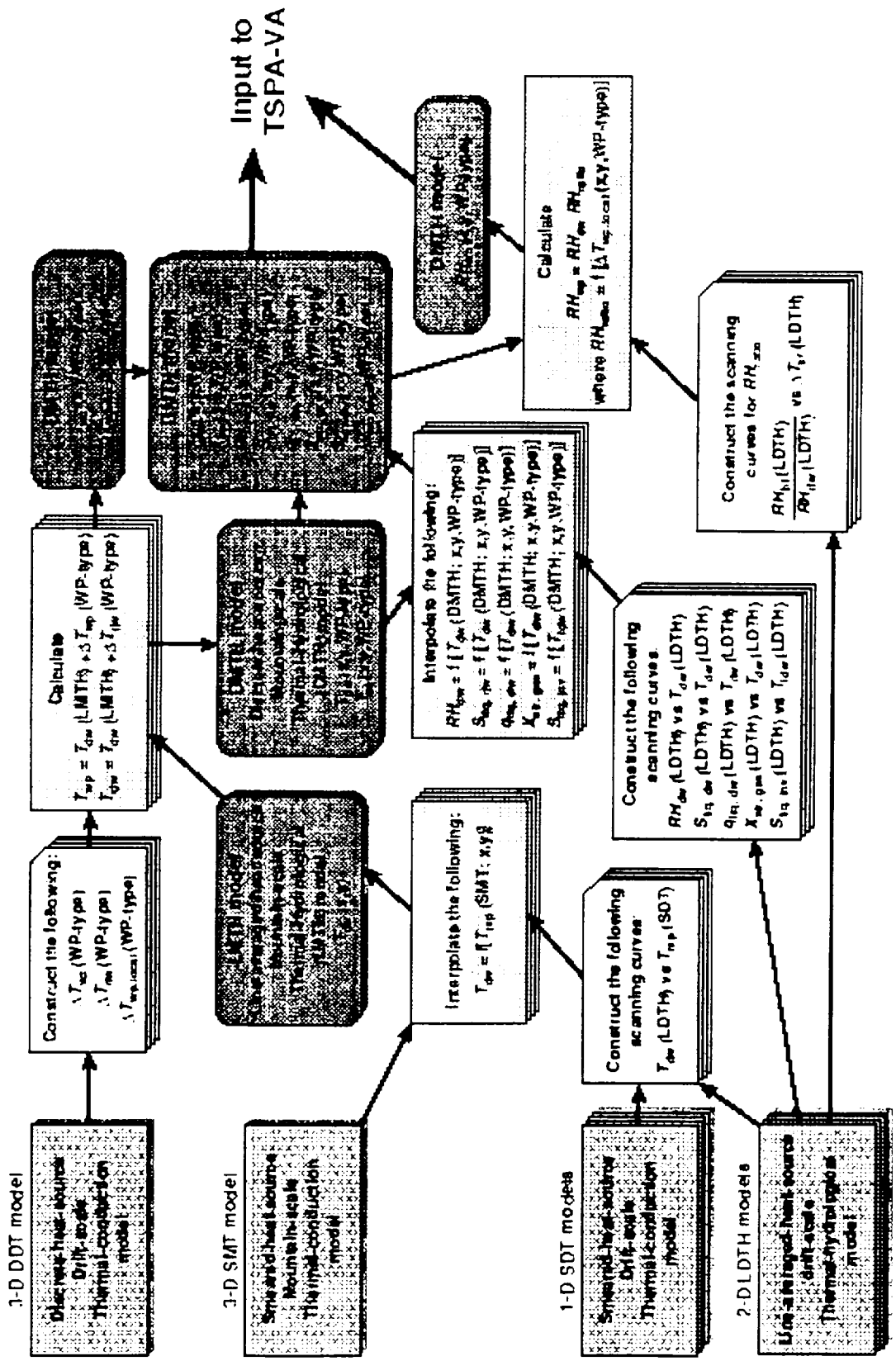

Figure 3-49. Flow chart for the TH multiscale modeling and abstraction method for (a) cases with no engineered backfill and (b) cases with engineered backfill (Hardin 1998).

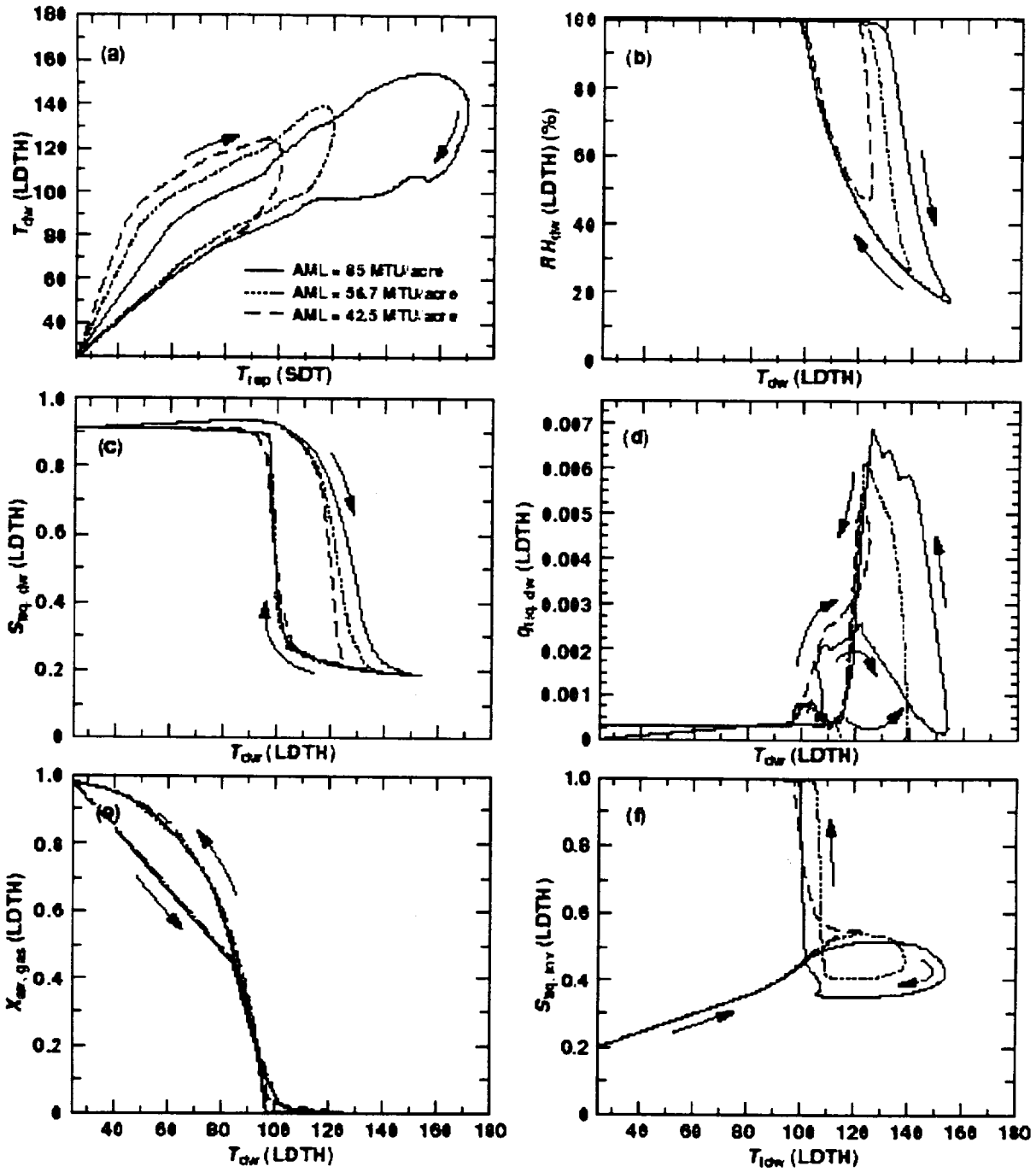

Figure 3-50 (a-f). Functional relations plotted for the process-model inputs to the TH multiscale modeling and abstraction method: (a) LDTH-model-predicted drift-wall temperature T_{dw} (LDTH) vs. SDT-model-predicted repository host-rock temperature T_{rep} (SDT), (b) LDTH-model-predicted drift-wall relative humidity RH_{dw} (LDTH) vs. T_{dw} (LDTH), (c) LDTH-model-predicted drift-wall liquid-phase saturation $S_{liq,dw}$ (LDTH) vs. T_{dw} (LDTH), (d) LDTH-model predicted liquid-phase flux 3 m above the drift $q_{liq,dw}$ (LDTH) vs. T_{dw} (LDTH), (e) LDTH-model-predicted gas-phase air-mass fraction in the drift $X_{air,dr}$ (LDTH) vs. T_{dw} (LDTH), (f) LDTH-model-predicted liquid-phase saturation in the invert $S_{liq,inv}$ (LDTH) vs. T_{dw} (LDTH) (Hardin 1998).

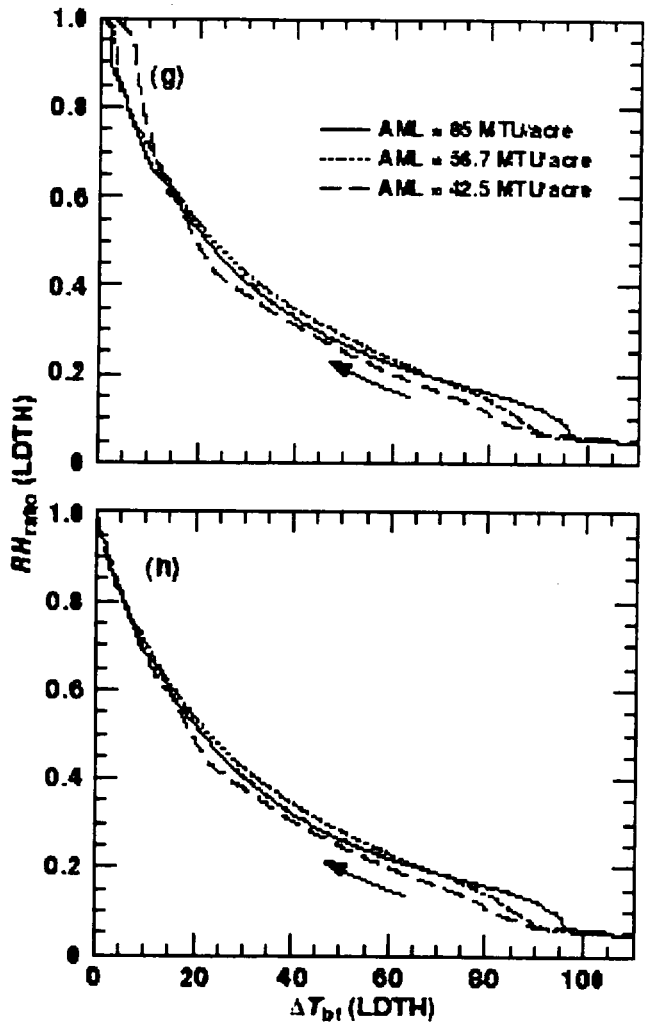

Figure 3-50 (g-h). Functional relations plotted for the process-models inputs to the TH multiscale modeling and abstraction method: (g) RH_{ratio}(LDTH) vs. ΔT_{bf}(LDTH), where RH_{ratio}(LDTH) = RH_{bf}(LDTH)/RH_{dw}(LDTH) and ΔT_{bf}(LDTH) = T_{bf}(LDTH) - T_{dw}(LDTH), where RH_{bf} and T_{bf} are the LDTH-model-predicted, backfill relative humidity and temperature, respectively, averaged over the perimeter of the WP and RH_{dw} and T_{dw} are the LDTH-model-predicted, drift-wall relative humidity and temperature, respectively, averaged over the perimeter of the drift wall. Functional relations are given for the point-load design with (g) crushed-tuff backfill and (h) quartz-sand backfill.

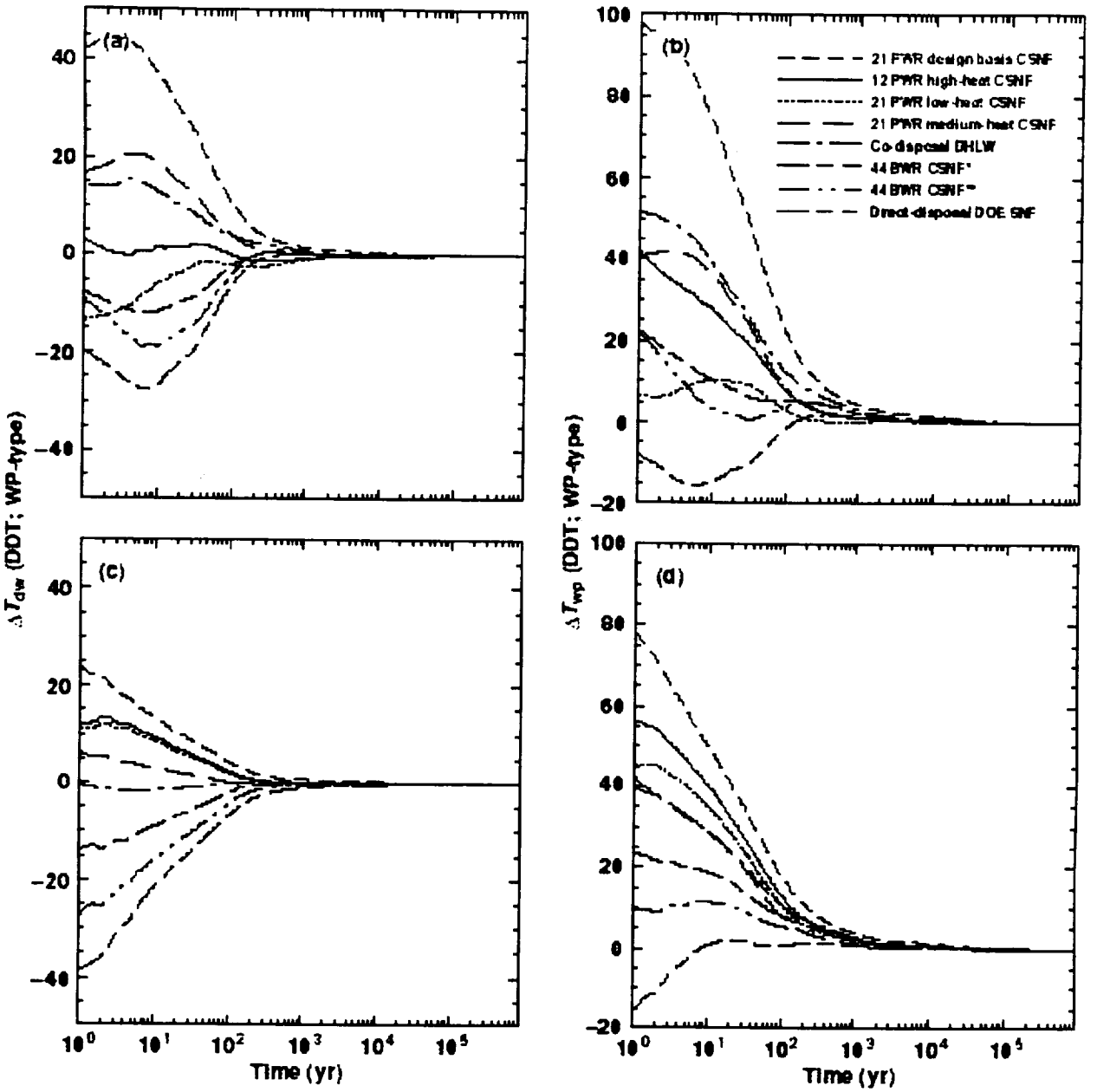

Figure 3-51 (a-d). Functional relations plotted for the process-model inputs to the TH multiscale modeling and abstraction method as functions of time: (a) WP-type/location-specific temperature deviations ΔT_{dw} (WP-type) from the average drift-wall temperature along the drift and (b) WP-type/location-specific temperature difference ΔT_{wp} (WP-type) between the WP surface and the average drift-wall temperature along the drift for the point-load design. The relations for ΔT_{dw} (WP-type) (c) and ΔT_{wp} (WP-type) (d) are also given for the line-load design (Hardin 1998).

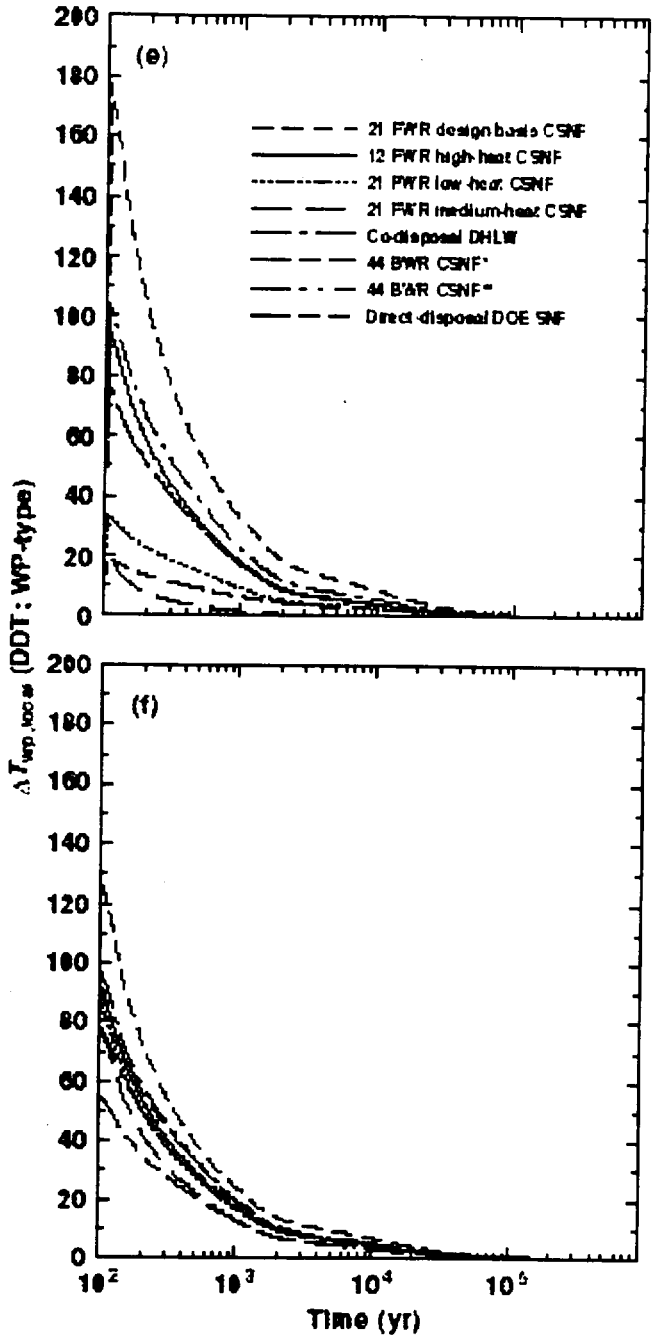

Figure 3-51 (e-f). Functional relations plotted for the process-models inputs to the TH multiscale modeling and abstraction method: (e) $\Delta T_{wp,local}$(DDT; WP-type) = T_{wp}(DDT; WP-type) - $T_{dw,local}$(DDT; WP-type), where T_{wp} is the DDT-model-predicted WP temperature and $T_{dw,local}$ is the DDT-model-predicted, local, drift-wall temperature for a given WP location, plotted for the point-load design. (f) The relation for $\Delta T_{wp,local}$(DDT; WP-type) is also plotted for the line-load design.

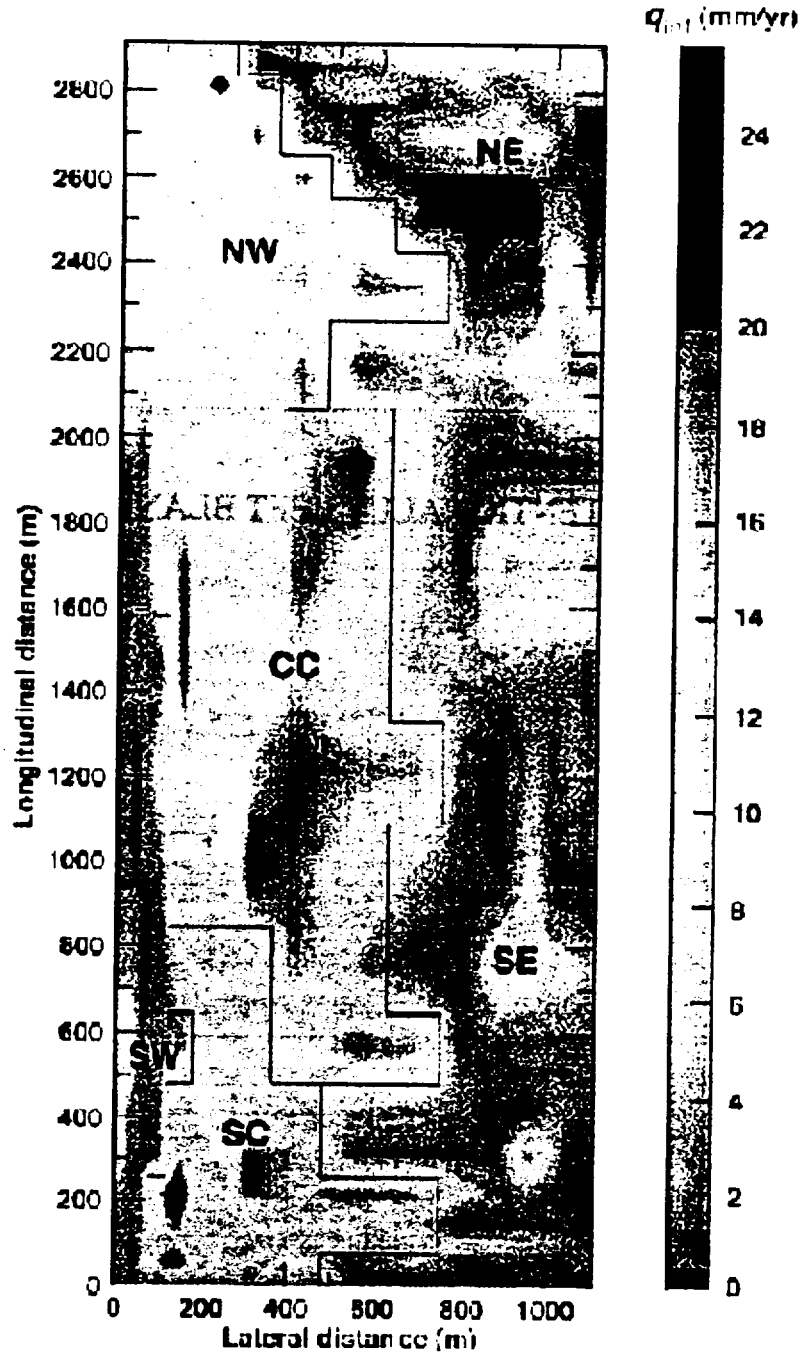

Figure 3-52. The six infiltration-flux subdomains and the infiltration-flux q_{inf} distribution (Flint et al., 1996a) shown for the SMT-model representation of the repository area (infiltration-flux subdomains used to bin the WP environments for EBS subsystem analysis for TSPA-VA): increasing order of mean q_{inf} the subdomains (1) southwest SW, (2) northeast NE, (3) southeast SE, (4) northwest NW, (5) south-central SC, and (6) central-central CC (Hardin 1998).

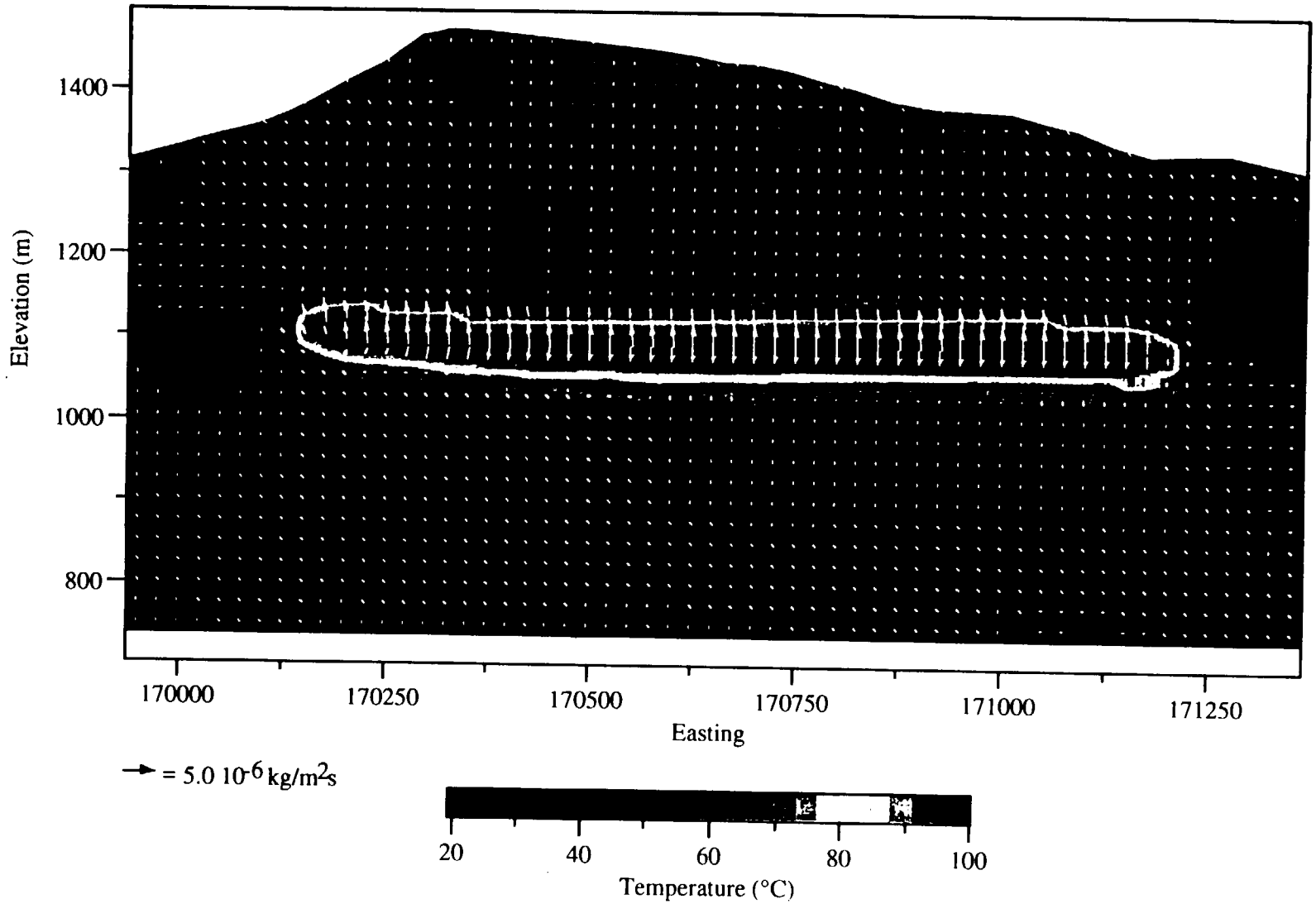

Figure 3-53. Temperature and gas flow fields throughout the simulation domain at 30 years for the two-dimensional mountain-scale TH simulations. Base case α_f-mean nominal I present day infiltration.

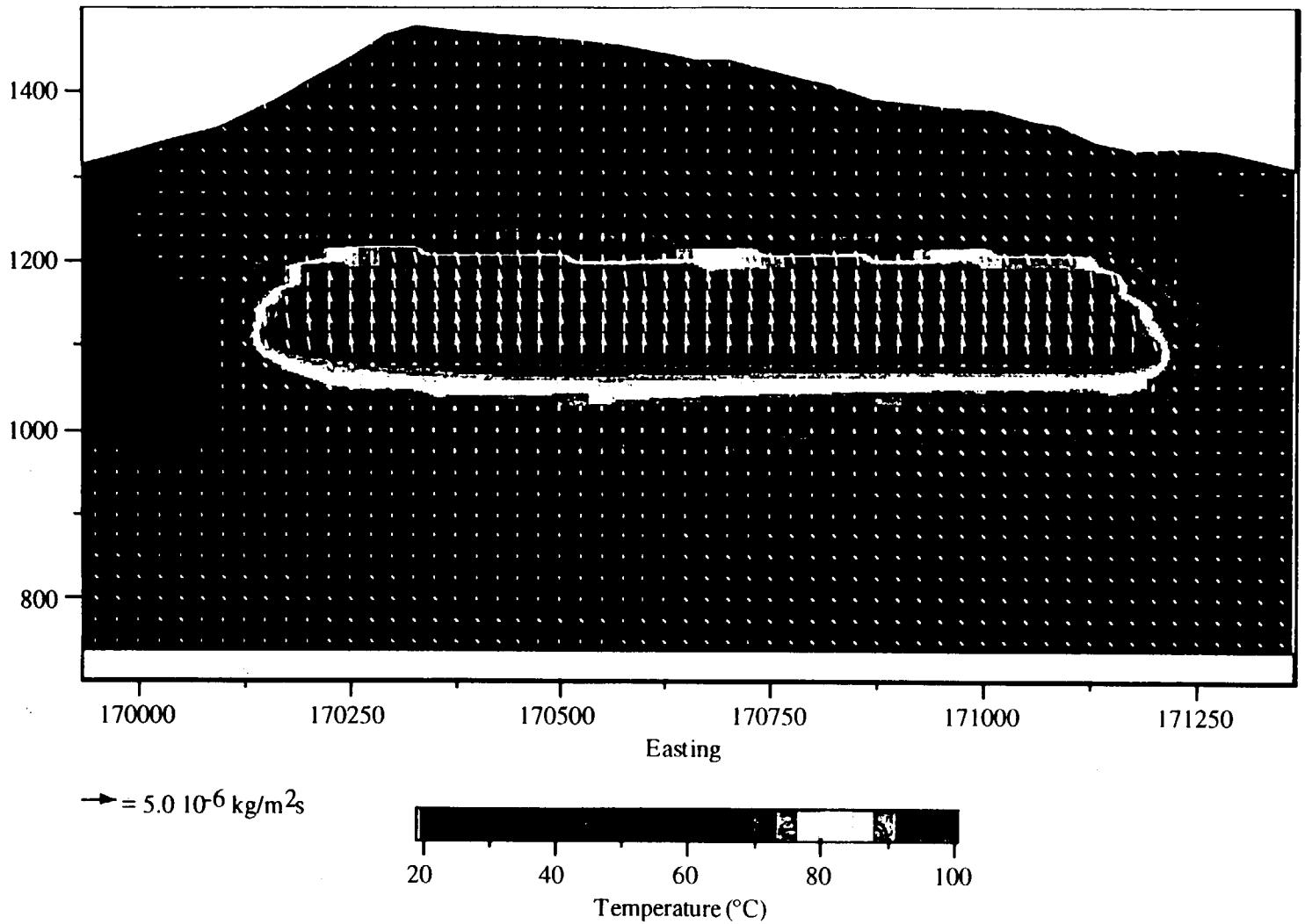

Figure 3-54. Temperature and gas flow fields throughout the simulation domain at 100 years for the two-dimensional mountain-scale TH simulations. Base case α_l-mean nominal I present day infiltration.

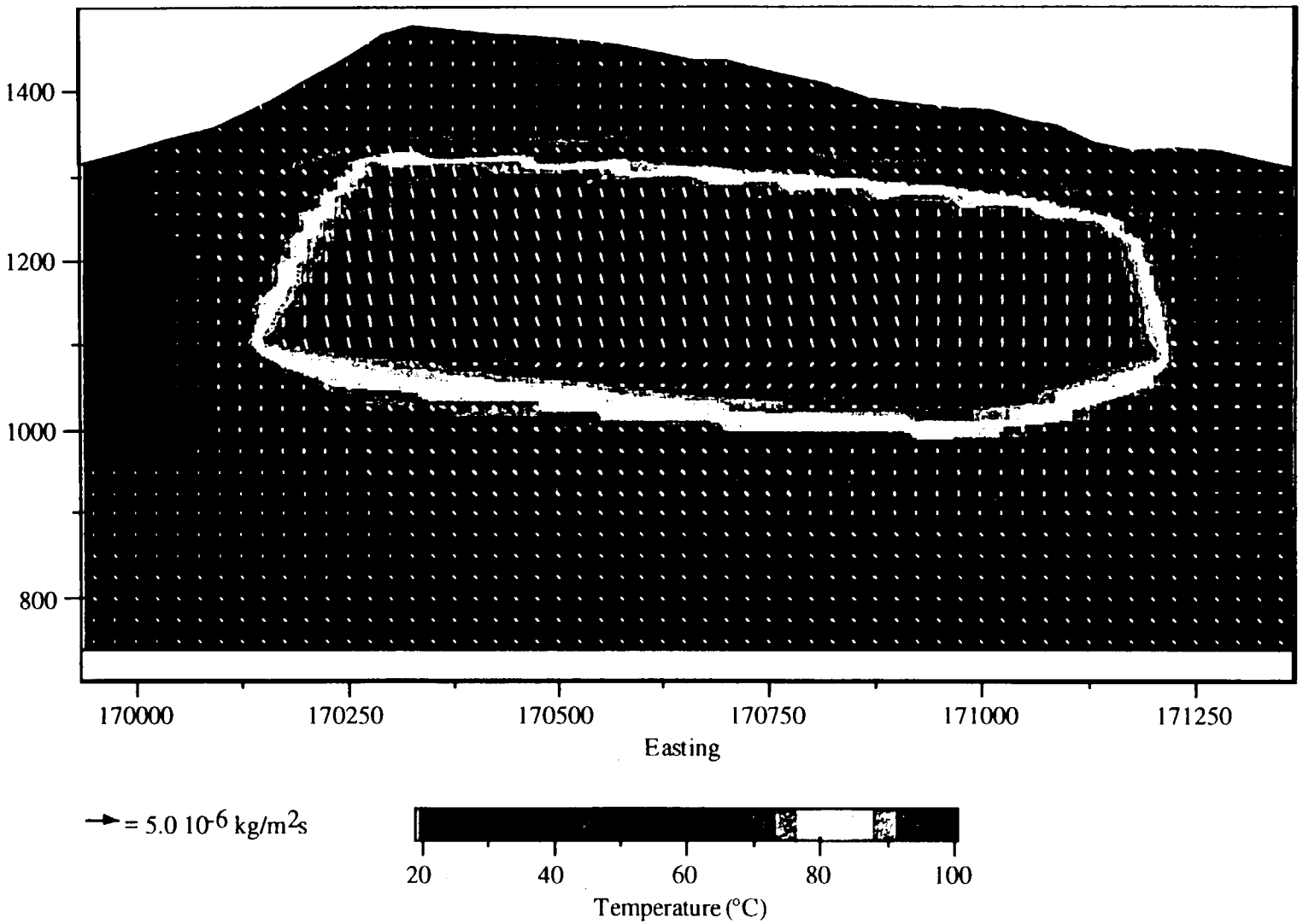

Figure 3-55.Temperature and gas flow fields throughout the simulation domain at 300 years for the two-dimensional mountain-scale TH simulations. Base case α_f-mean nominal I present day infiltration.

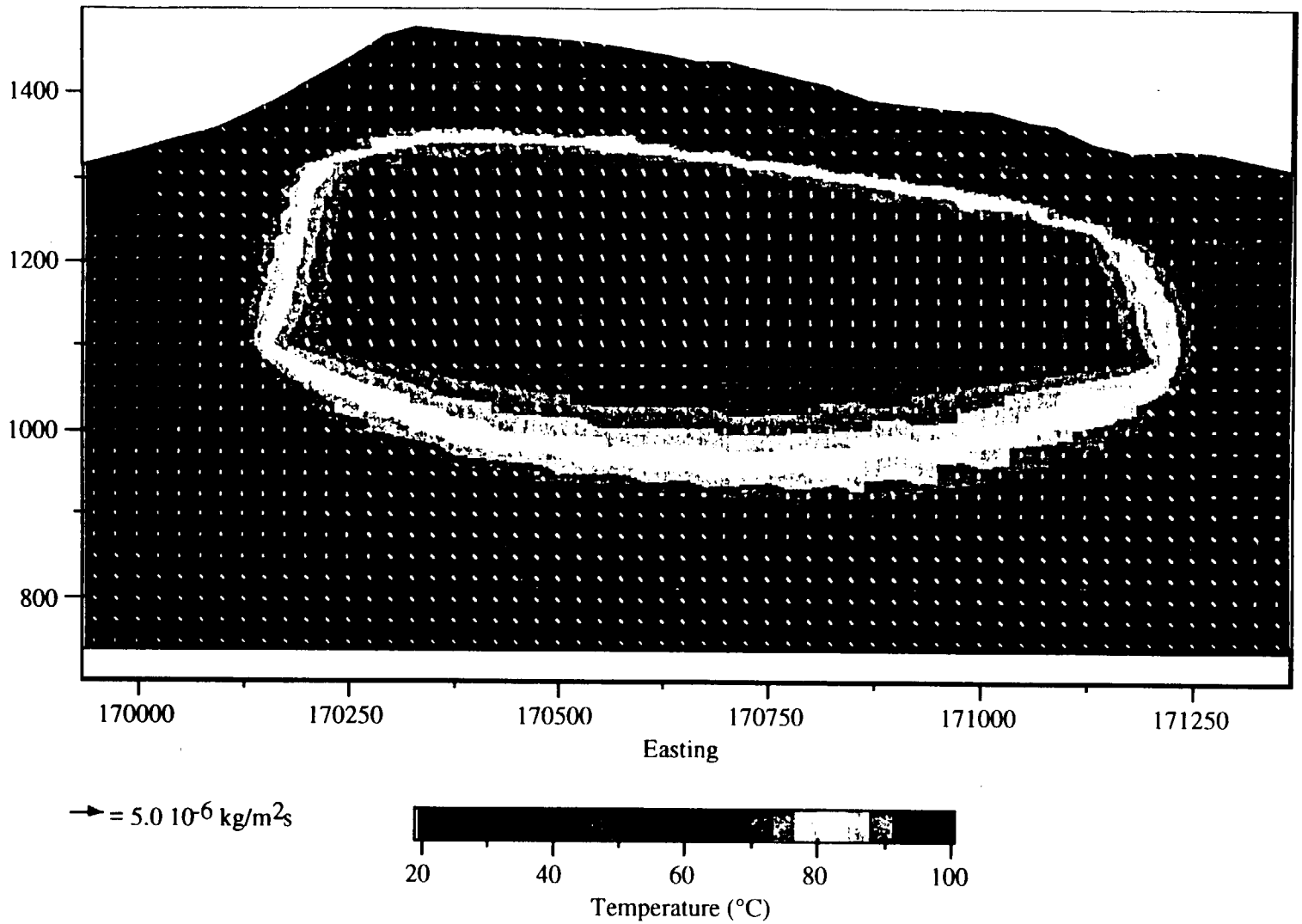

Figure 3-56. Temperature and gas flow fields throughout the simulation domain at 1000 years for the two-dimensional mountain-scale TH simulations. Base case α_f-mean nominal I present day infiltration.

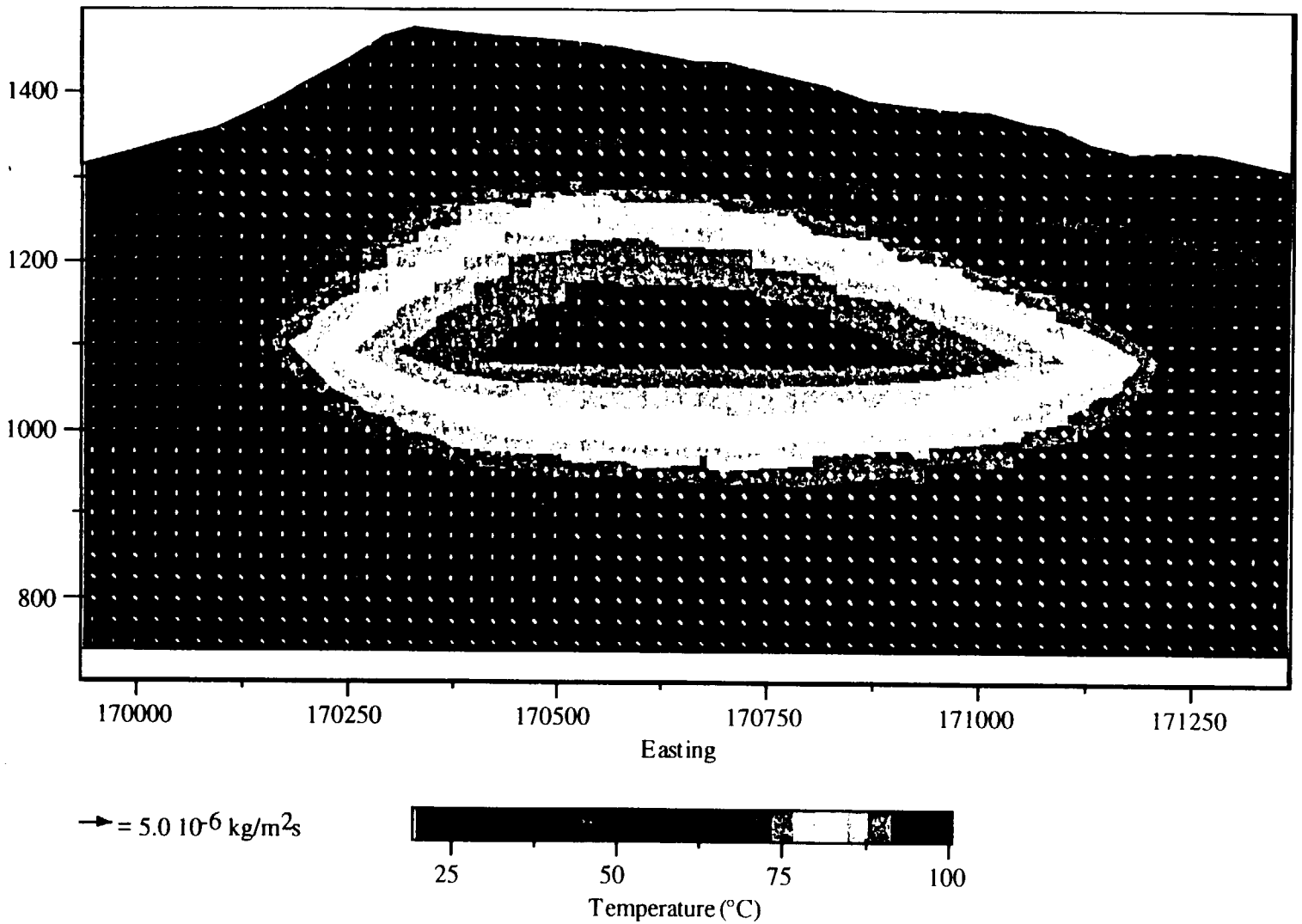

Figure 3-57. Temperature and gas flow fields throughout the simulation domain at 3,000 years for the two-dimensional mountain-scale TH simulations. Base case α_t-mean nominal I present day infiltration.

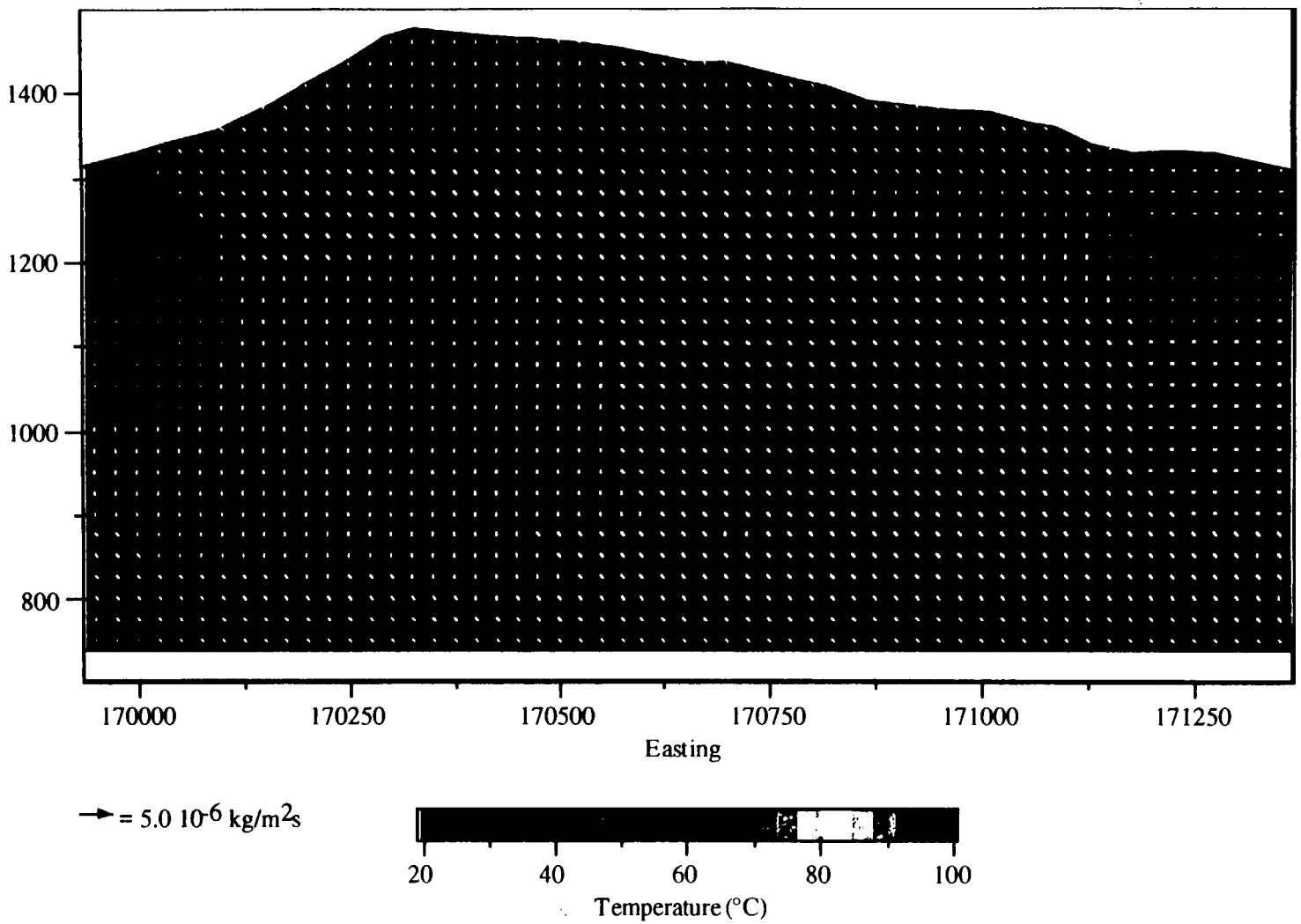

Figure 3-58. Temperature and gas flow fields throughout the simulation domain at 10,000 years for the two-dimensional mountain-scale Th simulations. Base case α_f-mean nominal I present day infiltration.

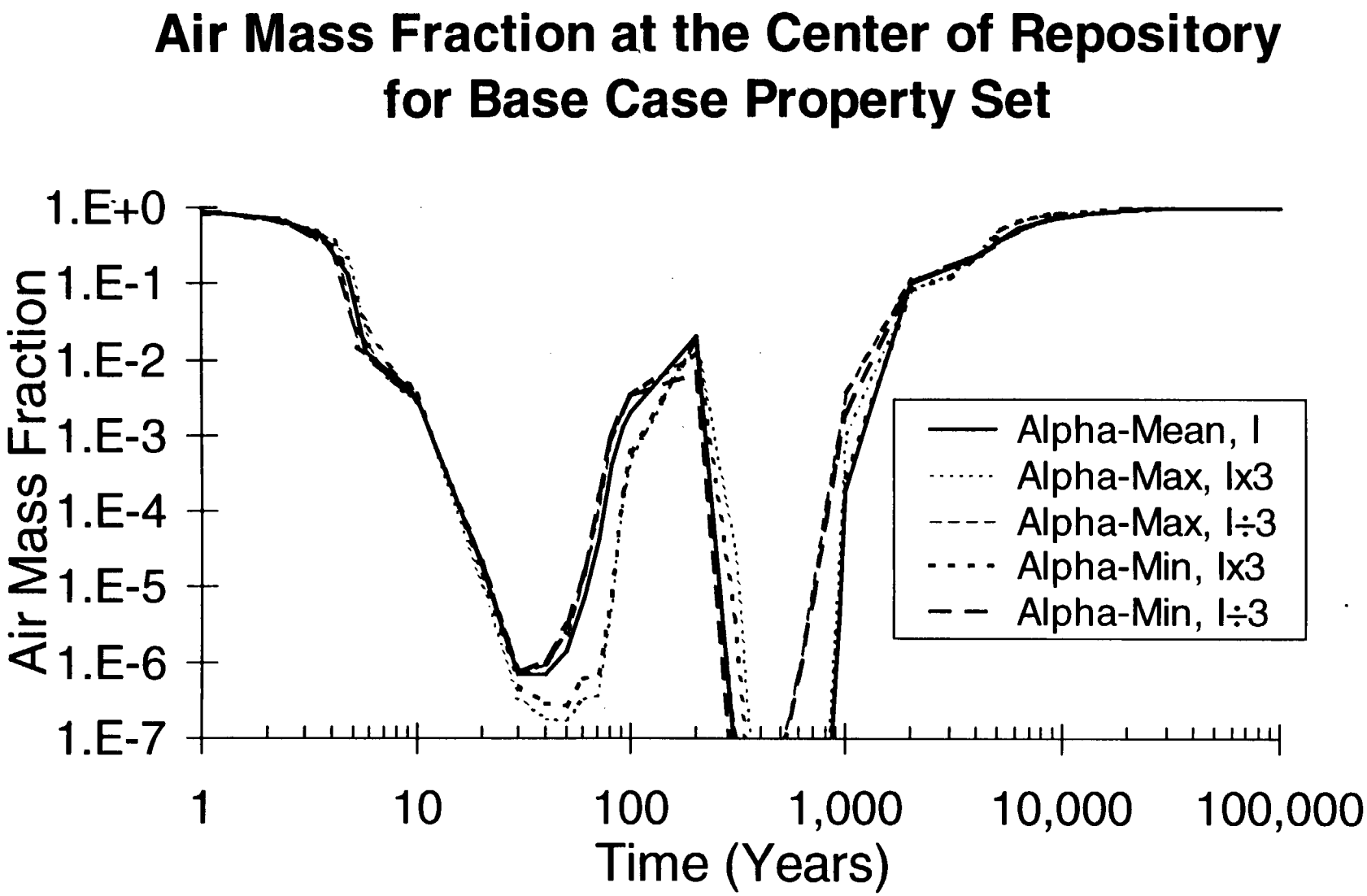

Figure 3-59. Air mass fraction at the center of the repository for the base case property set at the present day infiltration rate.

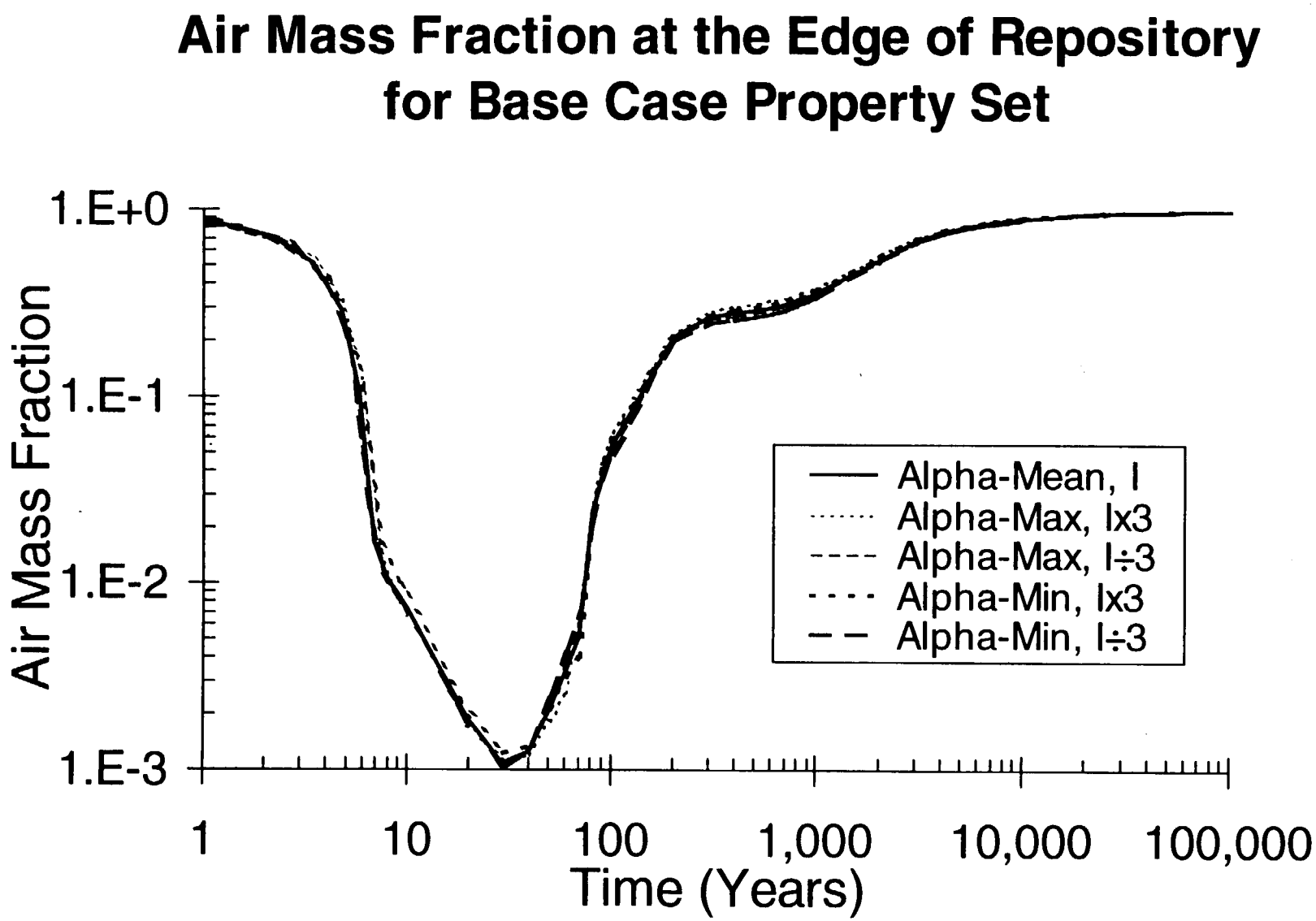

Figure 3-60. Air mass fraction at the edge of the repository for the base case property set at the present day infiltration rate.

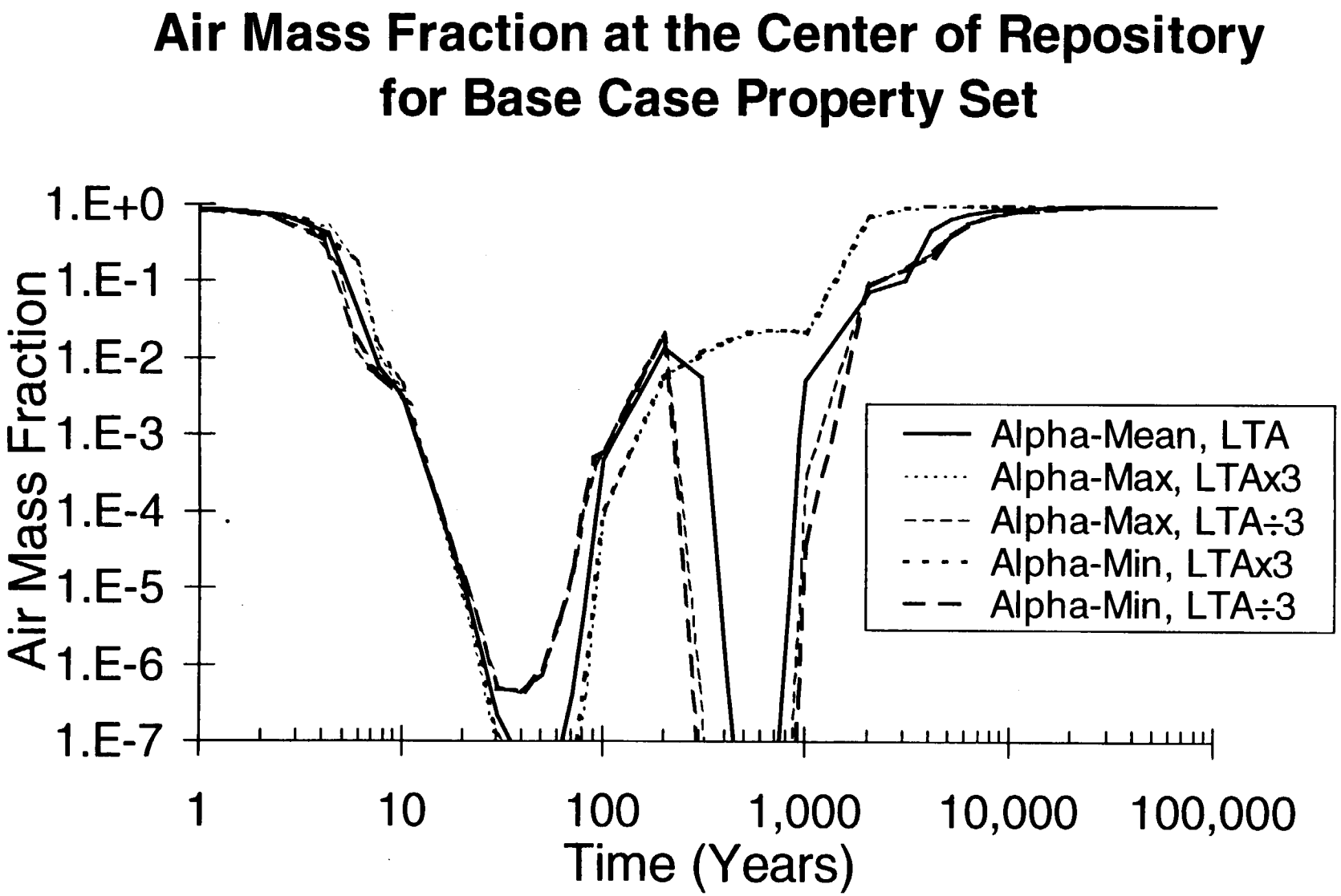

Figure 3-61. Air mass fraction at the center of the repository for the base case property set at the long term average infiltration rate.

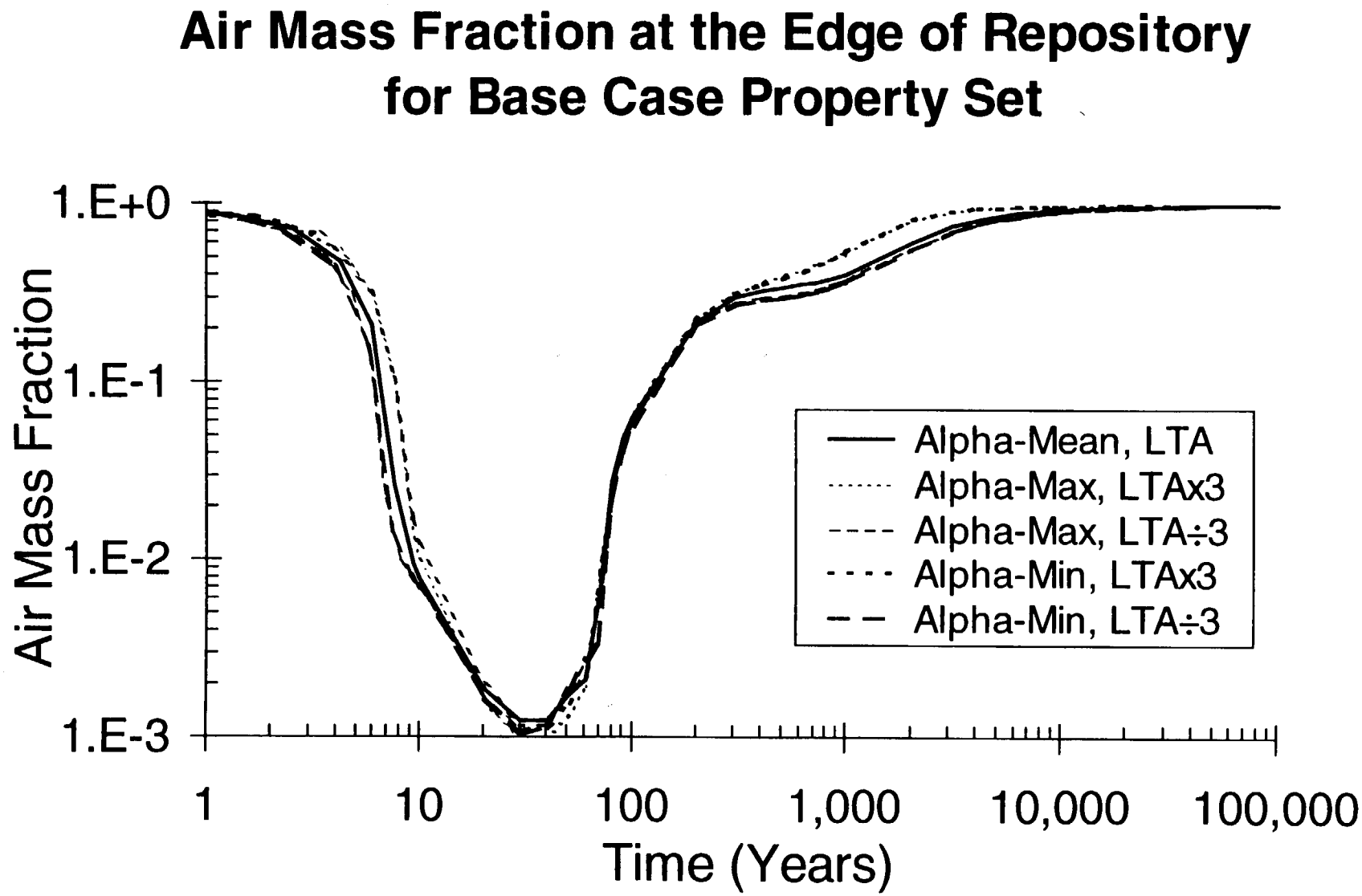

Figure 3-62. Air mass fraction at the edge of the repository for the base case property set at the long term average infiltration rate.

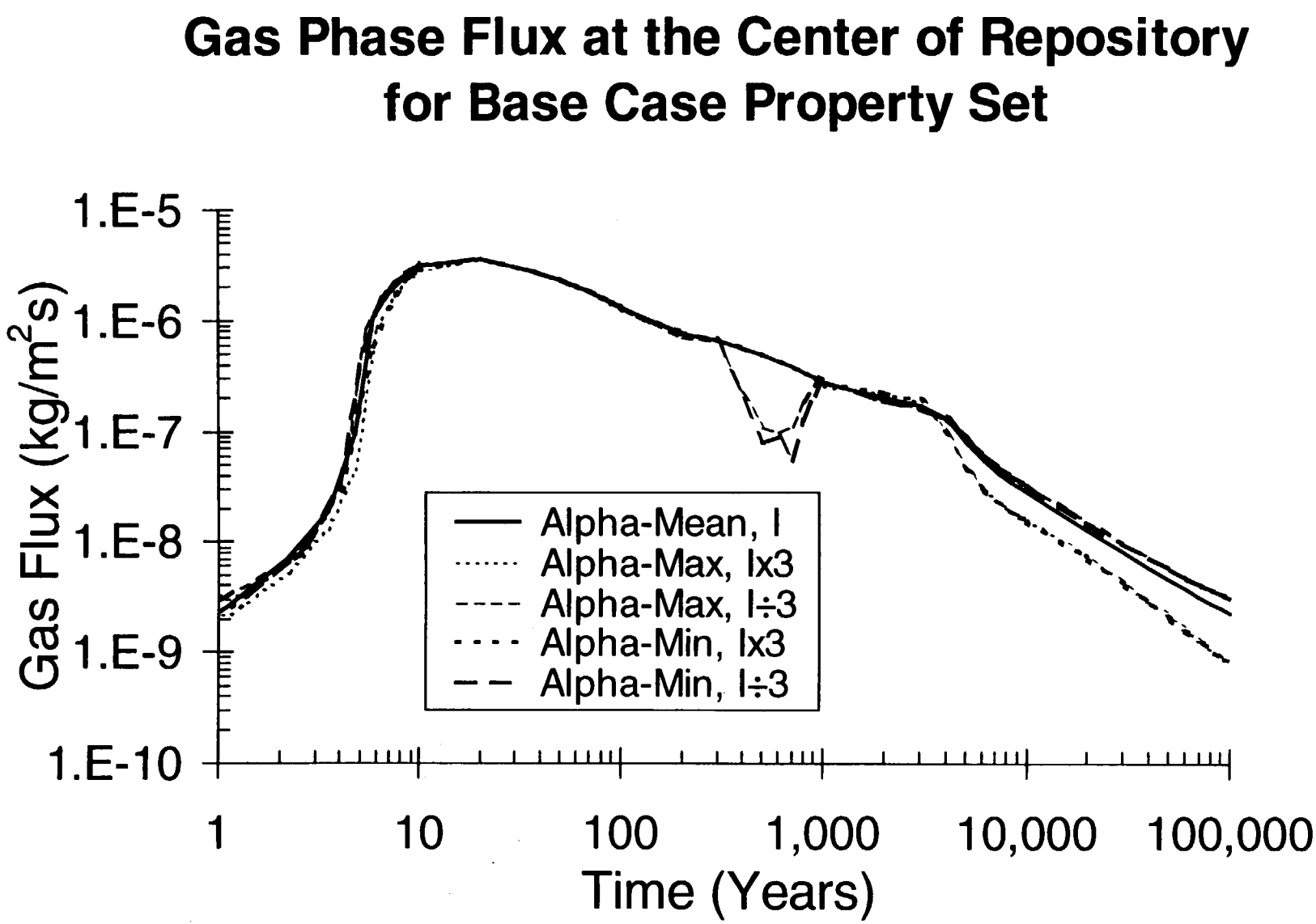

Figure 3-63. Gas flux at the center of the repository for the base case property set at the present day infiltration rate.

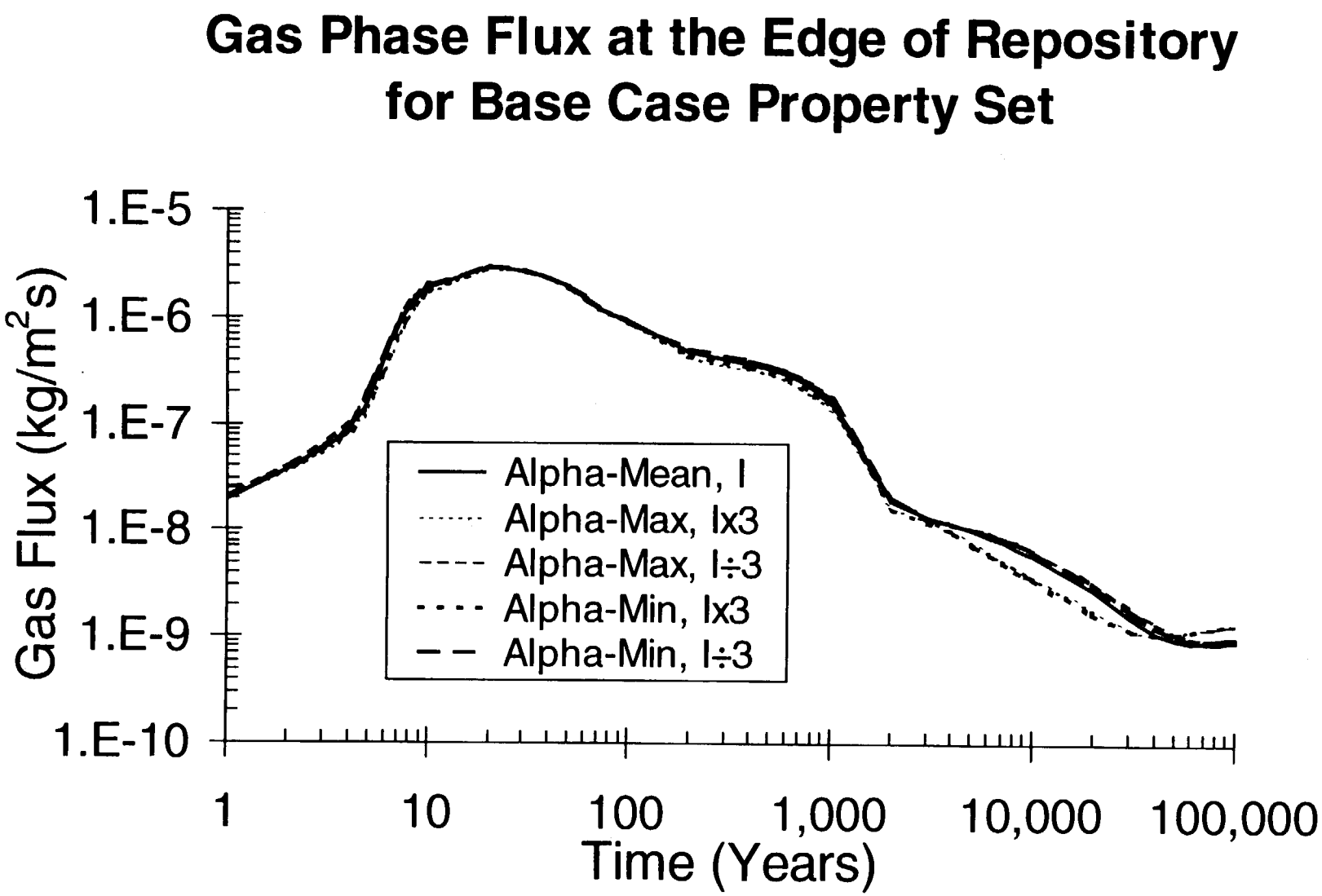

Figure 3-64. Gas flux at the edge of the repository for the base case property set at the present day infiltration rate.

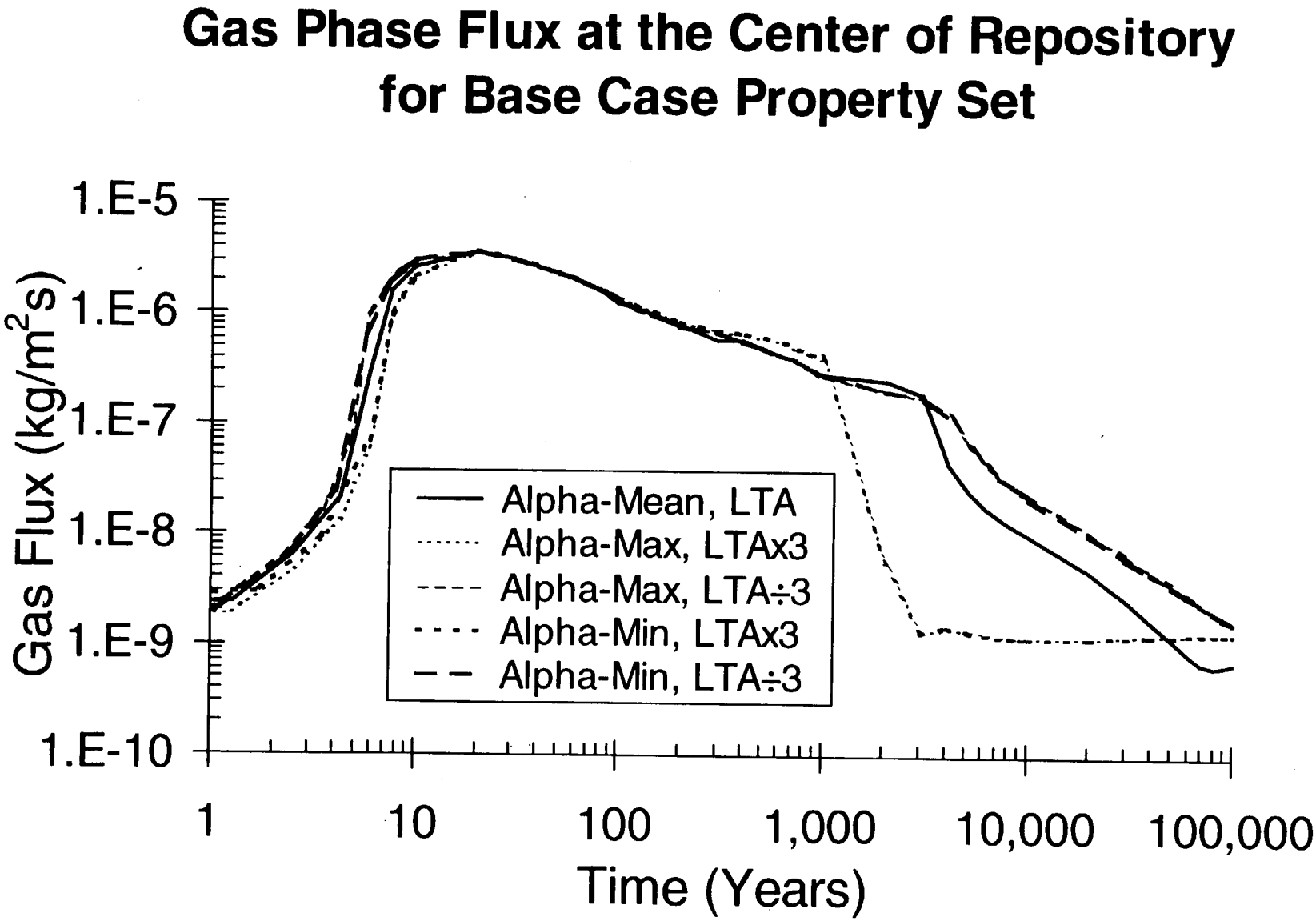

Figure 3-65. Gas flux at the center of the repository for the base case property set at the long term average infiltration rate.

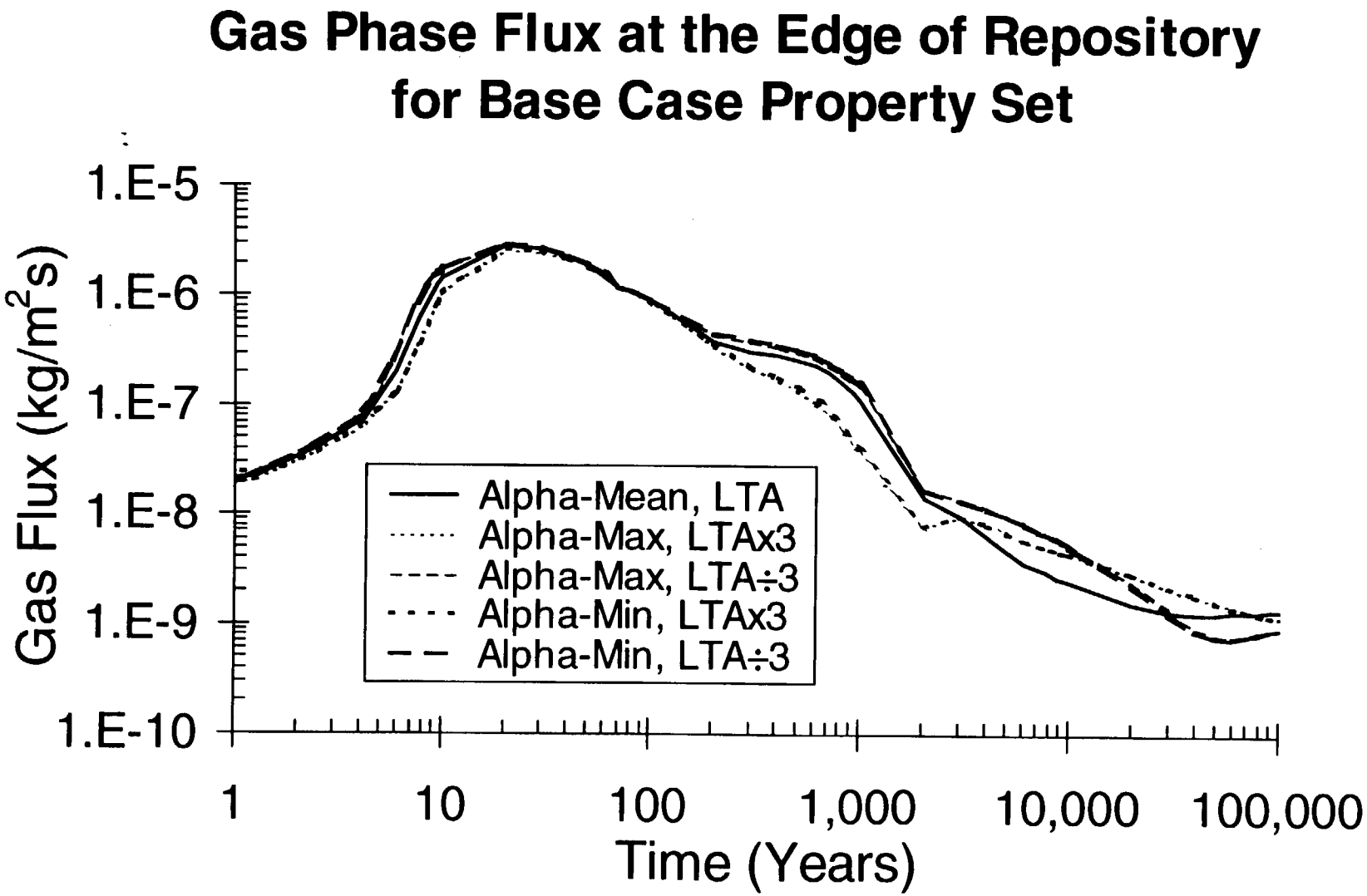

Figure 3-66. Gas flux at the edge of the repository for the base case property set at the long term average infiltration rate.

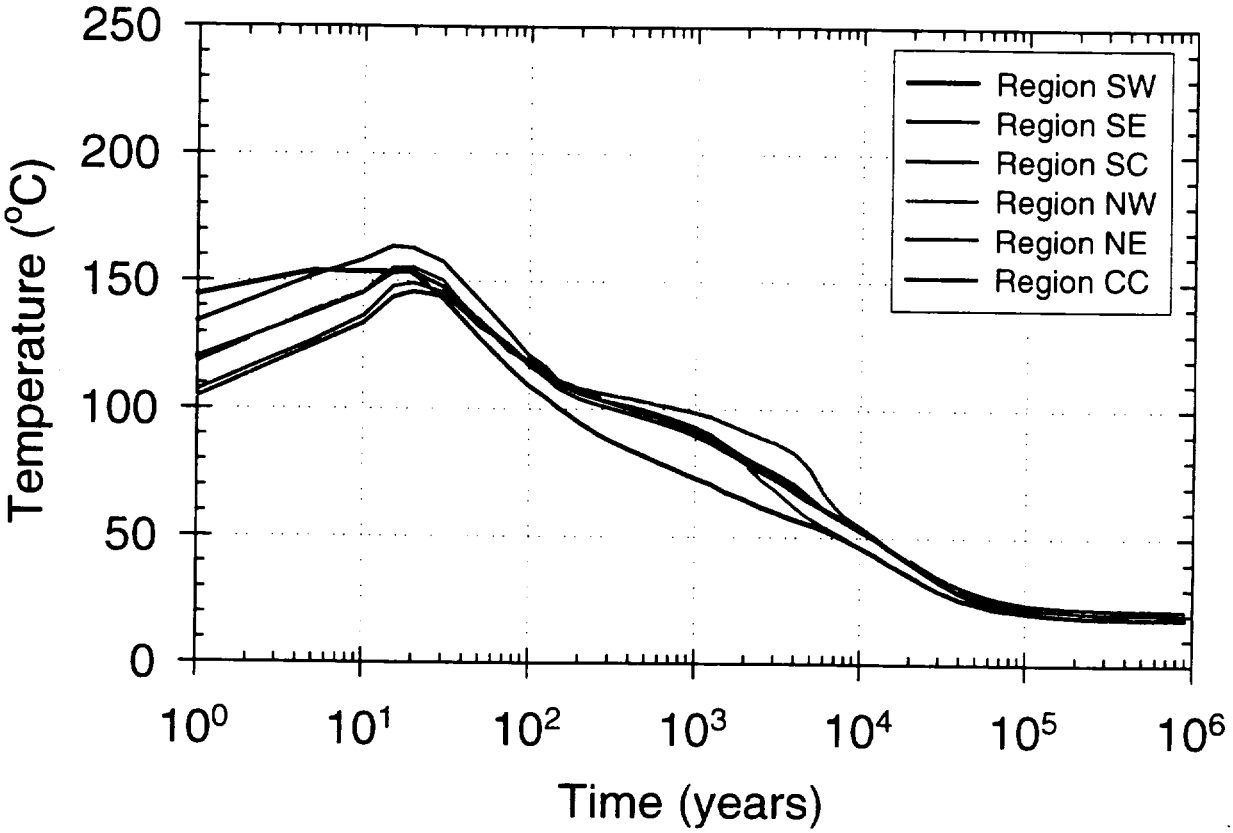

Figure 3-67. Average waste-package temperature history for six repository regions (commercial spent fuel, long-term-average climate, mean infiltration, base-case hydrologic properties)

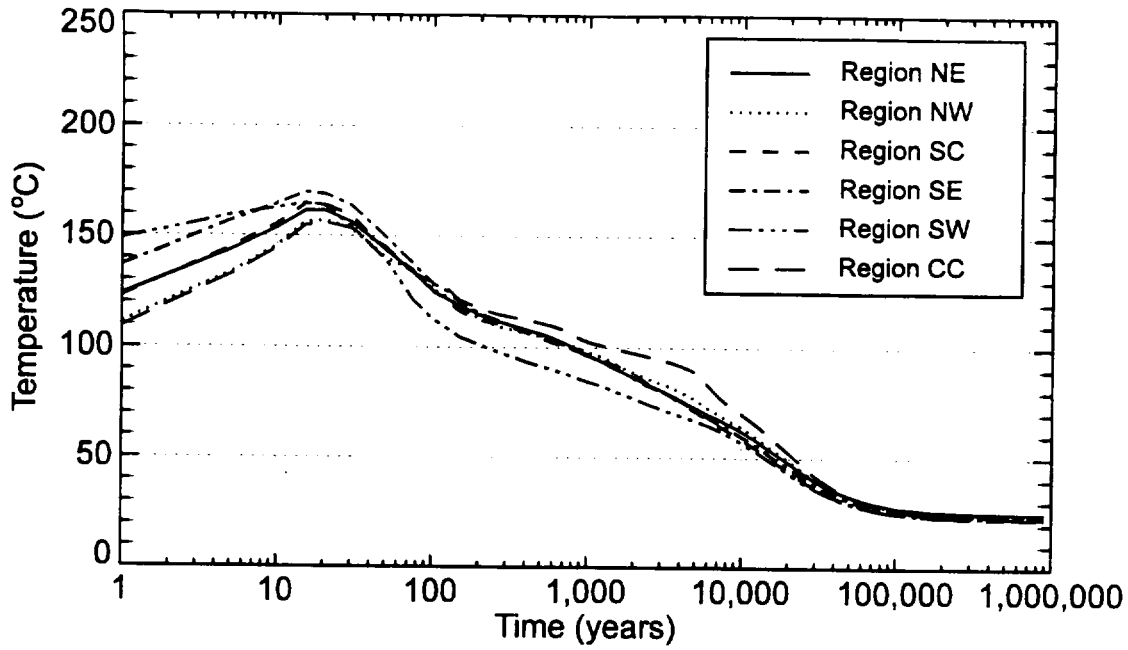

Figure 3-68. Average waste-package temperature history for six repository regions (commercial spent fuel, present day climate, mean infiltration, base-case hydrologic properties)

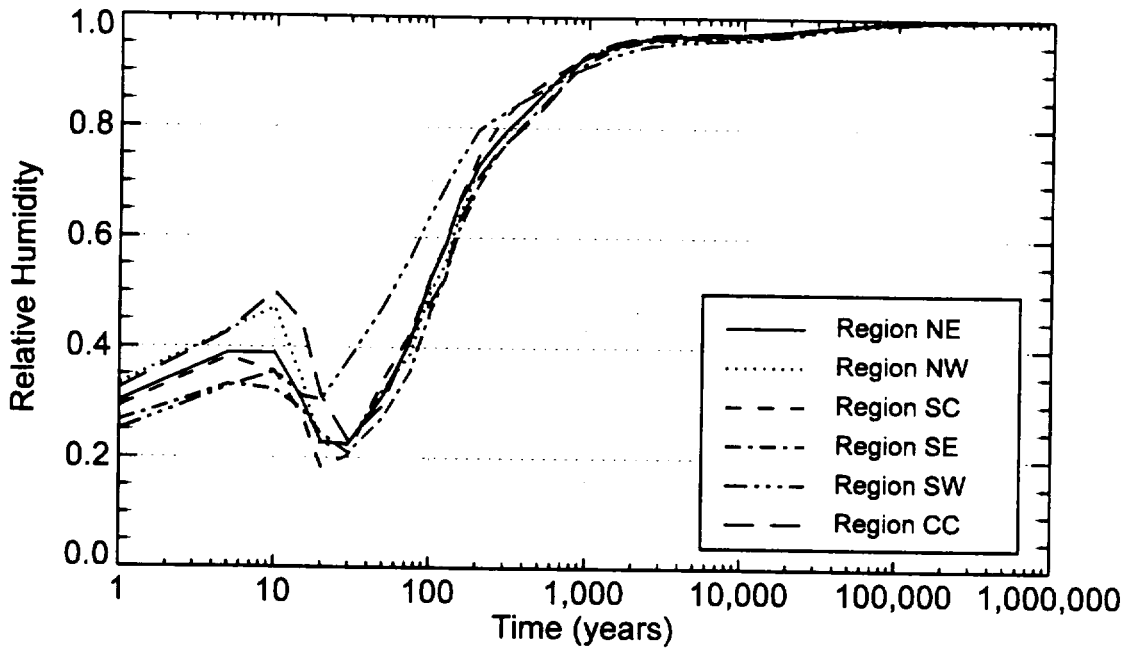

Figure 3-69. Average waste-package relative humidity history for six repository regions (commercial spent fuel, long-term-average climate, mean infiltration, base-case hydrologic properties)

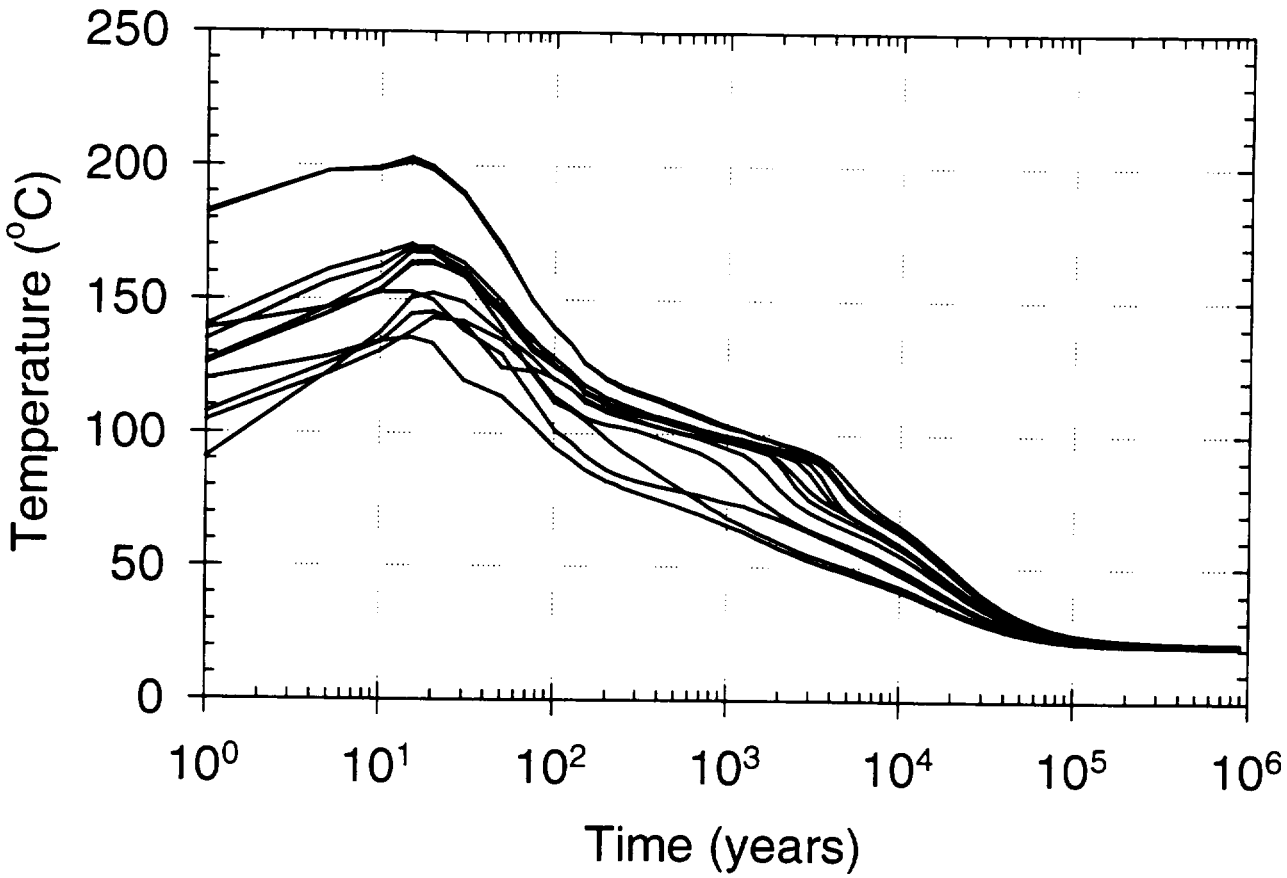

Figure 3-70. Variability of temperature history among waste packages (commercial spent fuel, long-term-average climate, mean infiltration, base-case hydrologic properties, region NE)

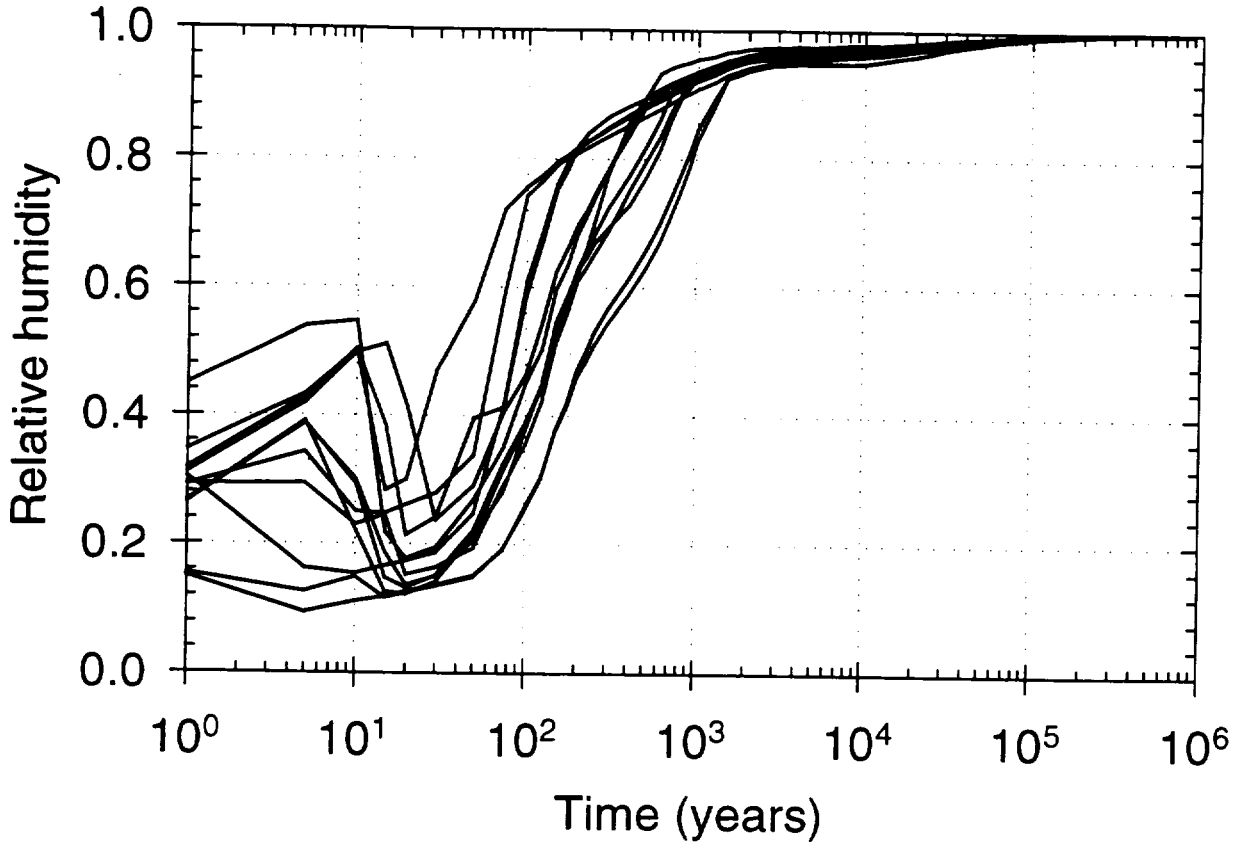

Figure 3-71. Variability of relative humidity history among waste packages (commercial spent fuel, long-term-average climate, mean infiltration, base-case hydrologic properties, region NE)

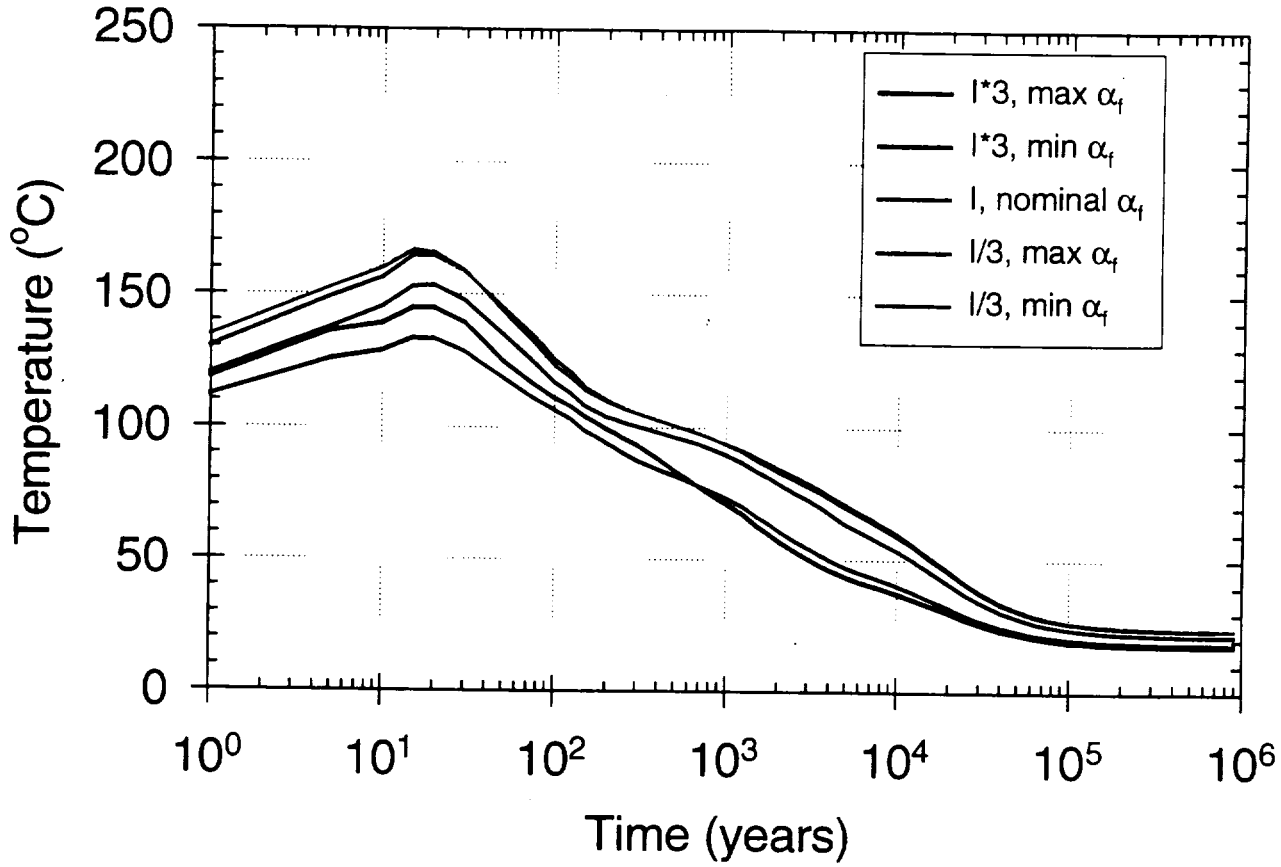

Figure 3-72. Average waste-package temperature history for the five base-case hydrologic-property sets (commercial spent fuel, long-term-average climate, region NE)

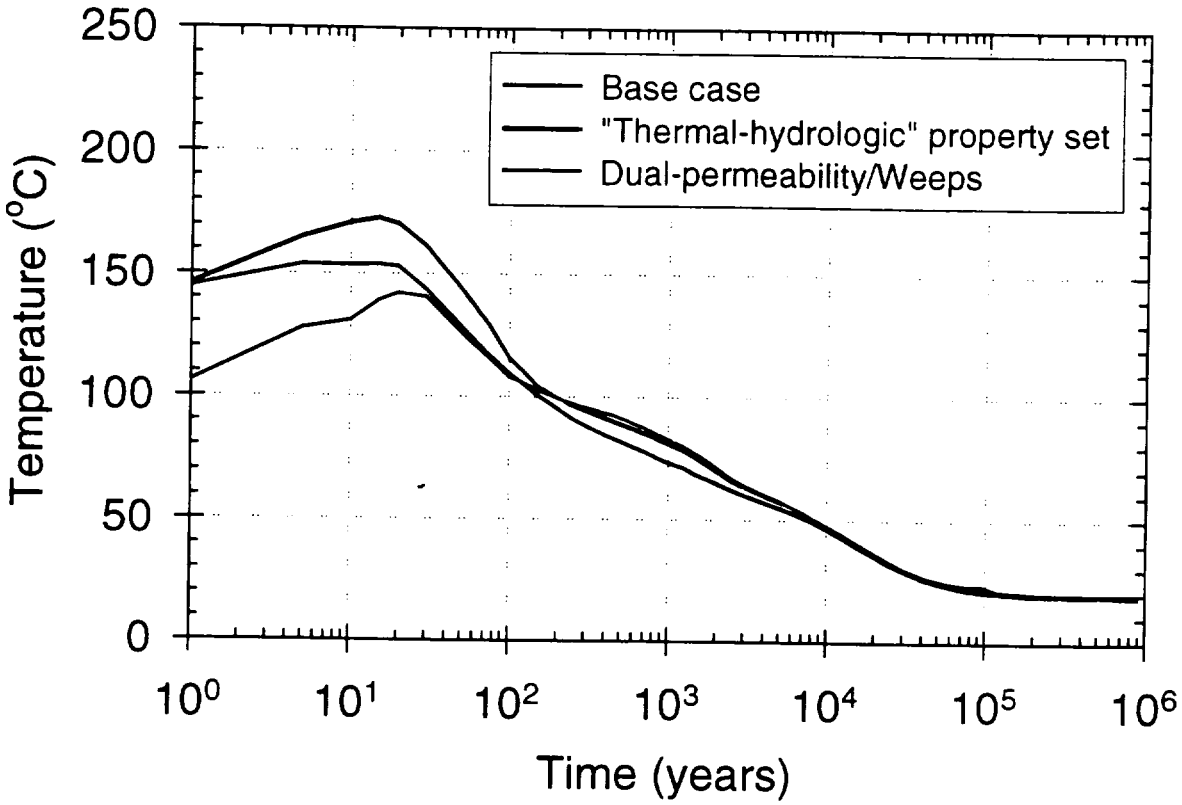

Figure 3-73. Effect of different hydrologic-property sets on waste-package temperature (commercial spent fuel, long-term-average climate, mean infiltration, region SW)

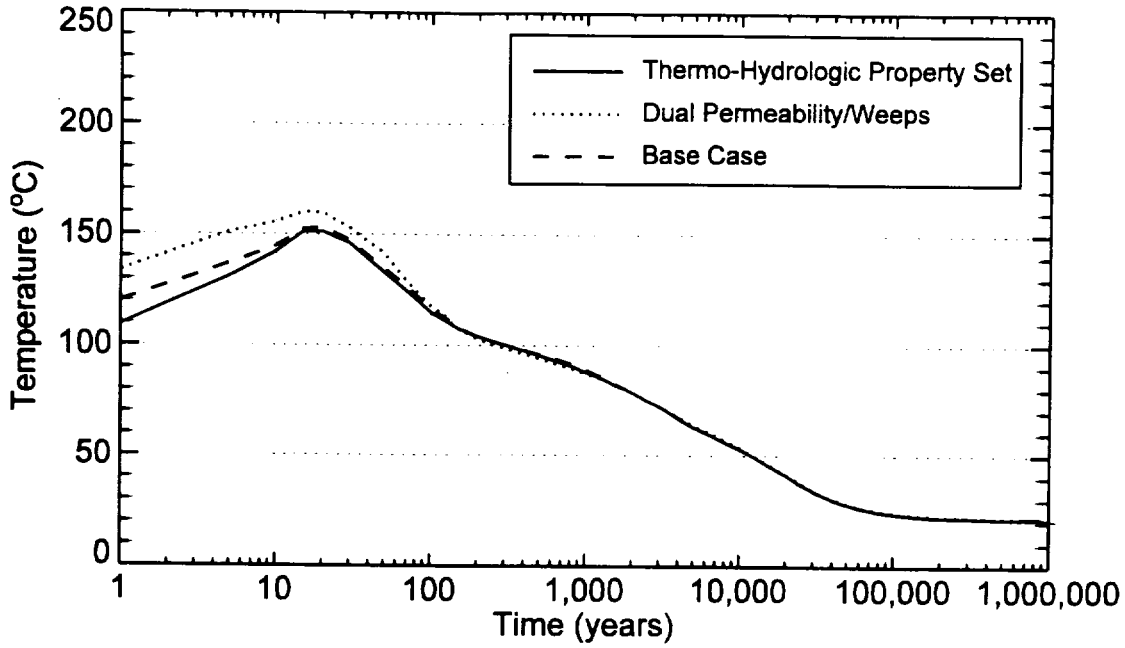

Figure 3-74. Effect of different hydrologic-property sets on waste-package temperature (commercial spent fuel, long-term-average climate, mean infiltration, region NE)

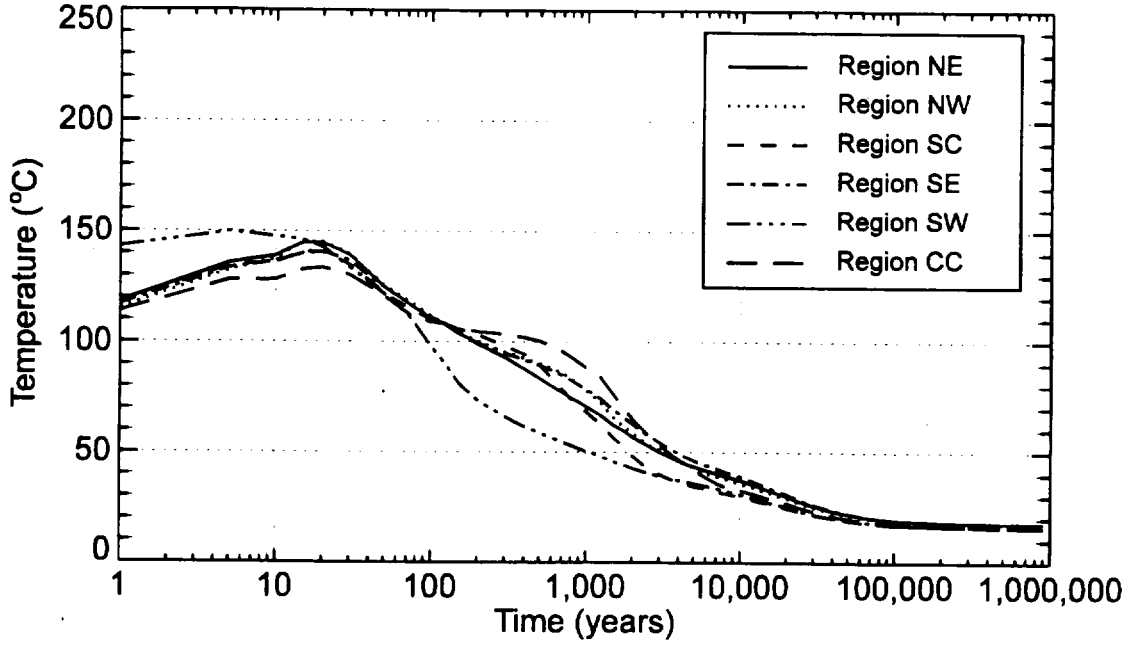

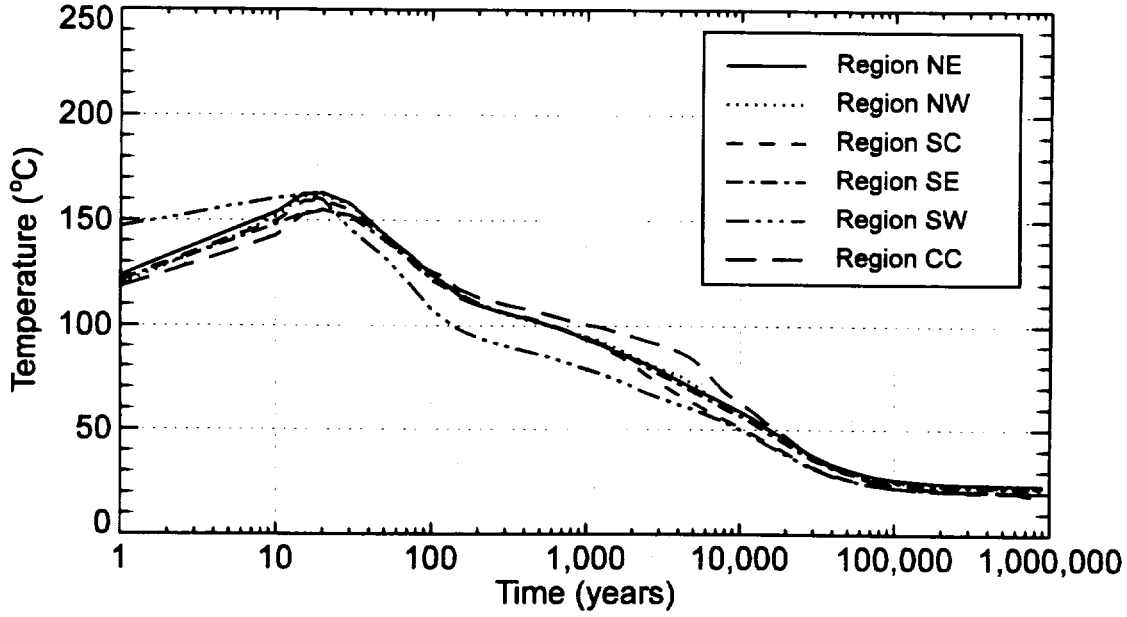

Figure 3-75. Average waste-package temperature history for six repository regions (commercial spent fuel, long-term-average climate, maximum α_l, I*3 infiltration rate, base-case hydrologic properties)

Figure 3-76. Average waste-package temperature history for six repository regions (commercial spent fuel, present day climate, maximum α_l, I*3 infiltration rate, base-case hydrologic properties)

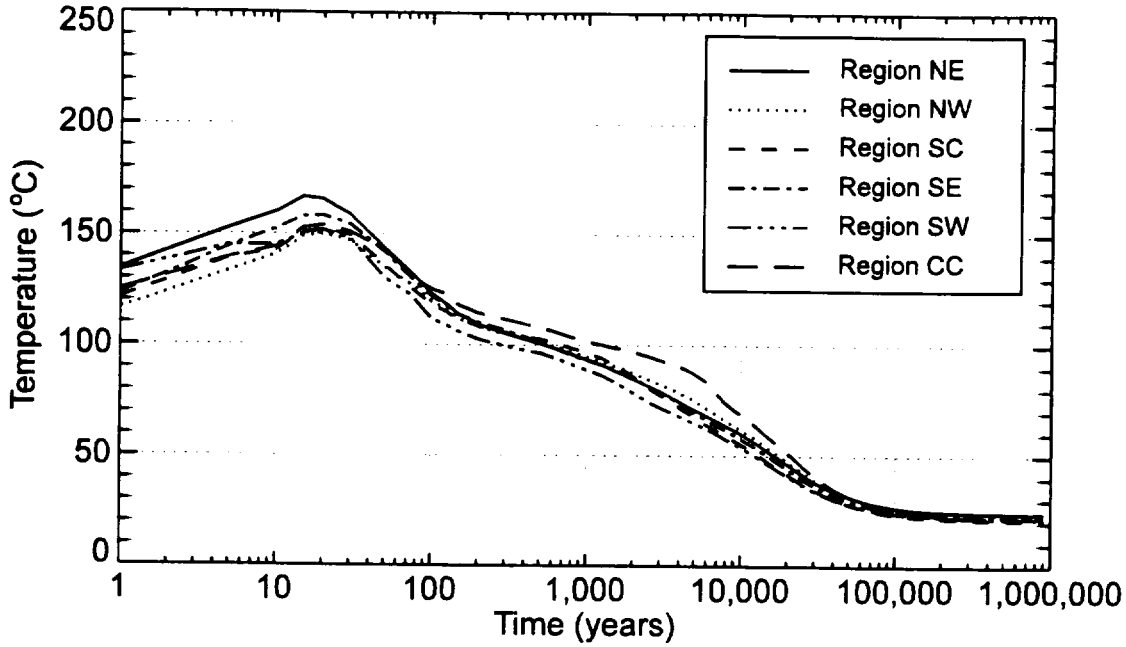

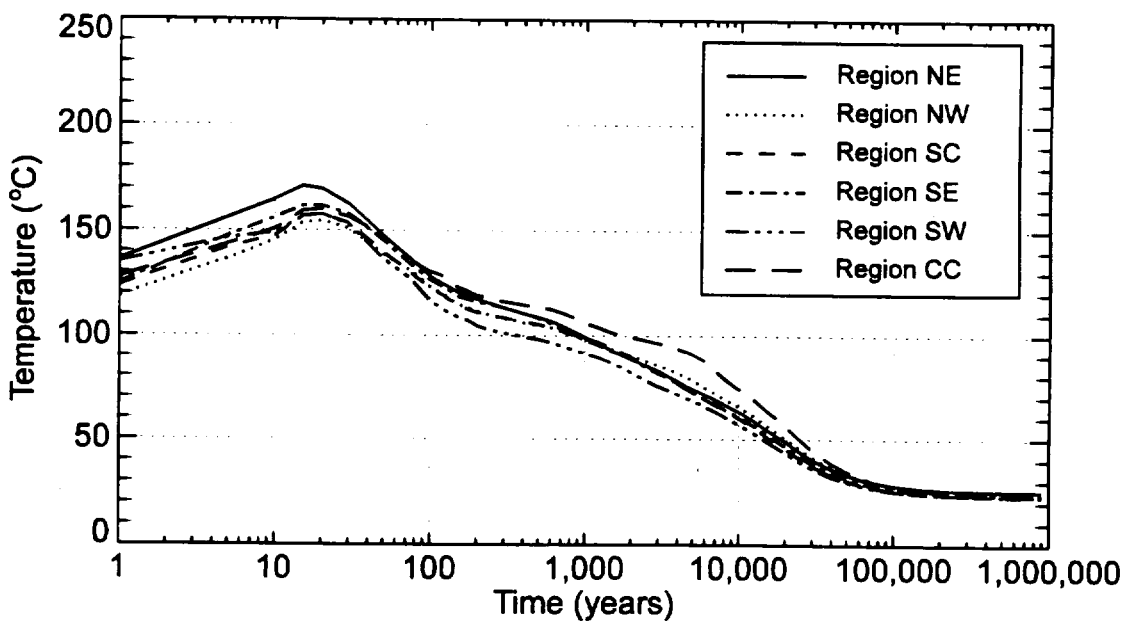

Figure 3-77. Average waste-package temperature history for six repository regions (commercial spent fuel, long-term-average climate, minimum α_l, I/3 infiltration rate, base-case hydrologic properties)

Figure 3-78. Average waste-package temperature history for six repository regions (commercial spent fuel, present day climate, minimum α_l, I/3 infiltration rate, base-case hydrologic properties)

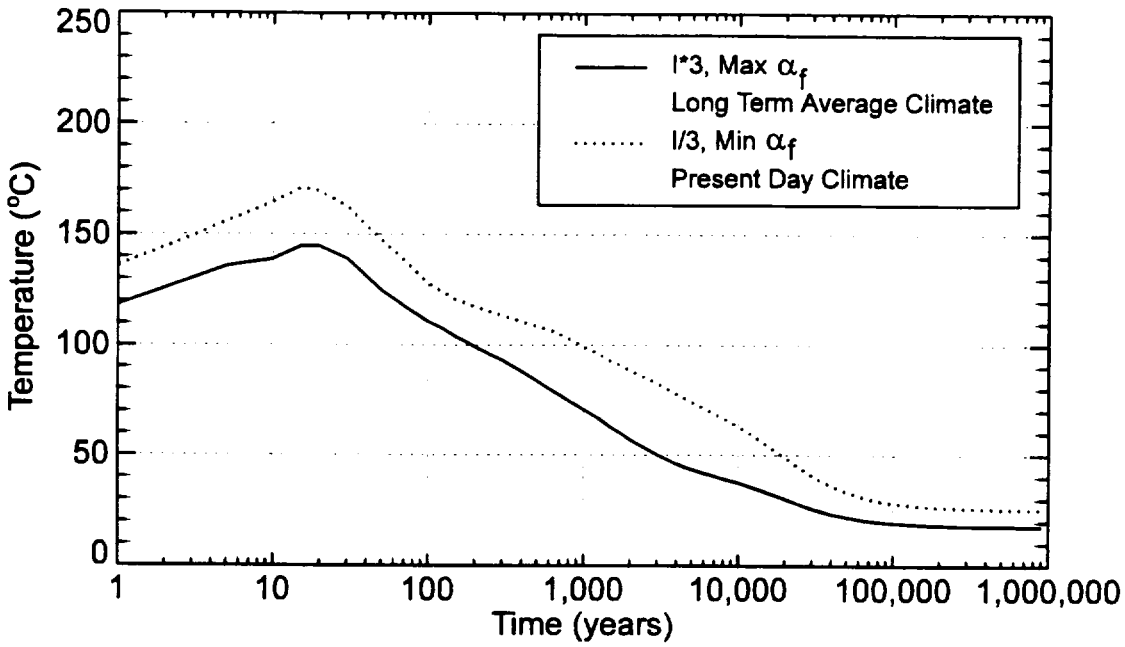

Figure 3-79. Maximum waste package temperature variability including climate change (commercial spent fuel, base case hydrologic properties, region NE)

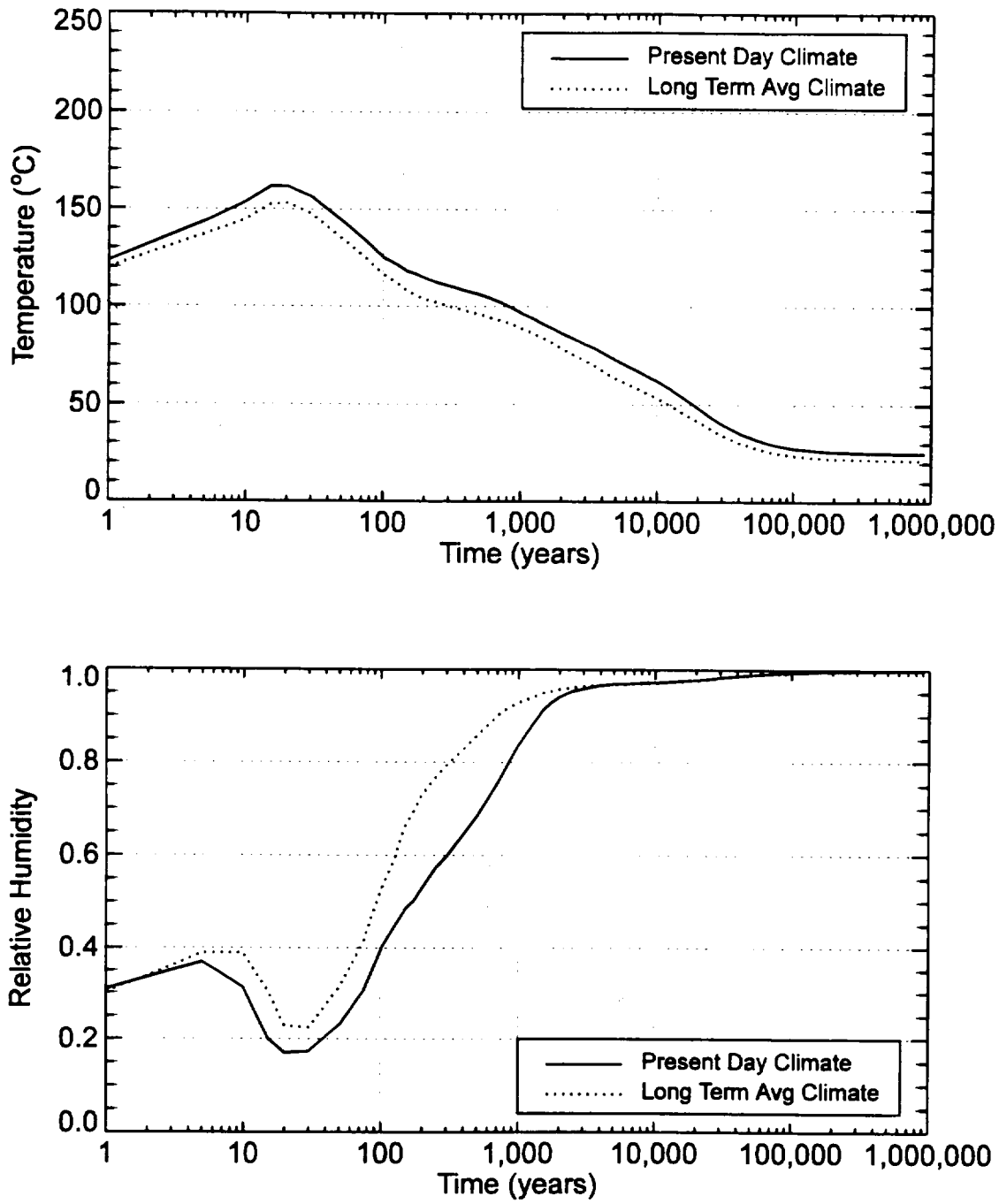

Figure 3-80. Waste package temperature variability including only the climate change response (commercial spent fuel, mean infiltration, base case hydrologic properties, region NE)

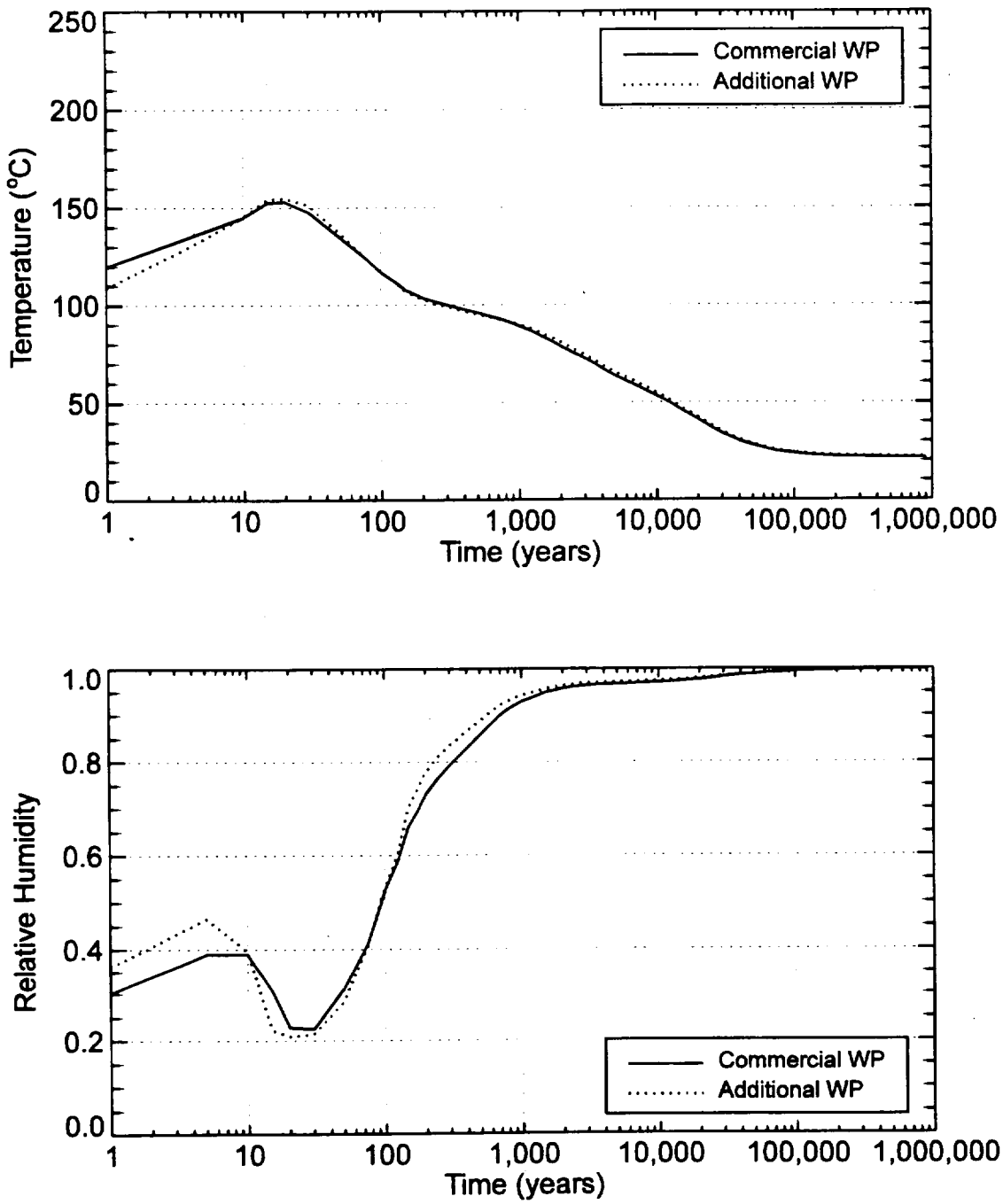

Figure 3-81. Comparison of commercial wastes to additional wastes for a point-load repository design (long-term-average climate, mean infiltration, base case hydrologic property set, region NE). Upper figure: average waste package temperature, Lower figure: average waste package relative humidities

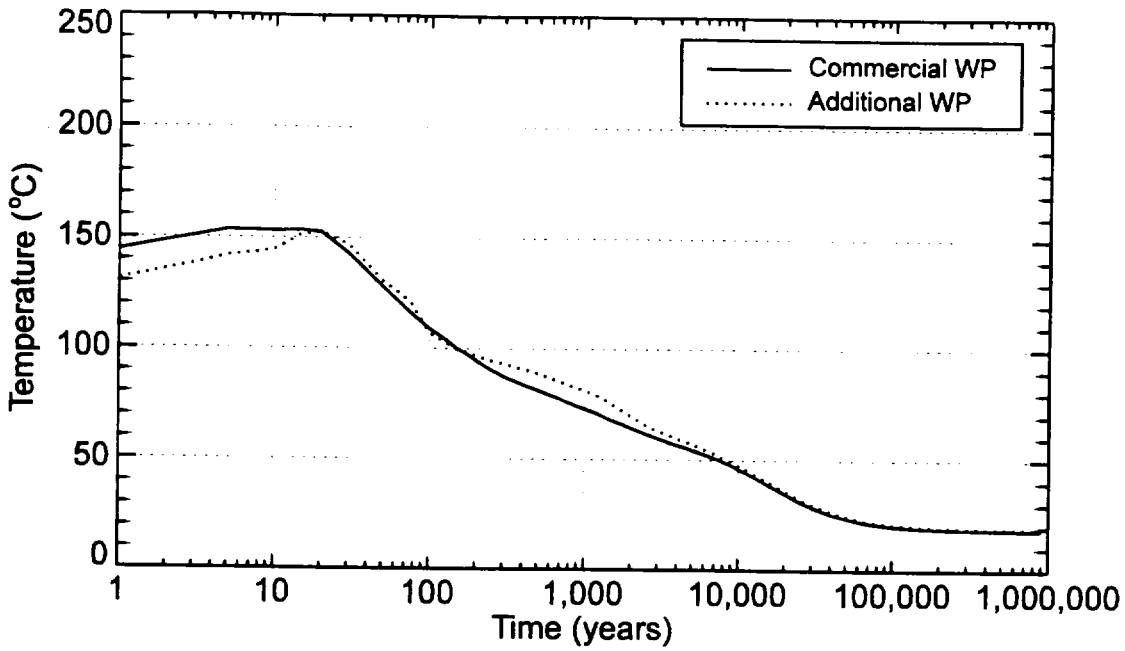

Figure 3-82. Comparison of commercial wastes to additional wastes for a point-load repository design (long-term-average climate, mean infiltration, base case hydrologic property set, region SW)

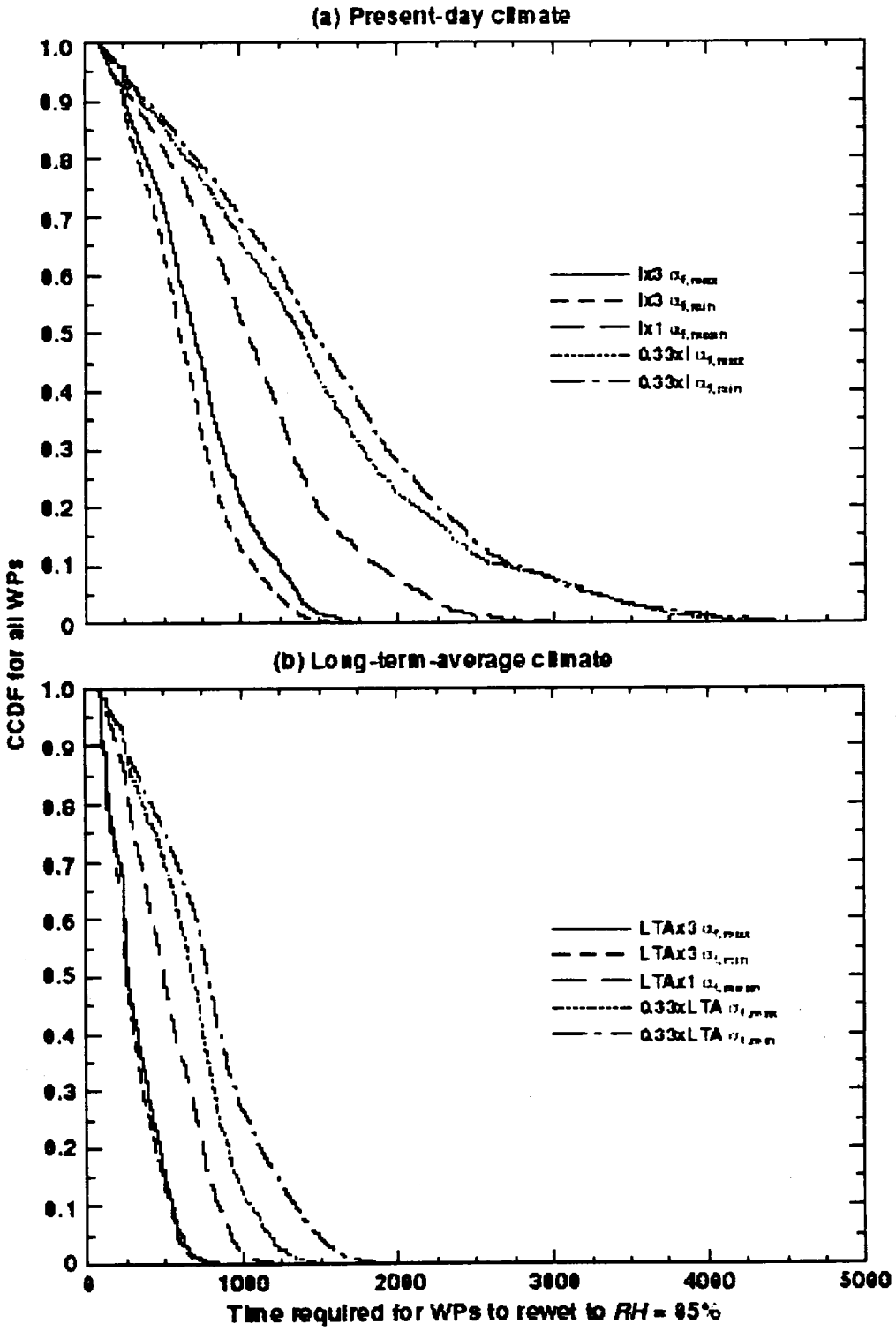

Figure 3-83. Complementary cumulative density function (CCDF) of the time required for waste packages to rewet to a relative humidity of 85% for the point-load design with no backfill for (a) present-day-climate percolation flux and (b) long-term-average-climate percolation flux. Going from left to right, curves are plotted for five cases in (a): (1) Ix3 $\alpha_{f,max}$, (2) Ix3, $\alpha_{f,min}$, (3) Ix1 $\alpha_{f,mean}$, (4) 0.33xI $\alpha_{f,max}$, and (5) 0.33xI $\alpha_{f,min}$, and for five cases in (b): (1) LTAx3 $\alpha_{f,max}$, (2) LTAx3 $\alpha_{f,min}$, (3) LTAx1 $\alpha_{f,mean}$, (4) 0.33xLTA $\alpha_{f,max}$, and (5) 0.33xLTA, $\alpha_{f,min}$, where α_f is the Van Genuchten "alpha" parameter for fractures. The subscripts min, mean, and max stand for the minimum, mean, and maximum values of α_f, the symbol I stands for the present-day-climate percolation-flux map, and the symbol LTA stands for the long-term-average percolation-flux map.

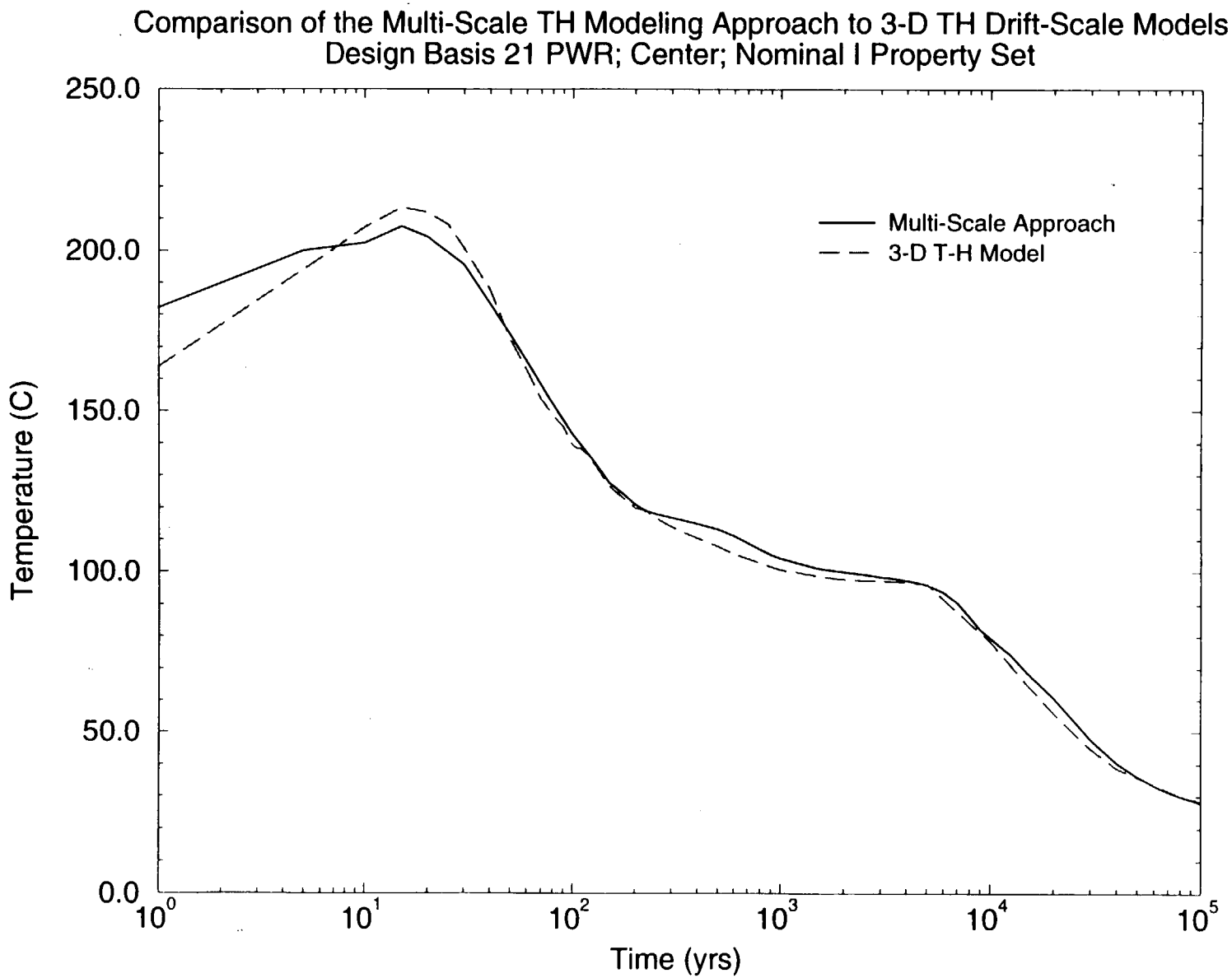

Figure 3-84. Comparison of the TH multiscale modeling and abstraction method to the PA testing models, design basis 21 PWR waste package temperature, repository center, present day infiltration rate.

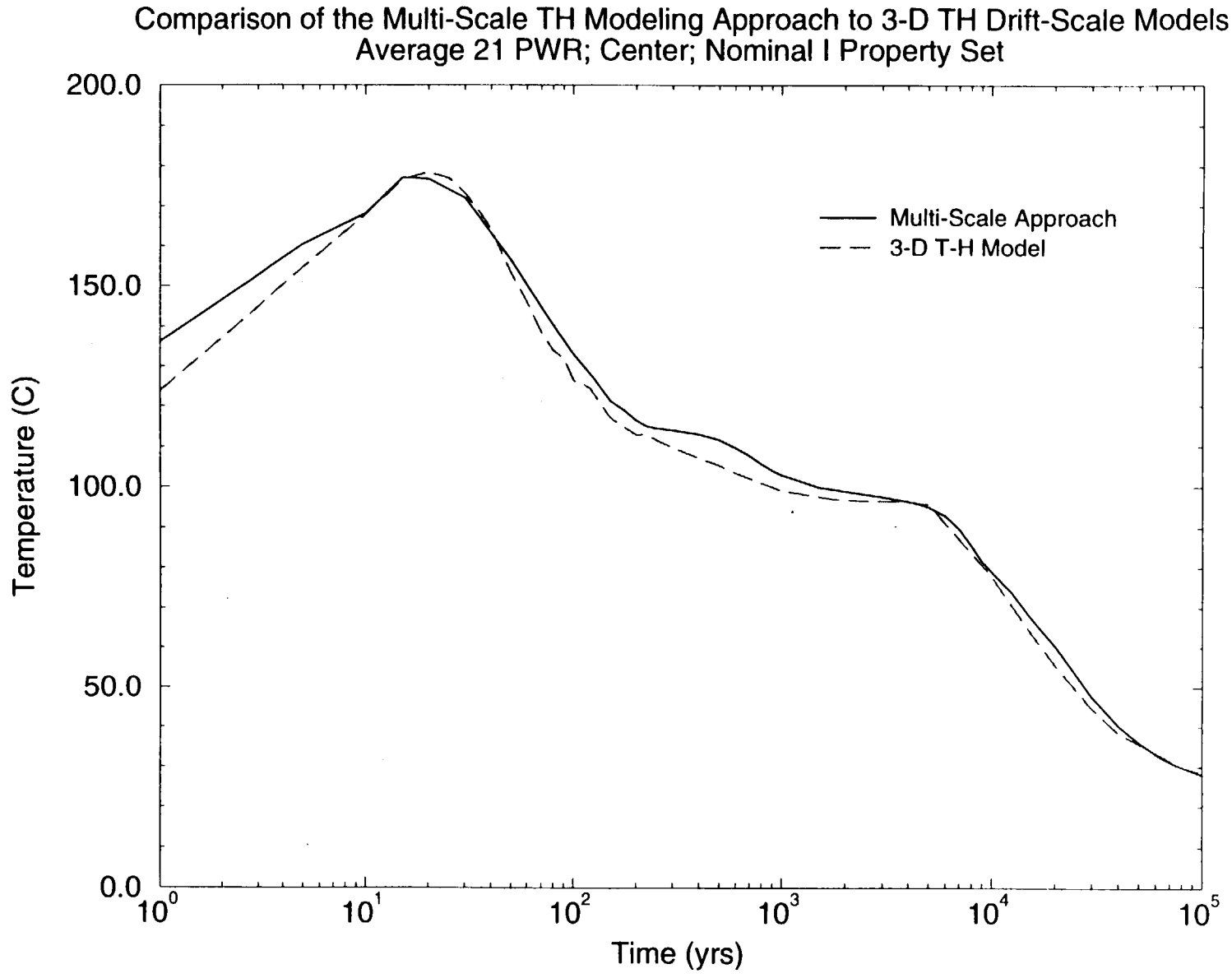

Figure 3-85. Comparison of the TH multiscale modeling and abstraction method to the PA testing models, average 21 PWR waste package temperature, repository center, present day infiltration rate.

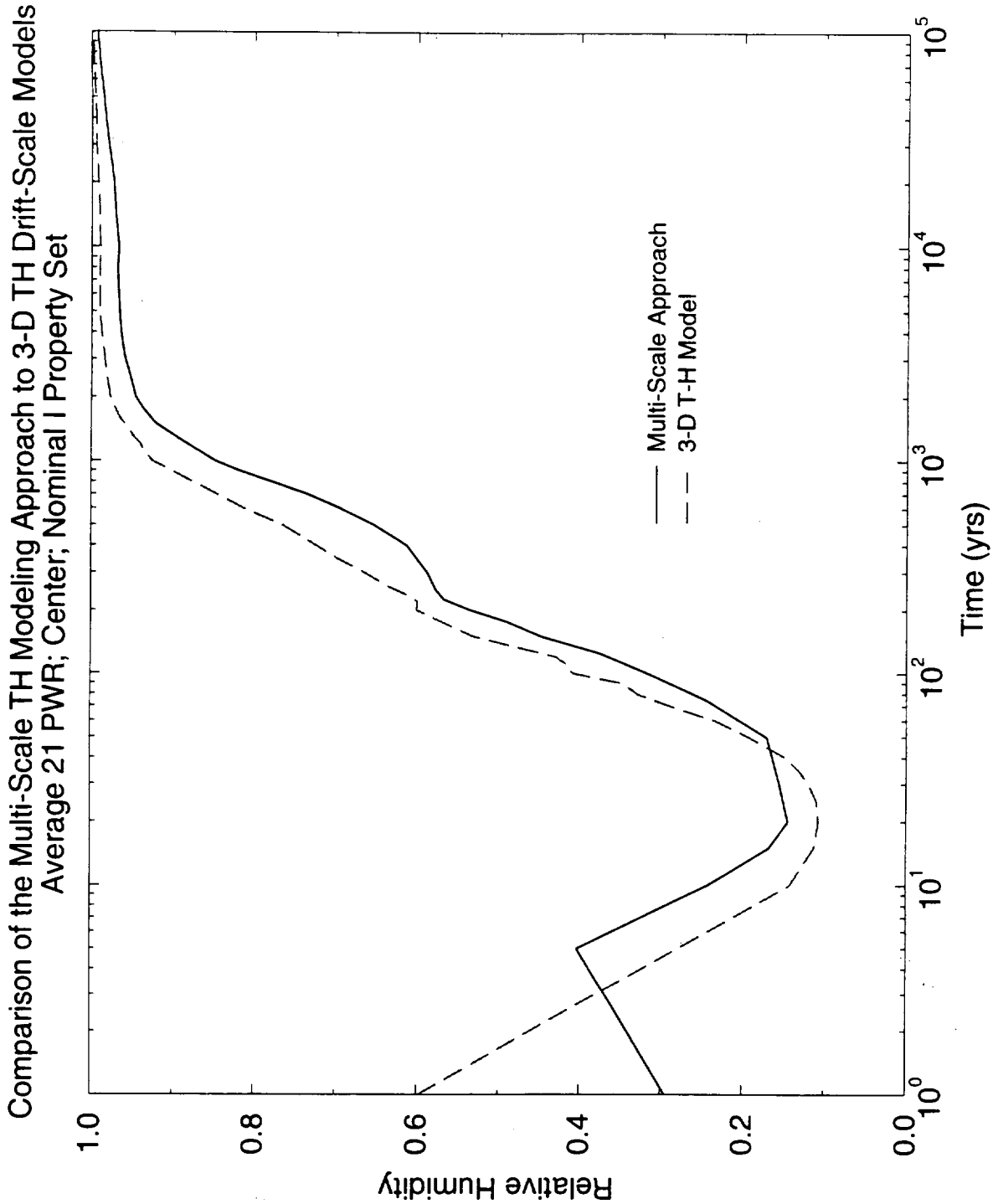

Figure 3-86. Comparison of the TH multiscale modeling and abstraction method to the PA testing models, average 21 PWR waste package relative humidity, repository center, present day infiltration rate.

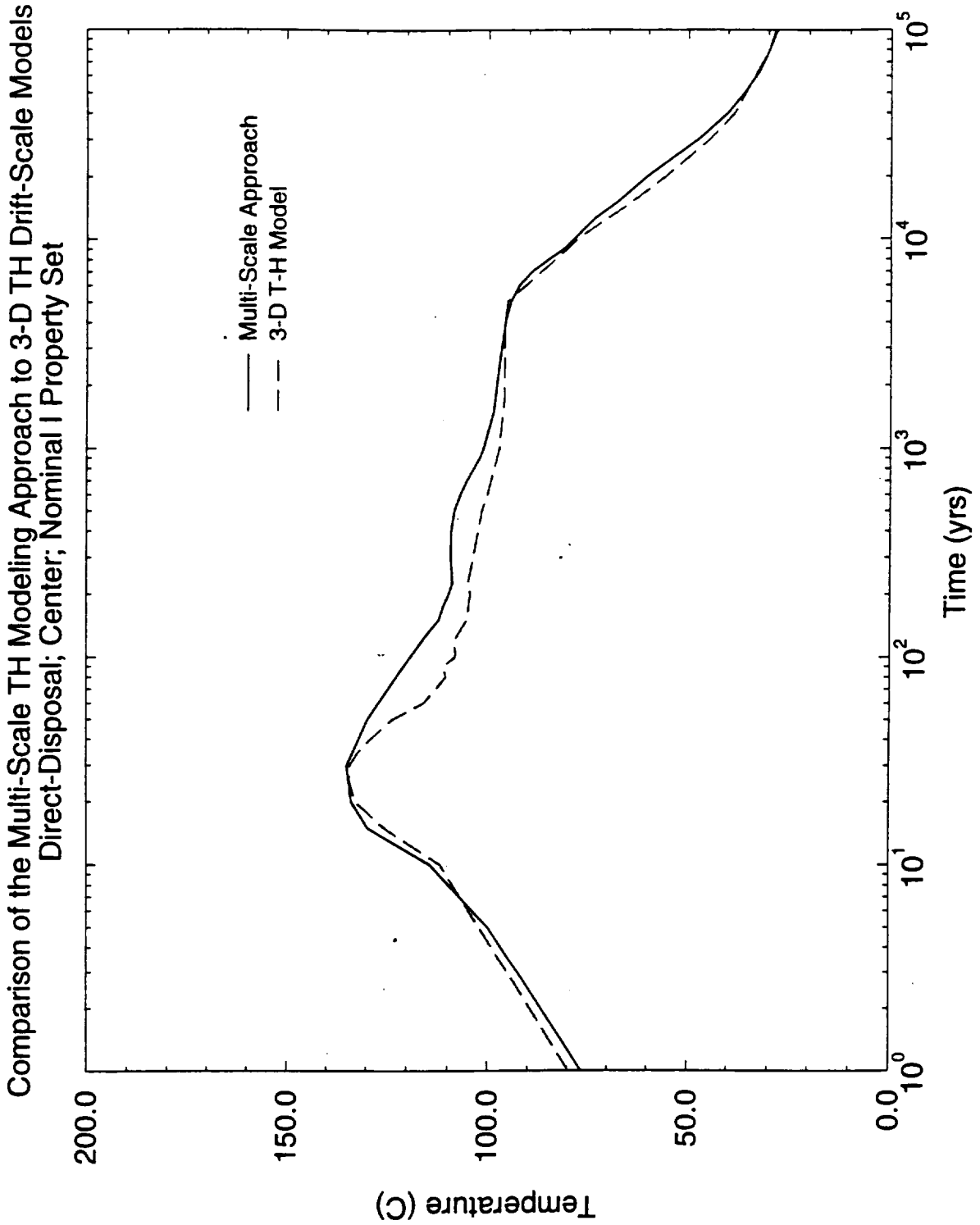

Figure 3-87. Comparison of the TH multiscale modeling and abstraction method to the PA testing models, separate disposal (or direct-disposal) waste package temperature, repository center, present day infiltration rate.

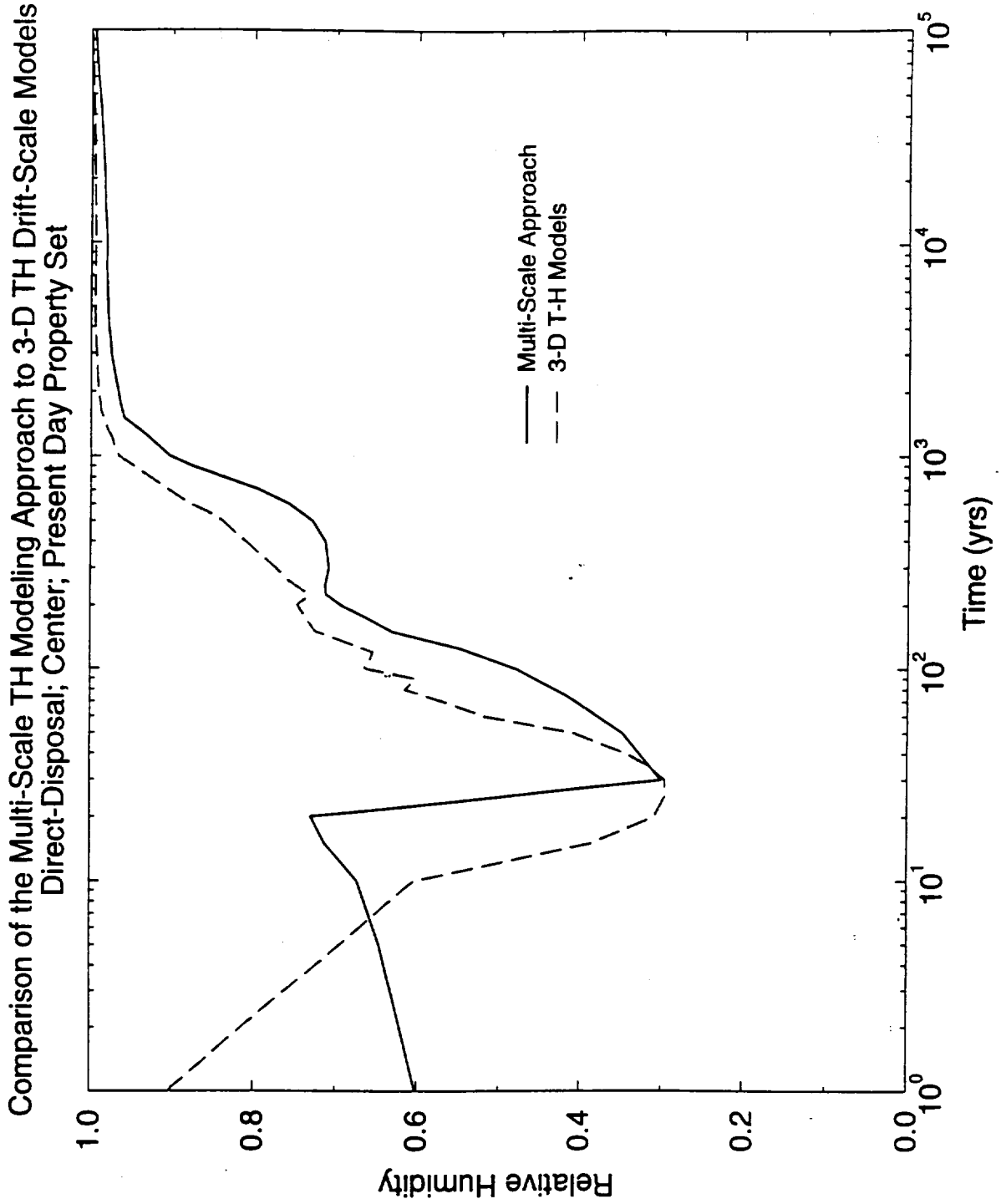

Figure 3-88. Comparison of the TH multiscale modeling and abstraction method to the PA testing models, separate disposal (or direct-disposal) waste package relative humidity, repository center, present day infiltration rate.

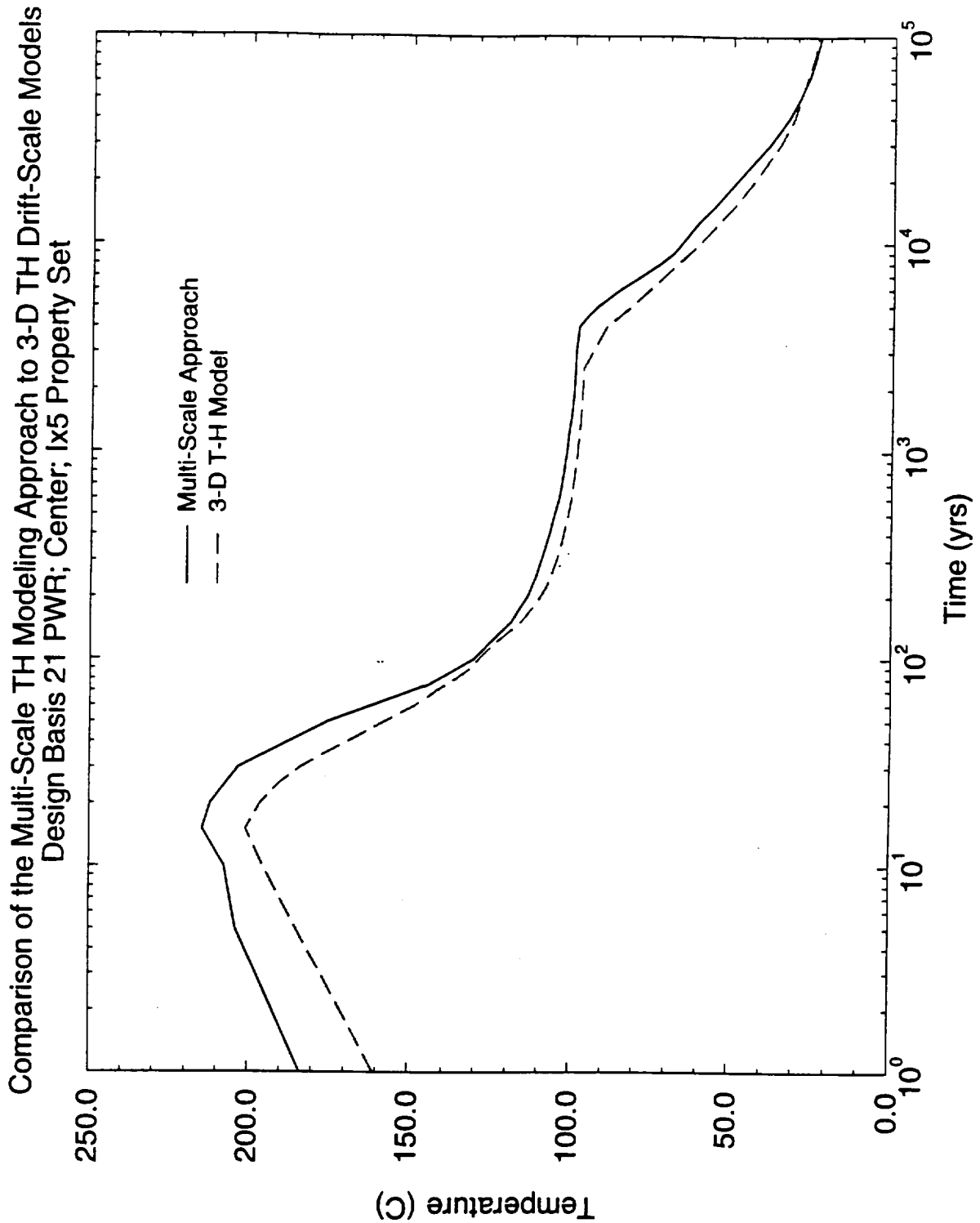

Figure 3-89. Comparison of the TH multiscale modeling and abstraction method to the PA testing models, design basis 21 PWR waste package temperature, repository center, present day I*5 infiltration rate.

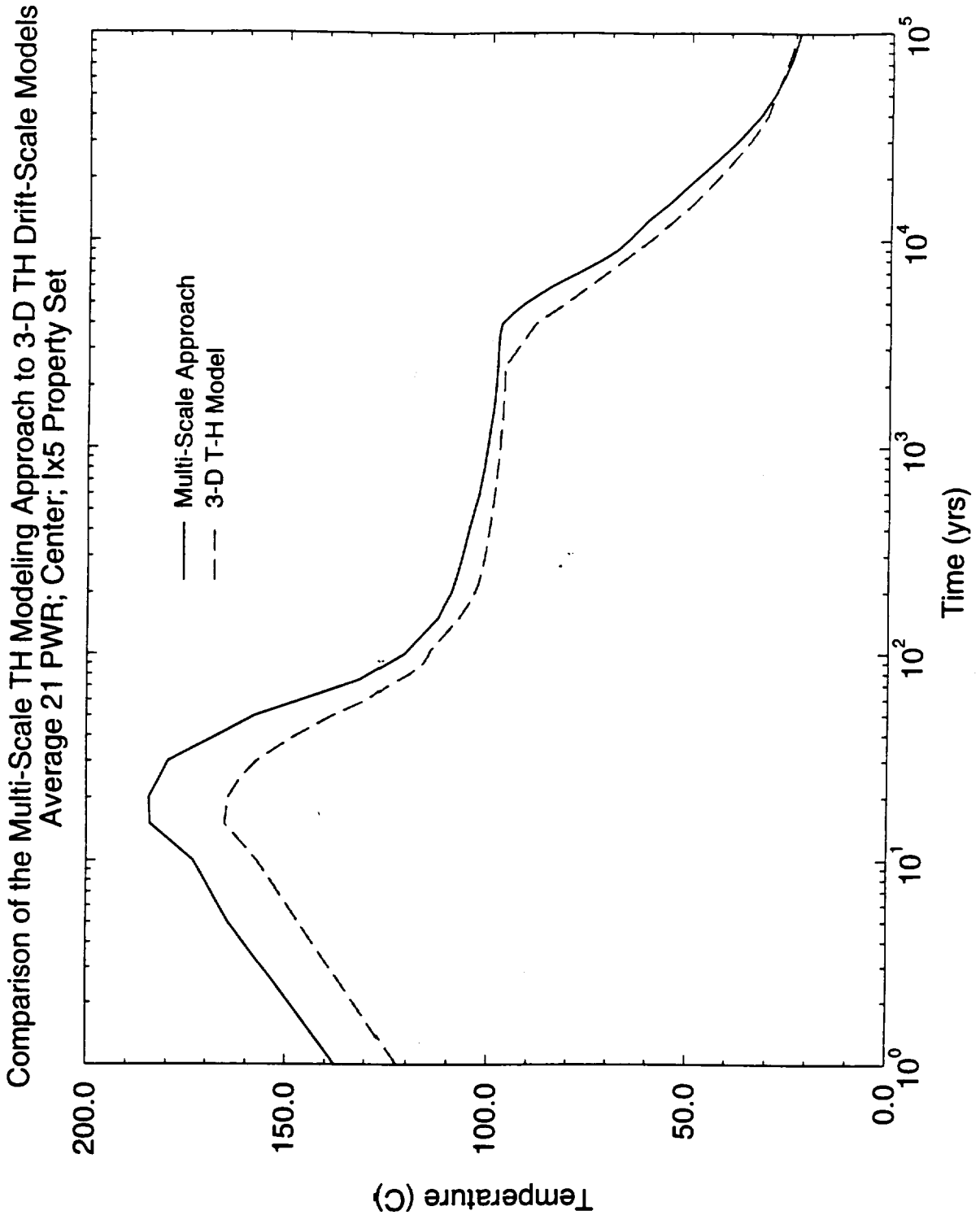

Figure 3-90. Comparison of the TH multiscale modeling and abstraction method to the PA testing models, average 21 PWR waste package temperature, repository center, present day I*5 infiltration rate.

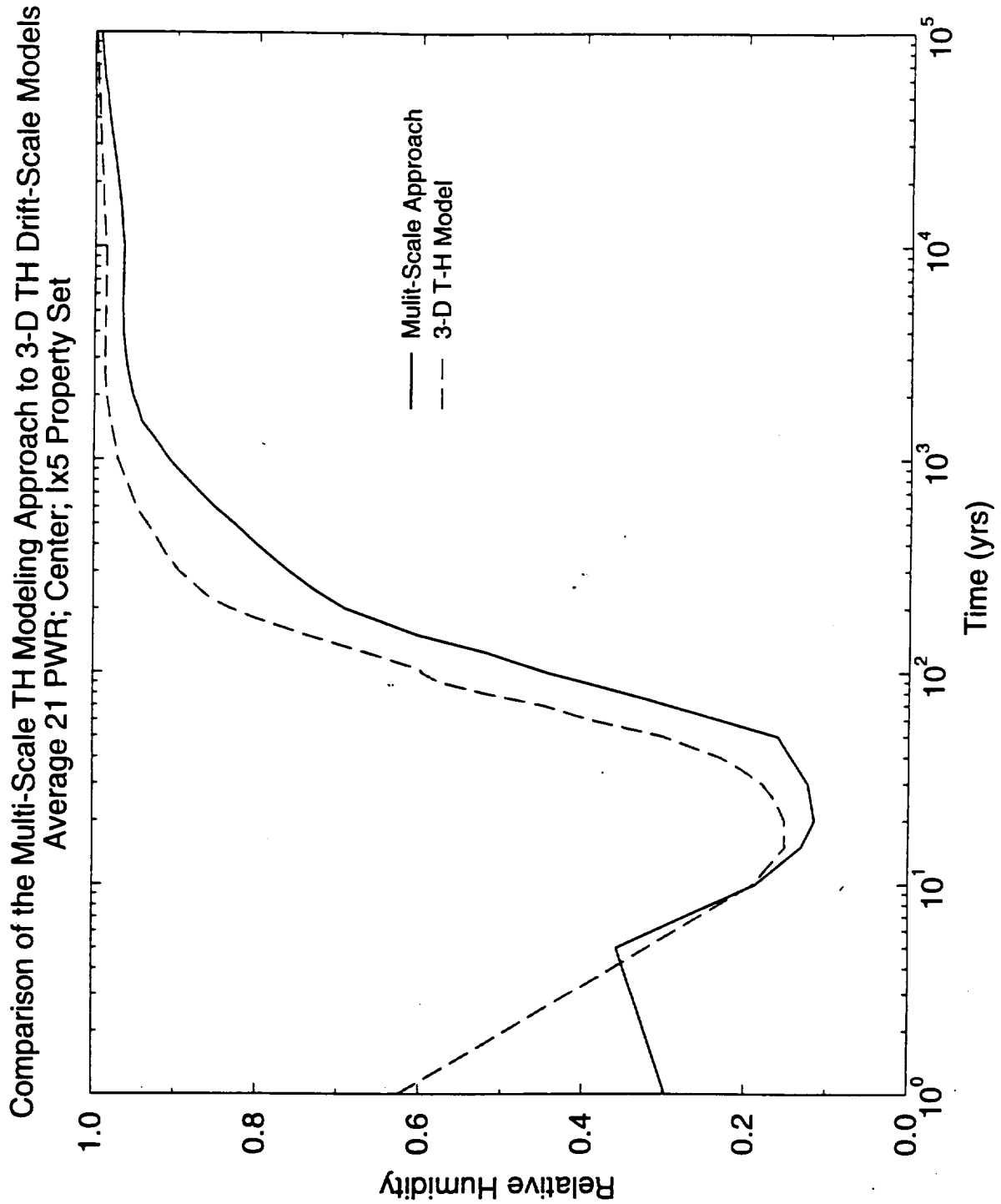

Figure 3-91. Comparison of the TH multiscale modeling and abstraction method to the PA testing models, average 21 PWR waste package relative humidity, repository center, present day I*5 infiltration rate.

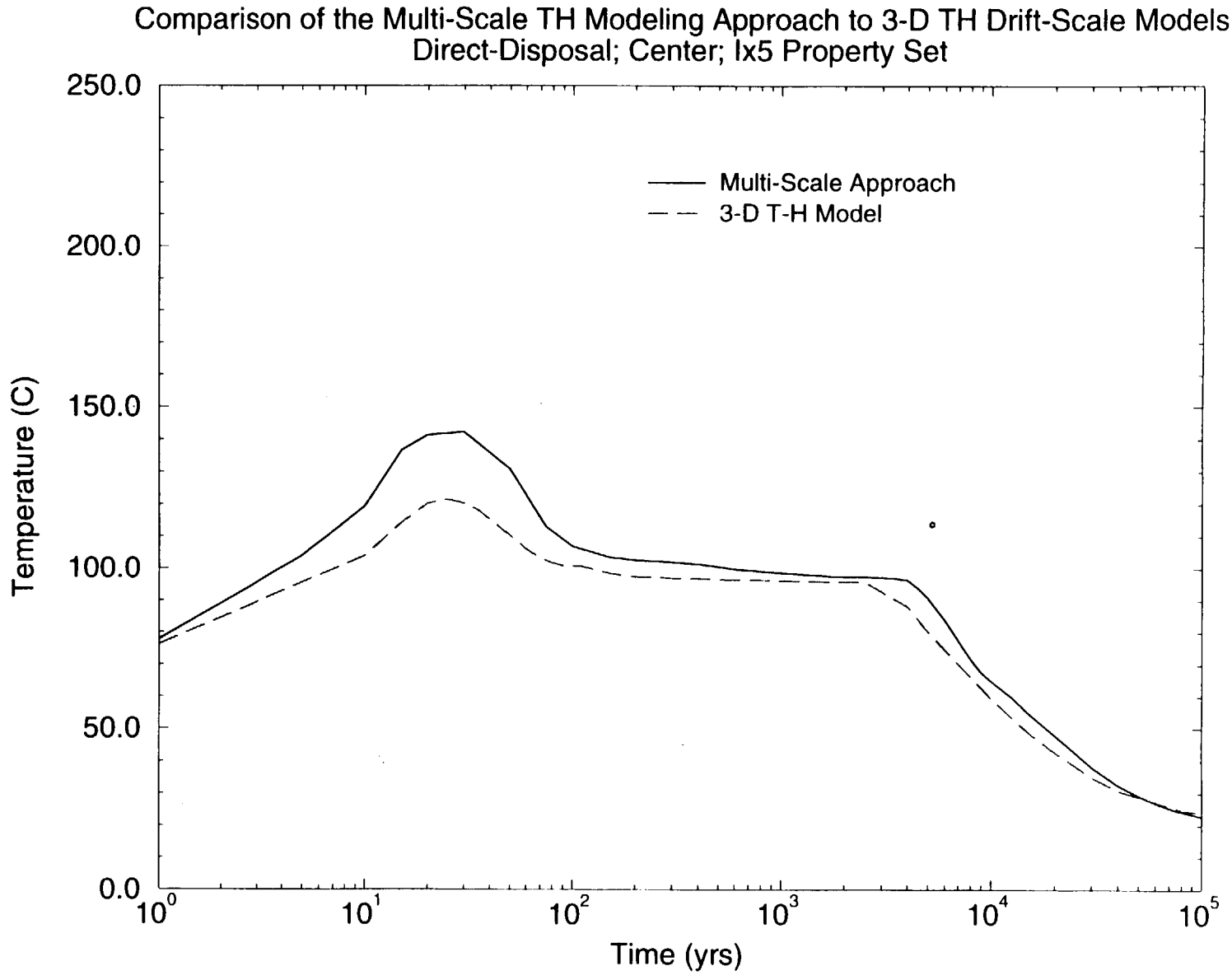

Figure 3-92. Comparison of the TH multiscale modeling and abstraction method to the PA testing models, separate disposal (or direct-disposal) waste package temperature, repository center, present day I*5 infiltration rate.

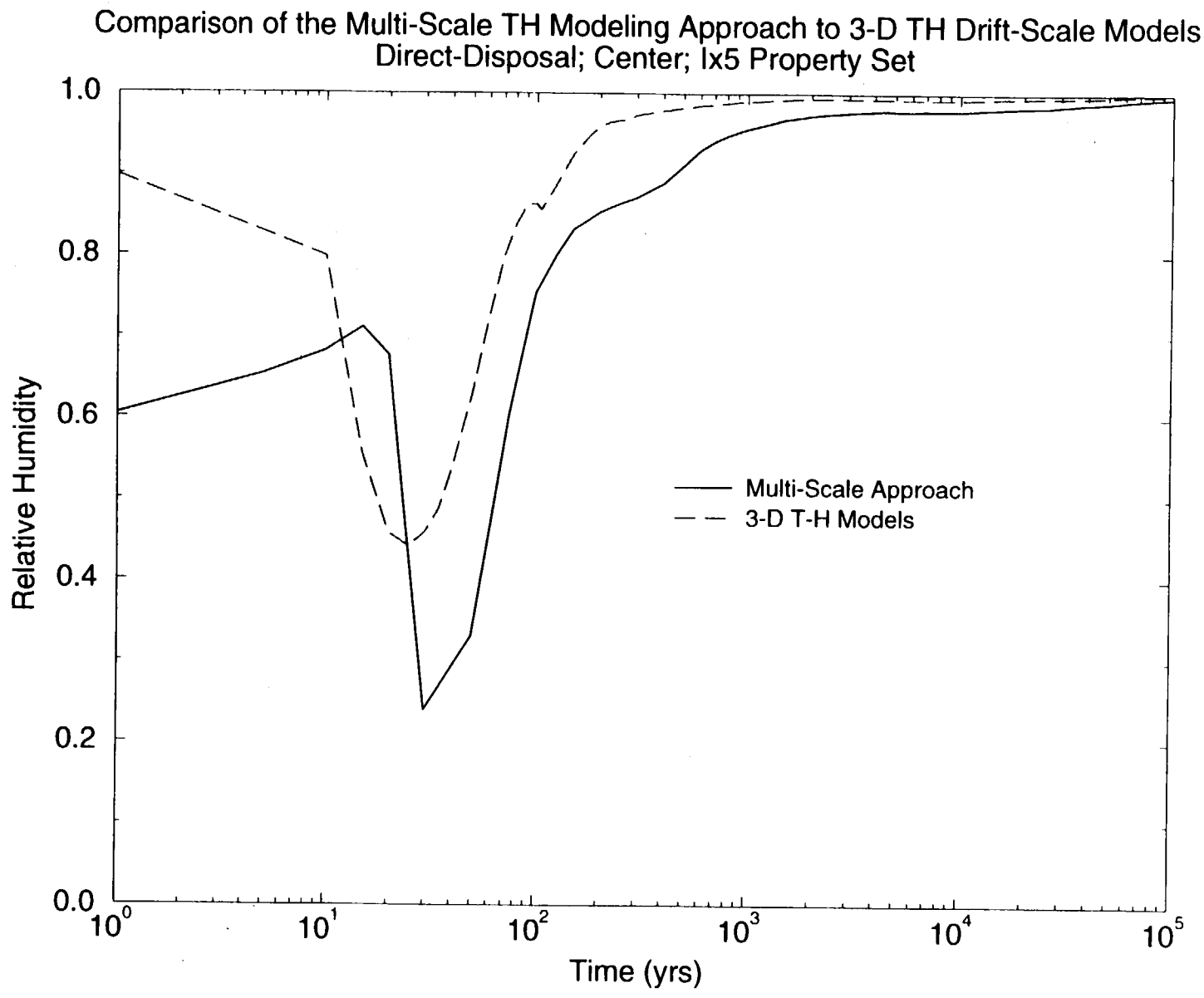

Figure 3-93. Comparison of the TH multiscale modeling and abstraction method to the PA testing models, separate disposal (or direct-disposal) waste package relative humidity, repository center, present day I*5 infiltration rate.

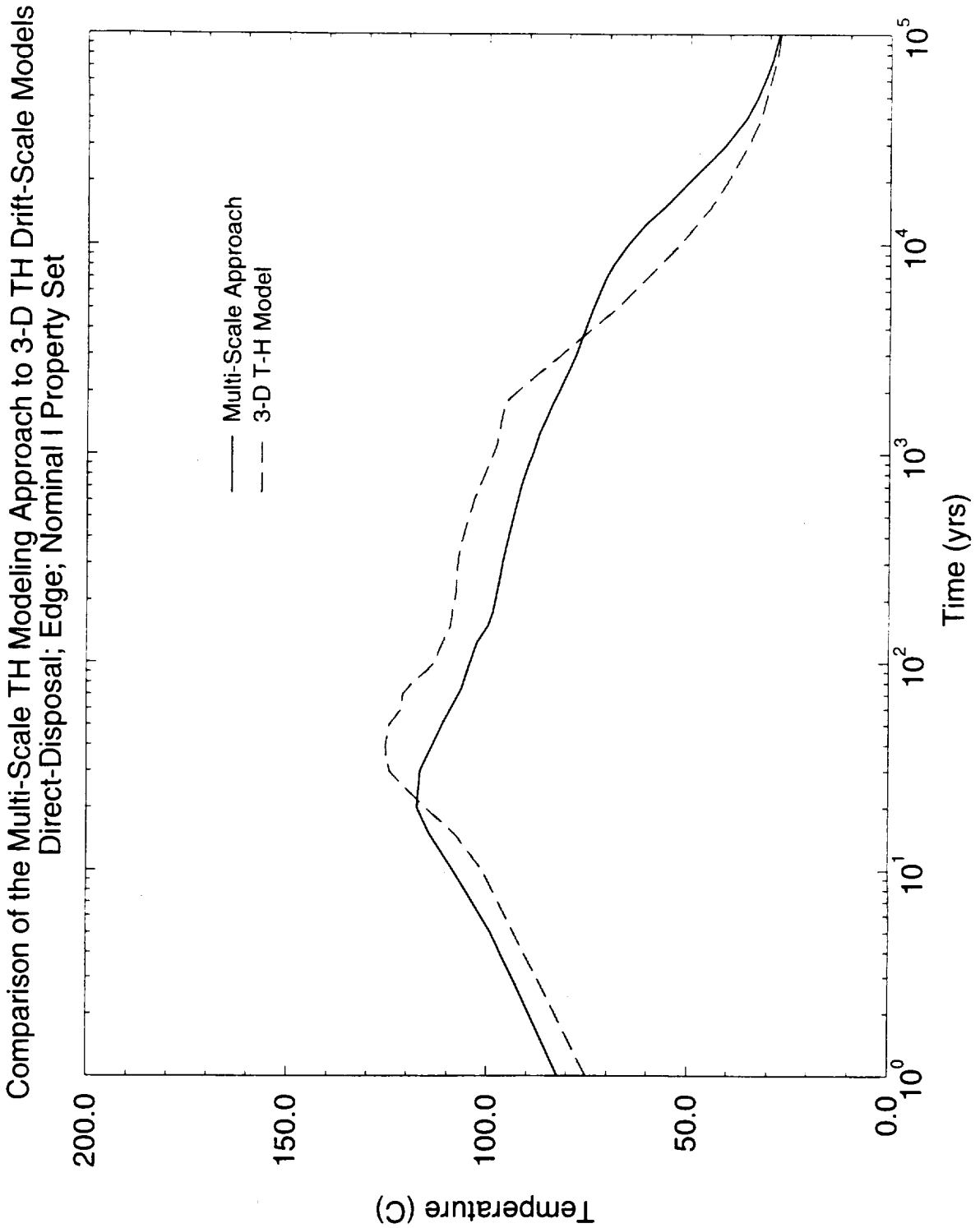

Figure 3-94. Comparison of the TH multiscale modeling and abstraction method to the PA testing models, separate disposal (or direct-disposal) waste package temperature, repository edge, present day infiltration rate.

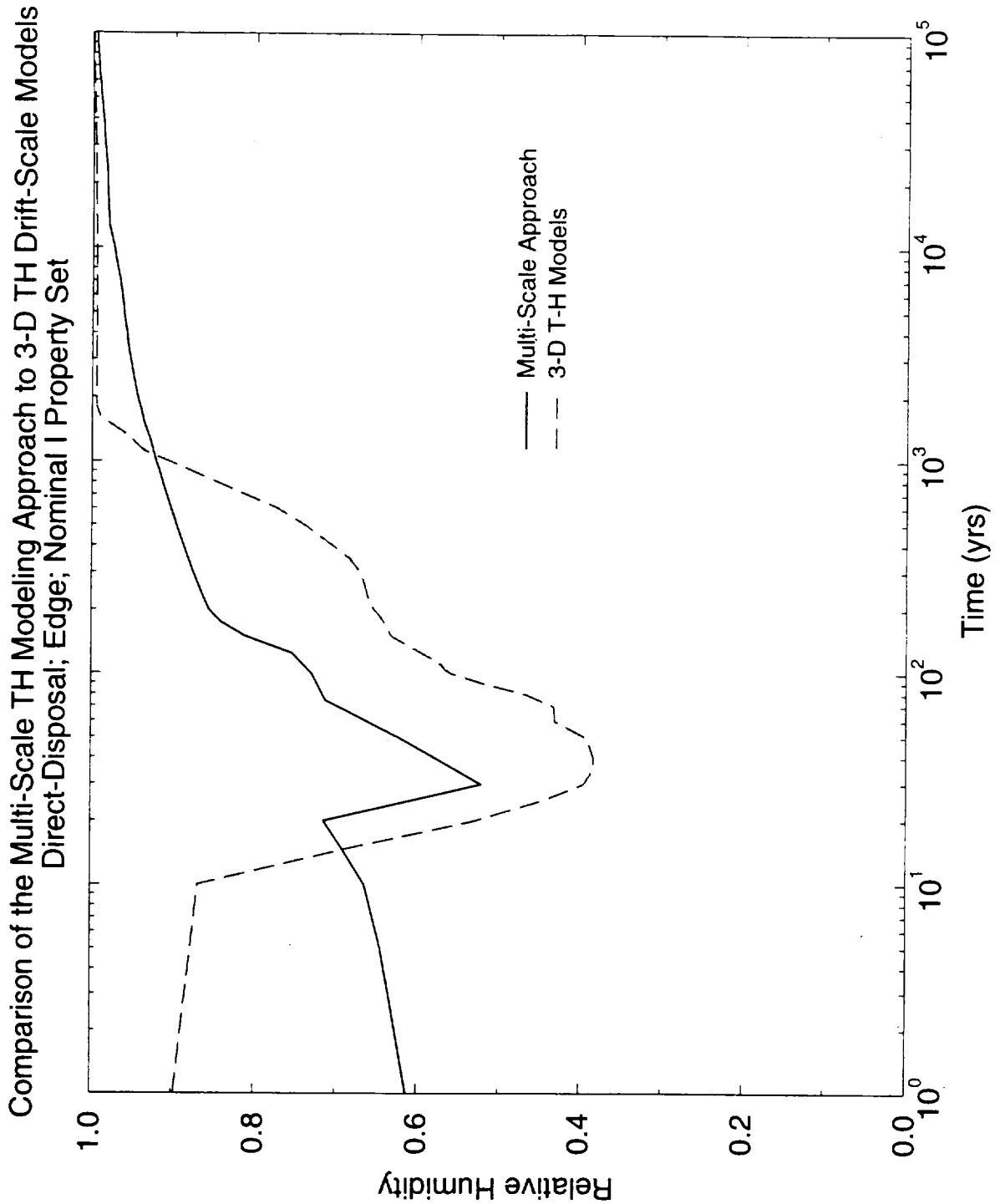

Figure 3-95. Comparison of the TH multiscale modeling and abstraction method to the PA testing models, separate disposal (or direct-disposal) waste package relative humidity, repository edge, present day infiltration rate.

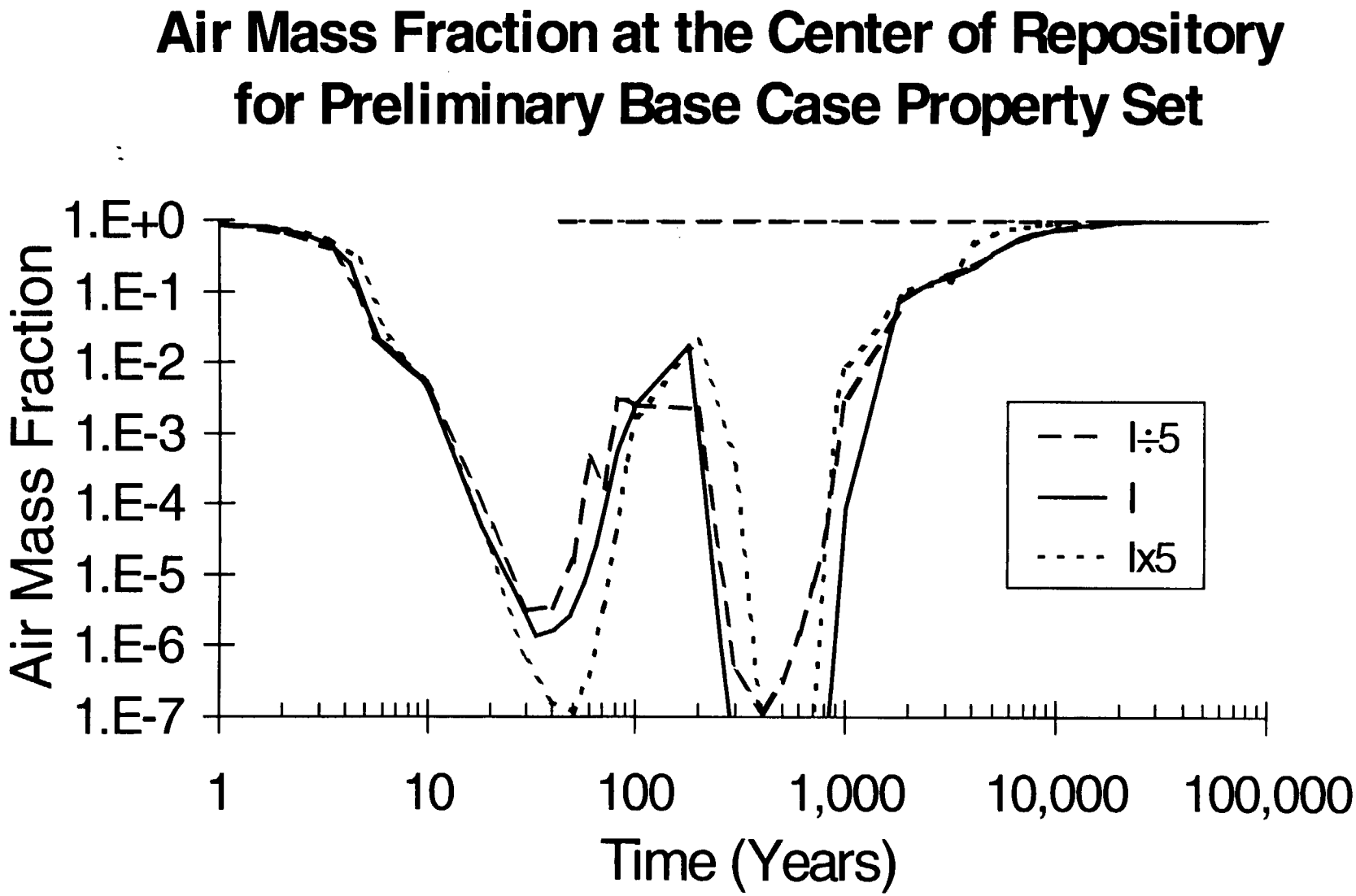

Figure 3-96. Air mass fraction at the center of the repository for the preliminary base-case property set at the present day infiltration rate.

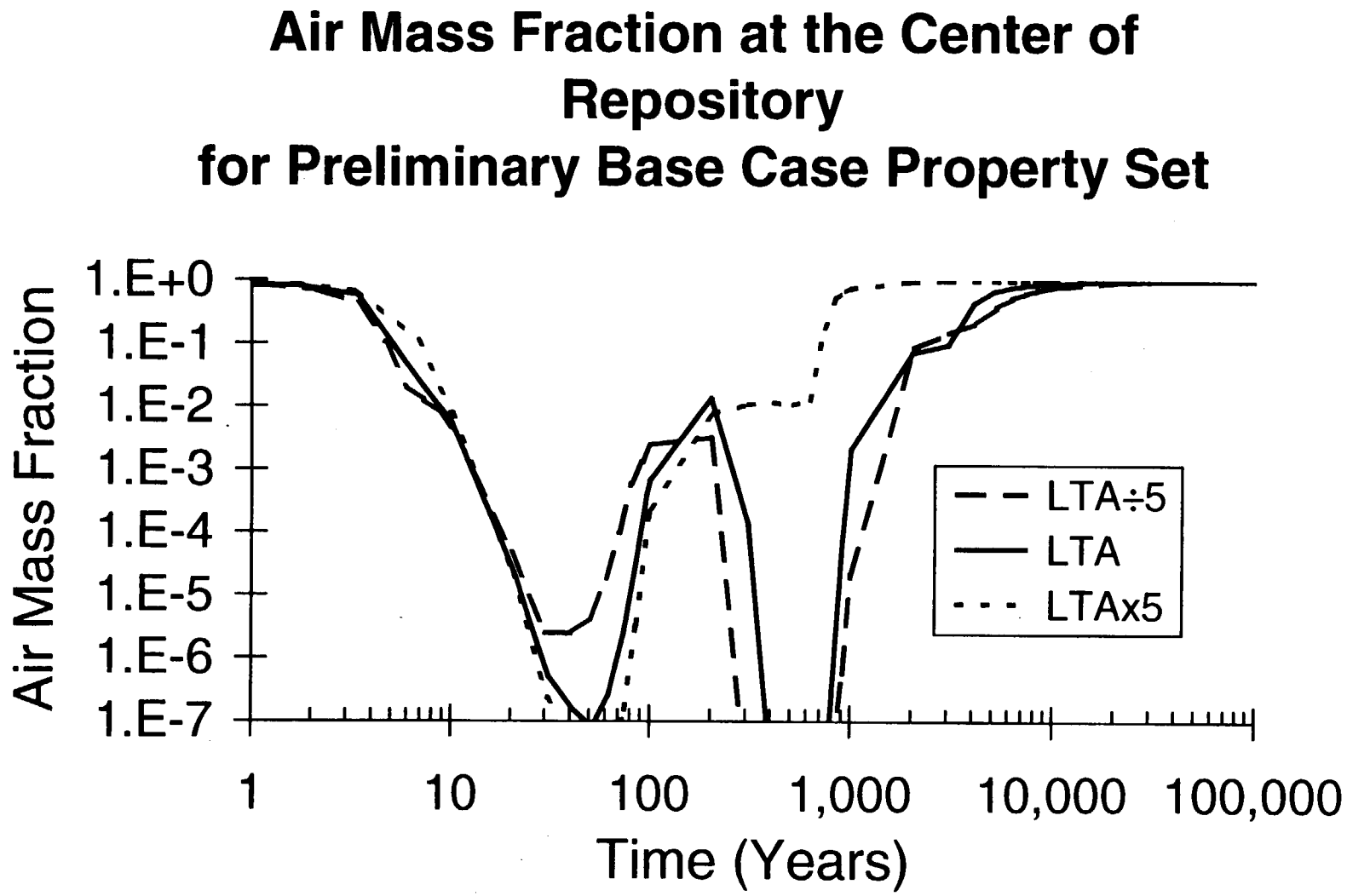

Figure 3-97. Air mass fraction at the center of the repository for the preliminary base-case property set at the long term average infiltration rate

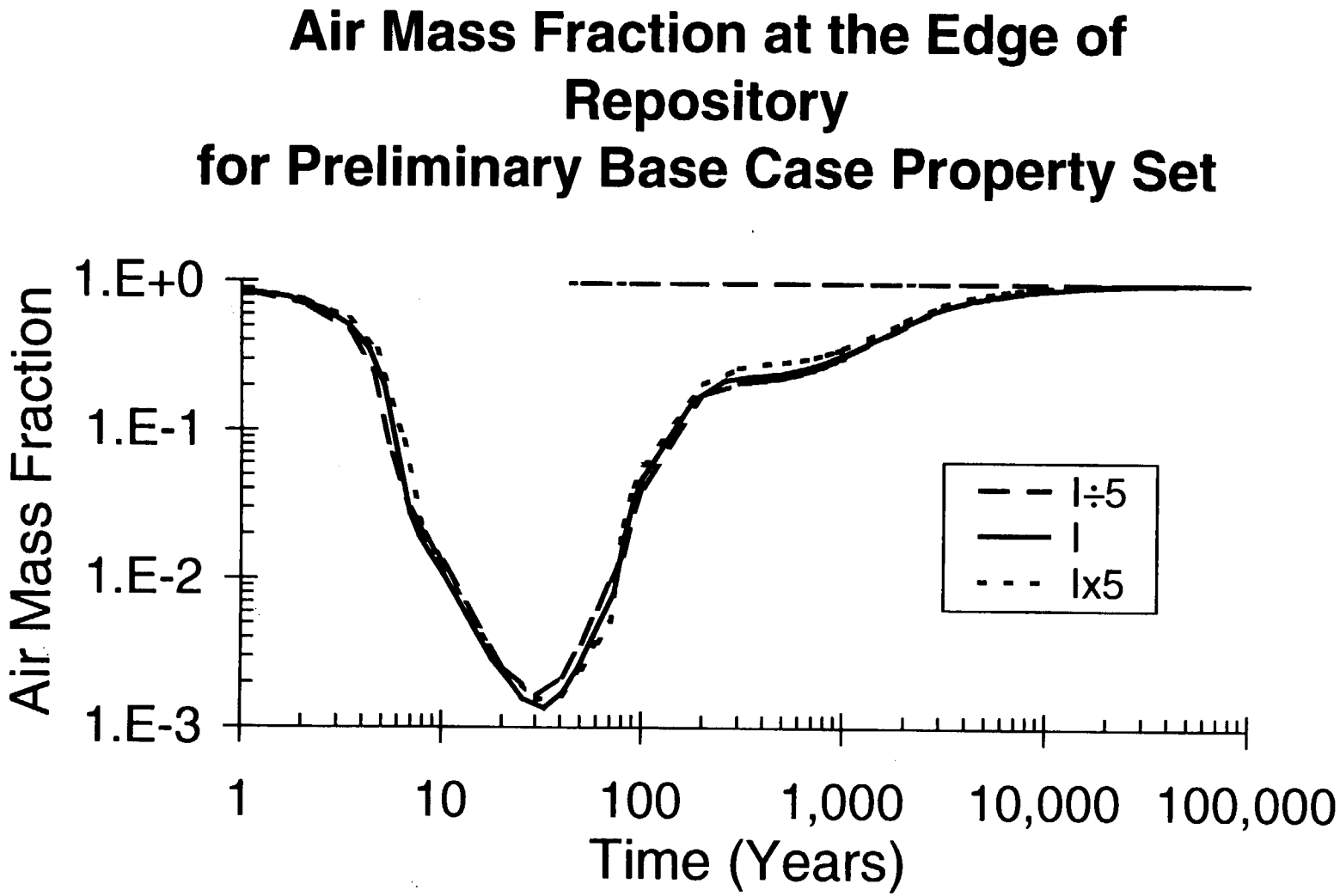

Figure 3-98. Air mass fraction at the edge of the repository for the preliminary base-case property set at the present day infiltration rate.

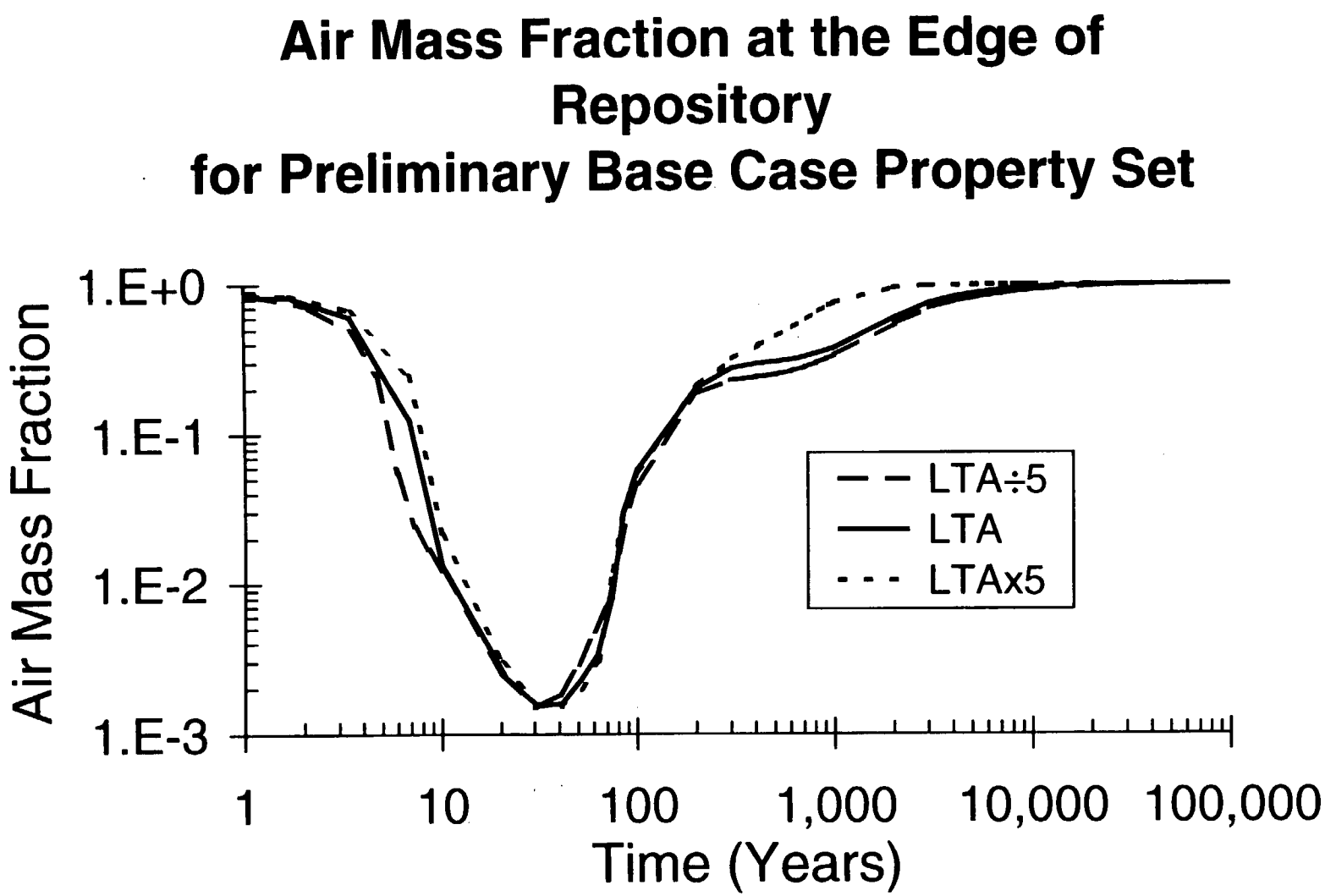

Figure 3-99. Air mass fraction at the edge of the repository for the preliminary base-case property set at the long term average infiltration rate.

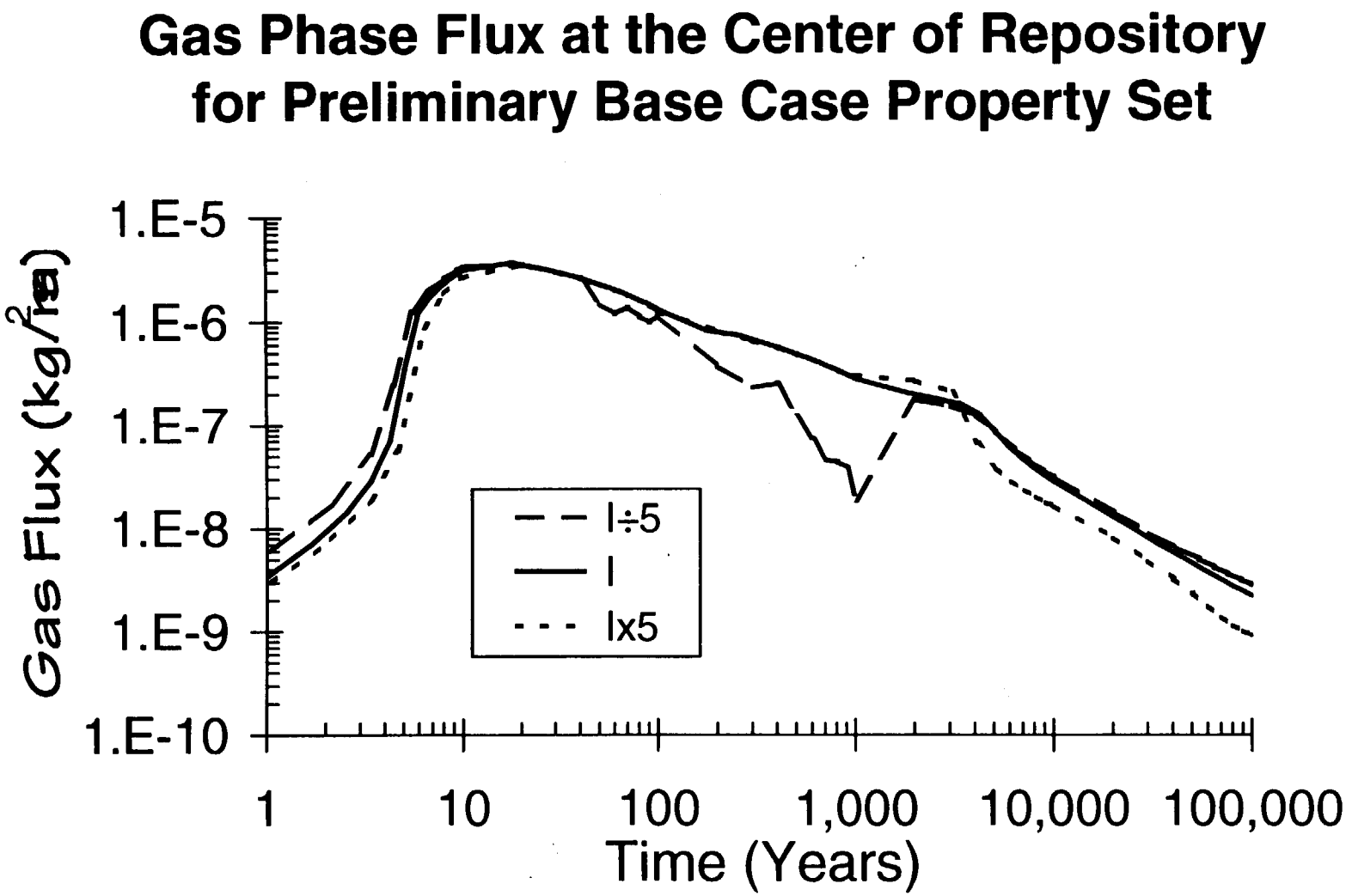

Figure 3-100. Gas flux at the center of the repository for the preliminary base-case property set at the present day infiltration rate.

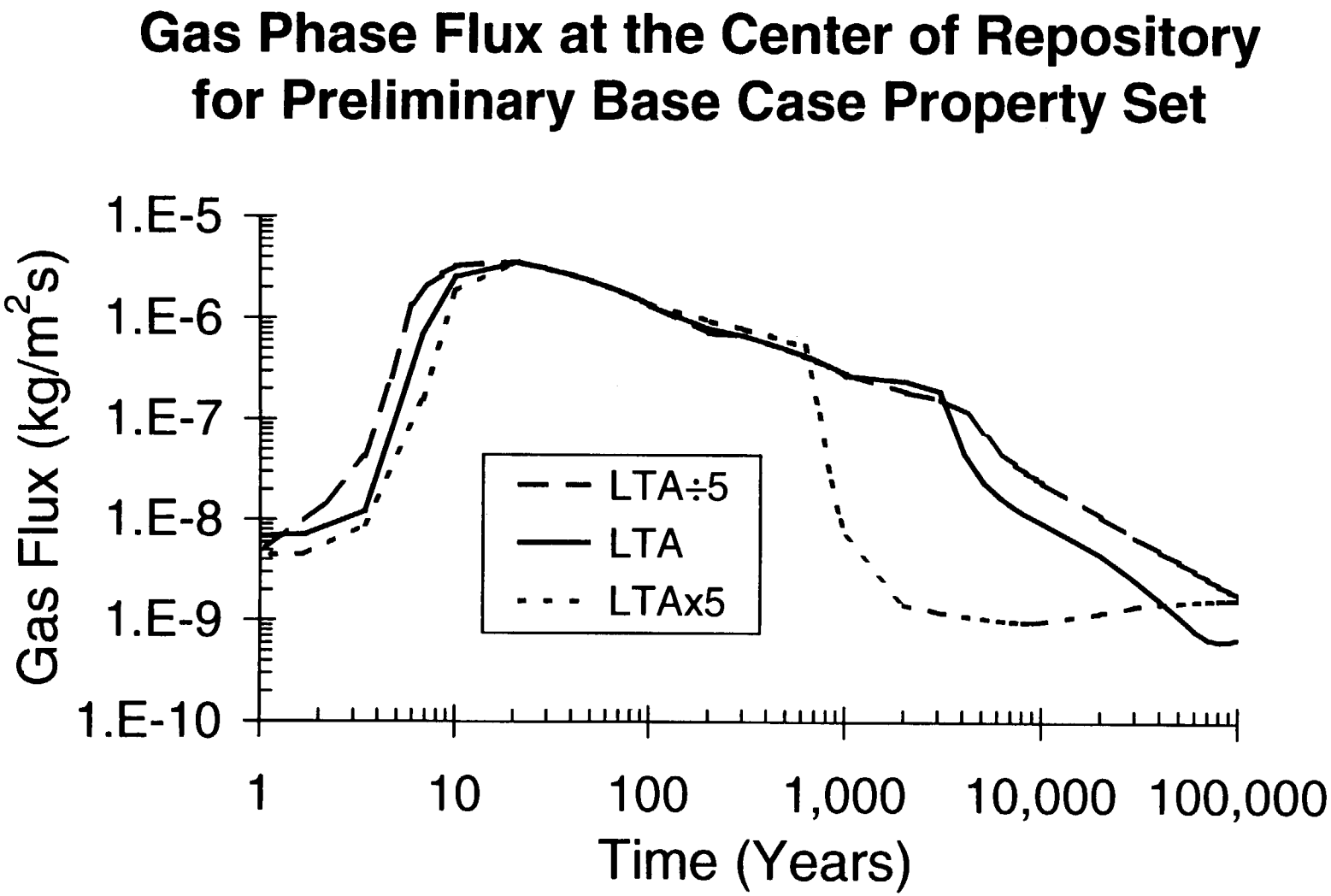

Figure 3-101. Gas flux at the center of the repository for the preliminary base-case property set at the long term average infiltration rate.

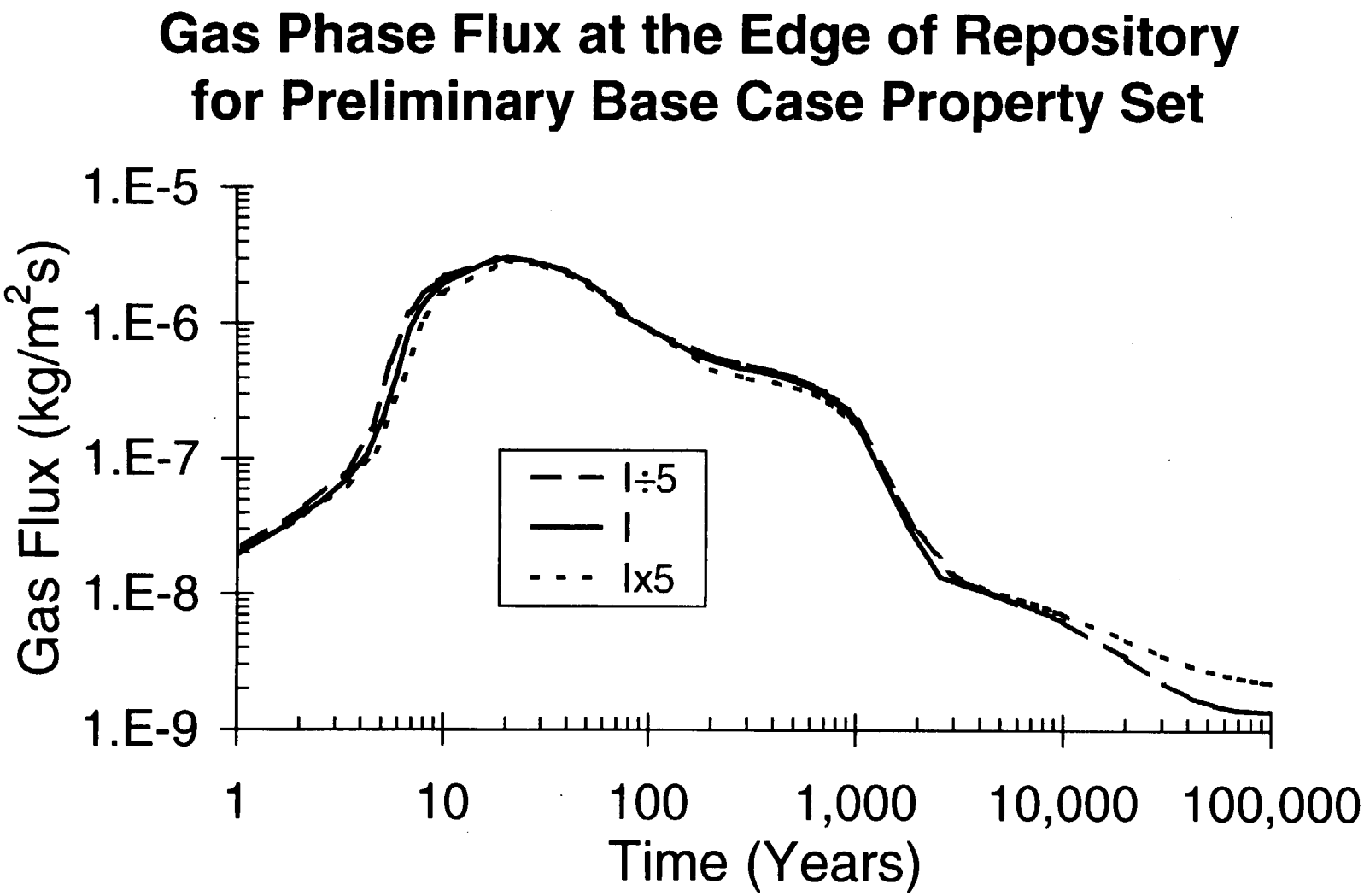

Figure 3-102. Gas flux at the edge of the repository for the preliminary base-case property set at the present day infiltration rate.

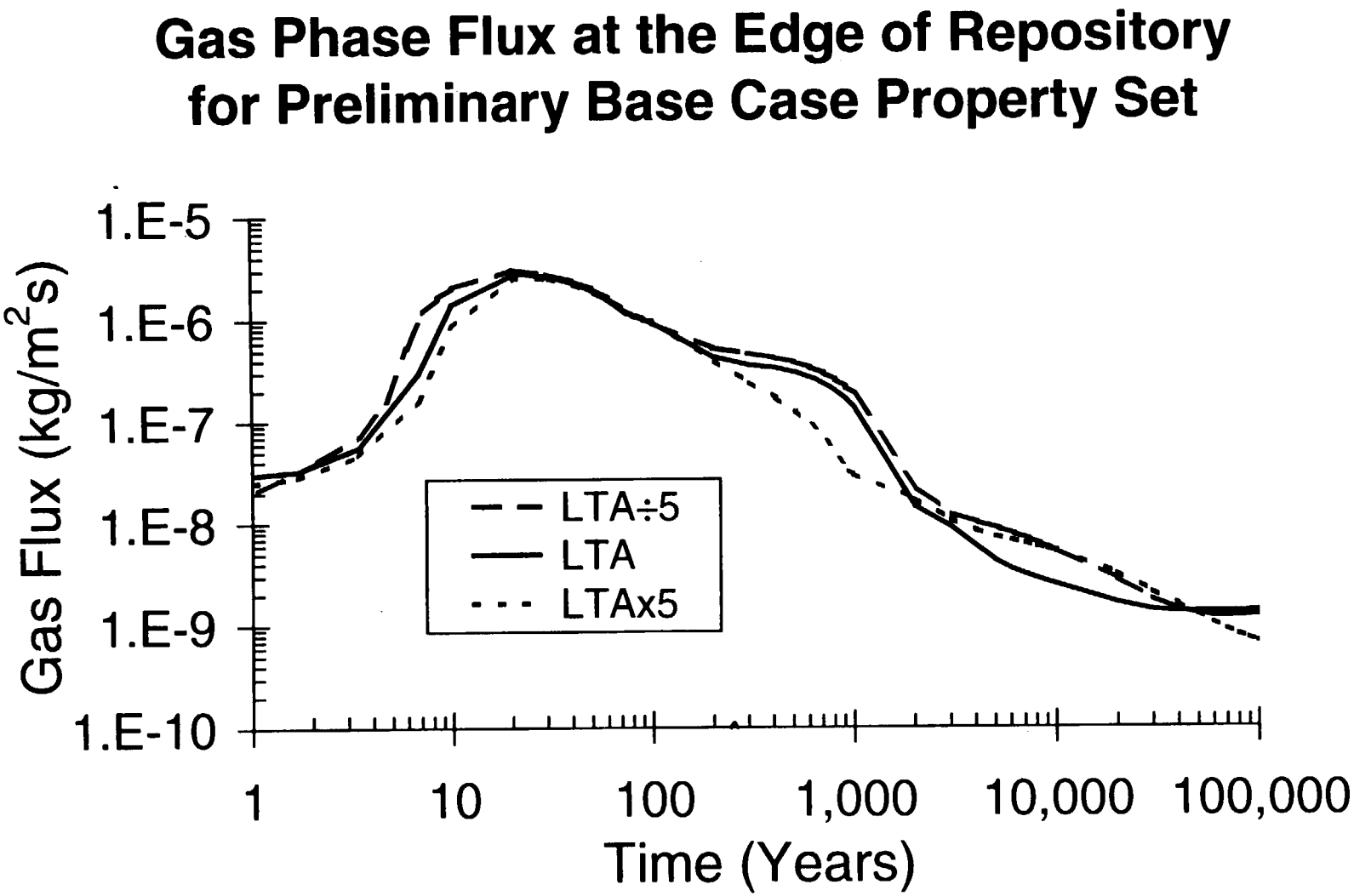

Figure 3-103. Gas flux at the edge of the repository for the preliminary base-case property set at the long term average infiltration rate.

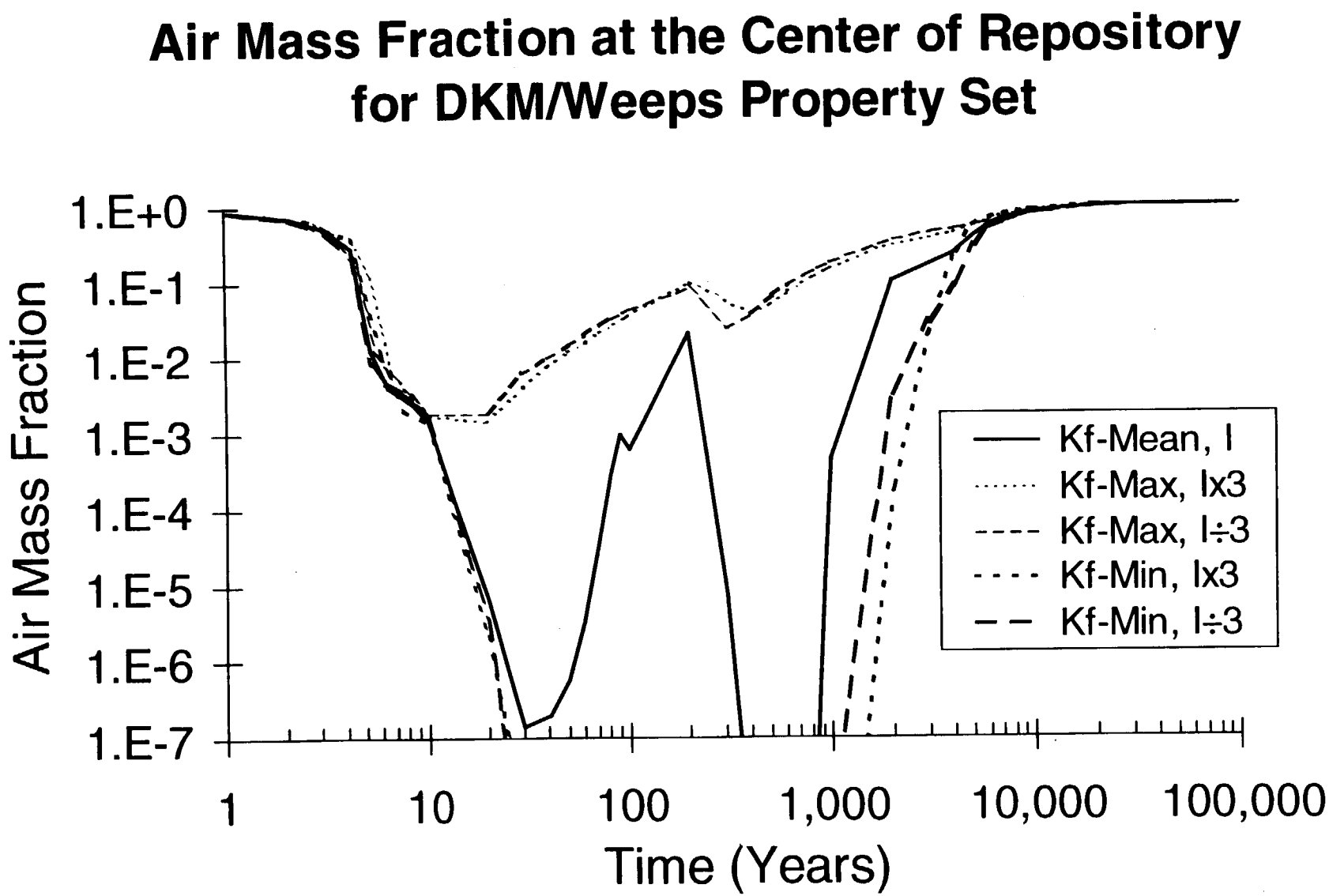

Figure 3-104. Air mass fraction at the center of the repository for the DKM/Weeps property set at the present day infiltration rate.

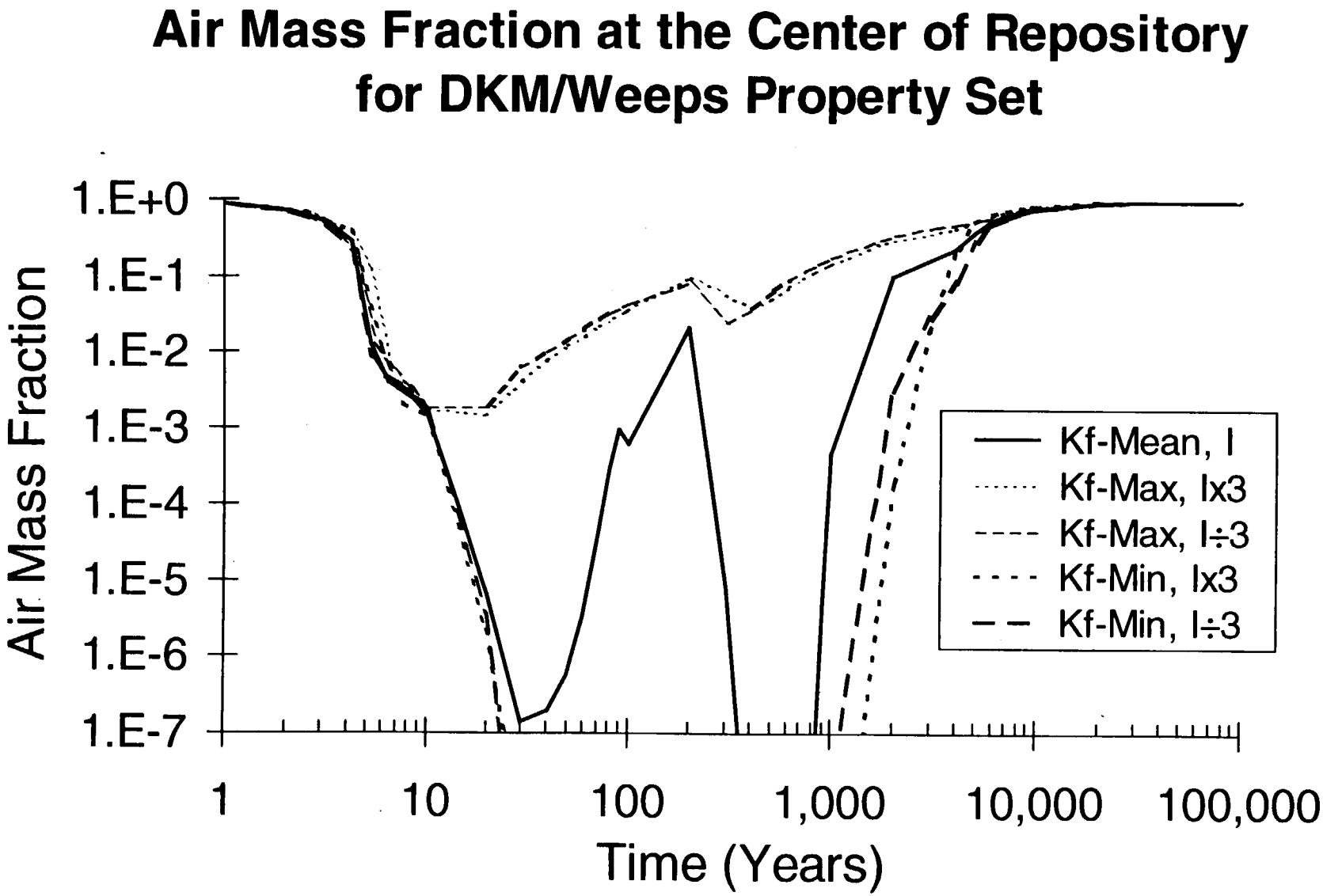

Figure 3-105. Air mass fraction at the center of the repository for the DKM/Weeps property set at the present day infiltration rate.

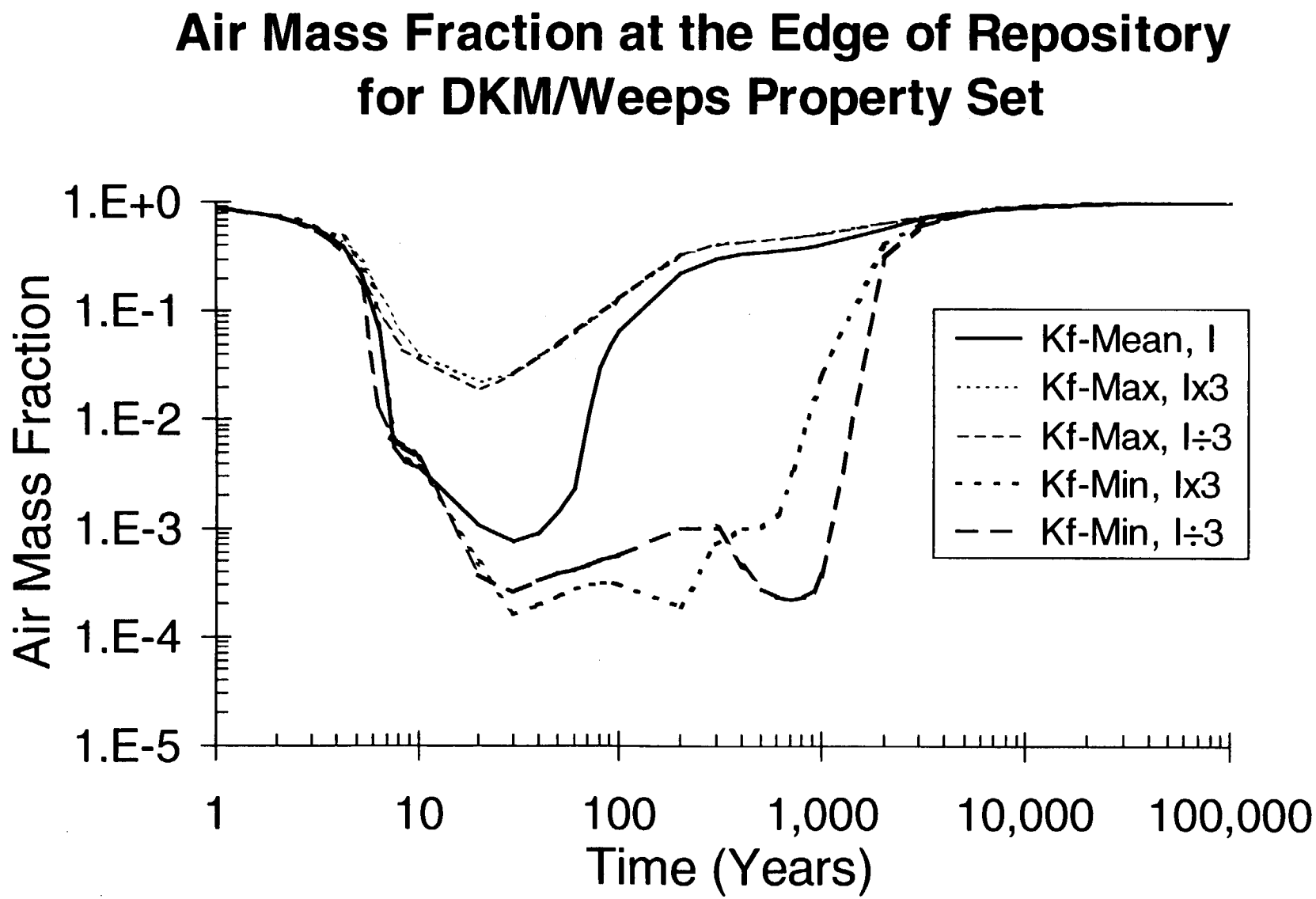

Figure 3-106. Air mass fraction at the edge of the repository for the DKM/Weeps property set at the present day infiltration rate.

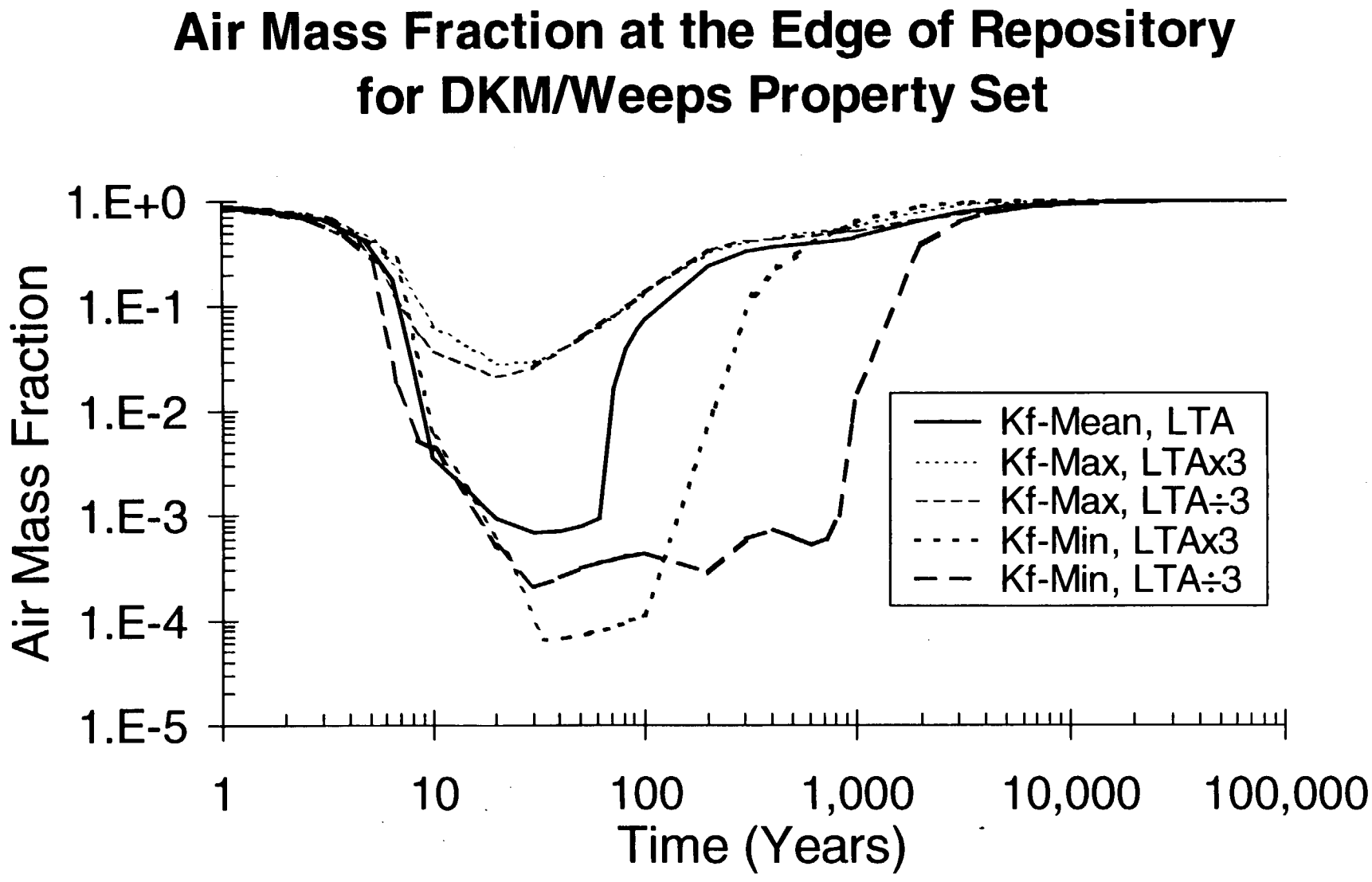

Figure 3-107. Air mass fraction at the edge of the repository for the DKM/Weeps property set at the long term average infiltration rate.

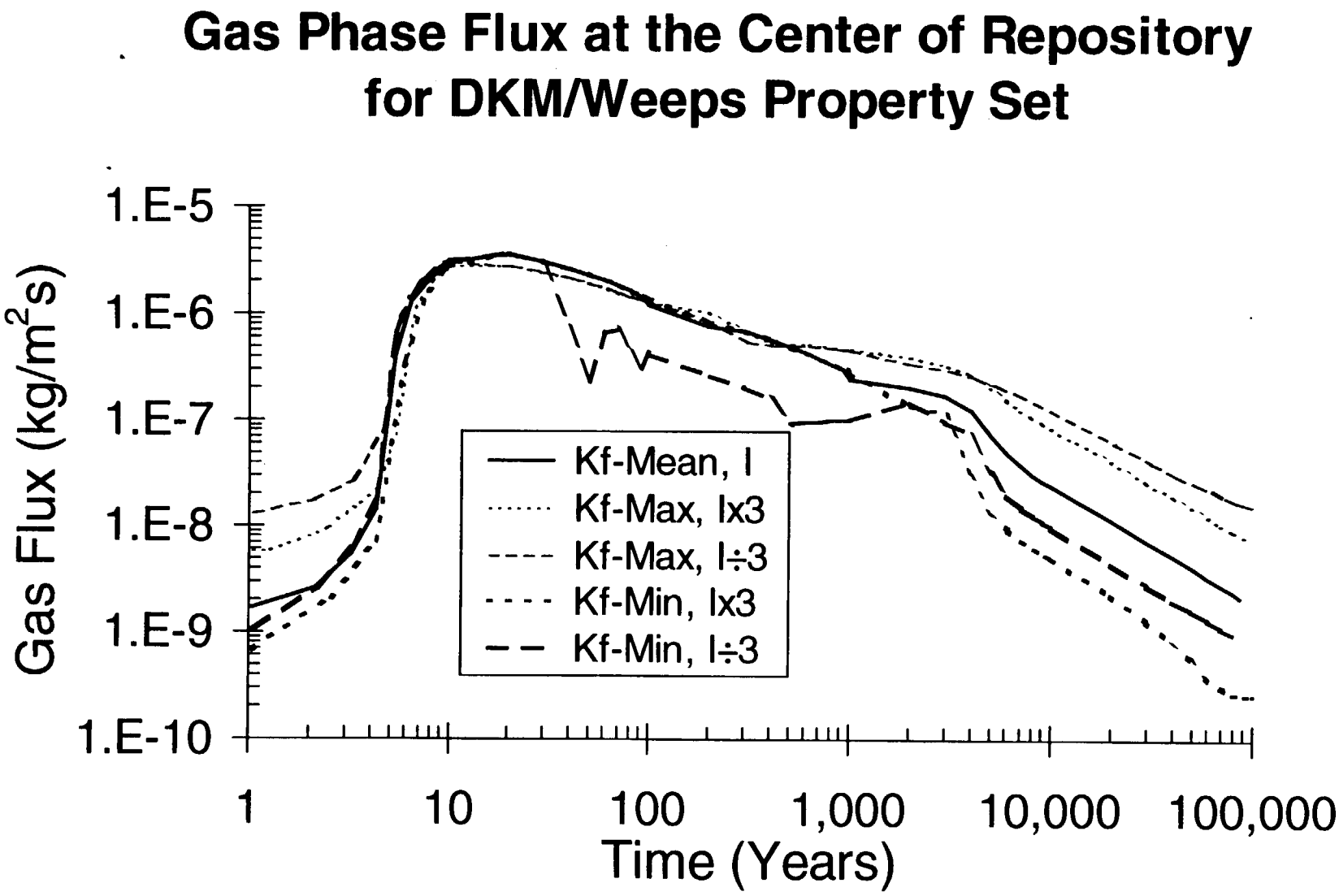

Figure 3-108. Gas flux at the center of the repository for the DKM/Weeps property set at the present day infiltration rate.

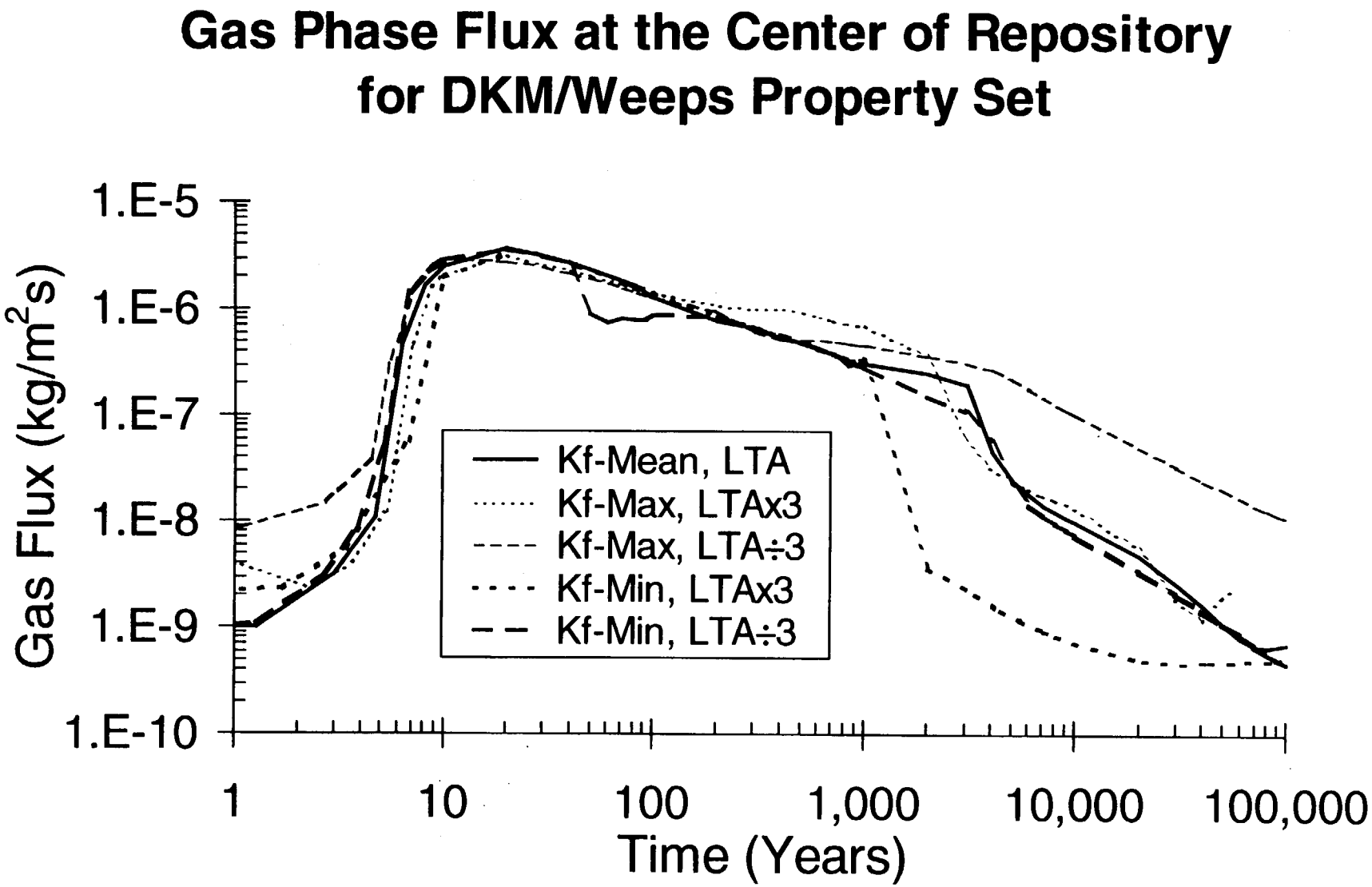

Figure 3-109. Gas flux at the center of the repository for the DKM/Weeps property set at the long term average infiltration rate.

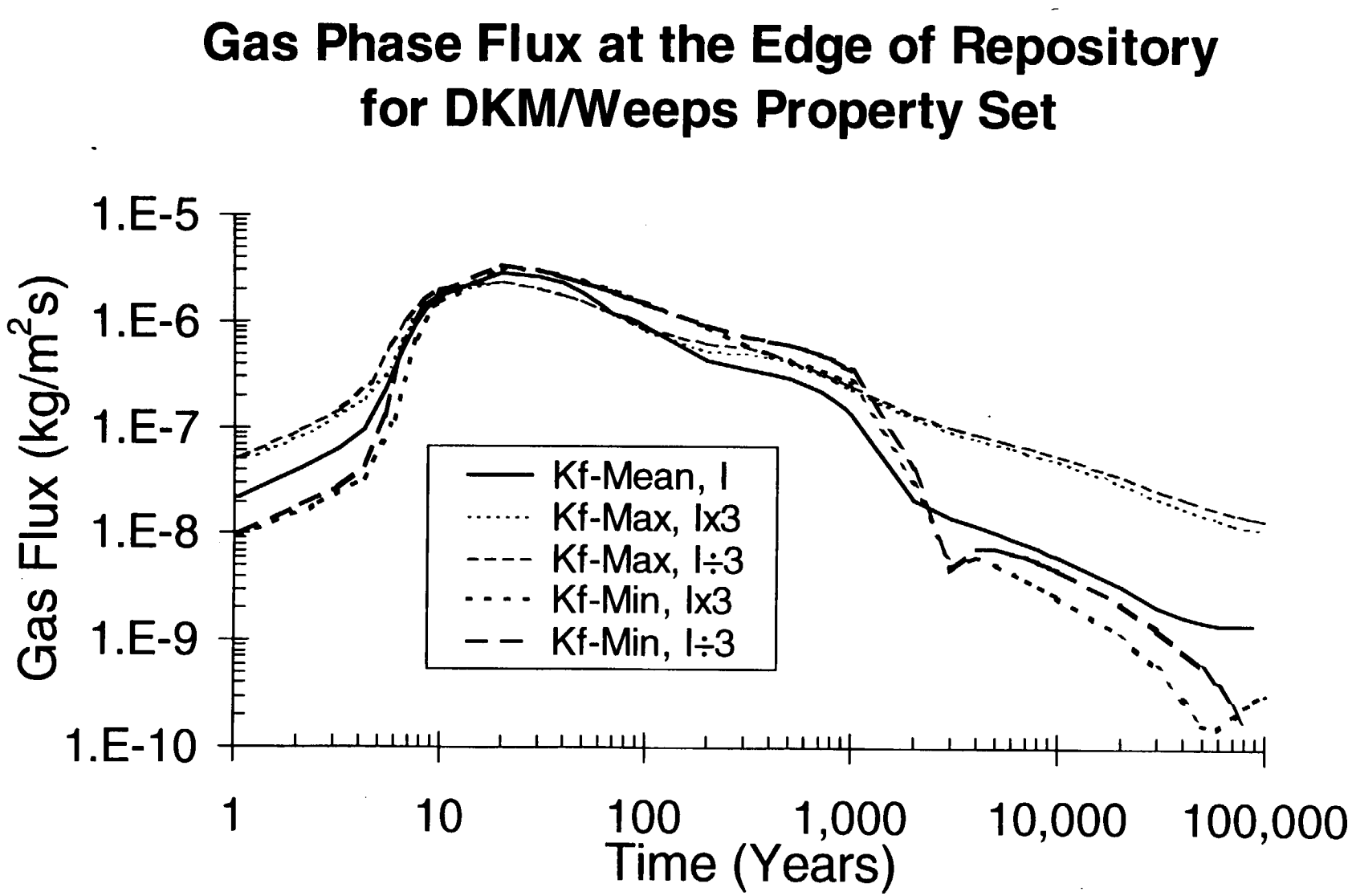

Figure 3-110. Gas flux at the edge of the repository for the DKM/Weeps property set at the present day infiltration rate.

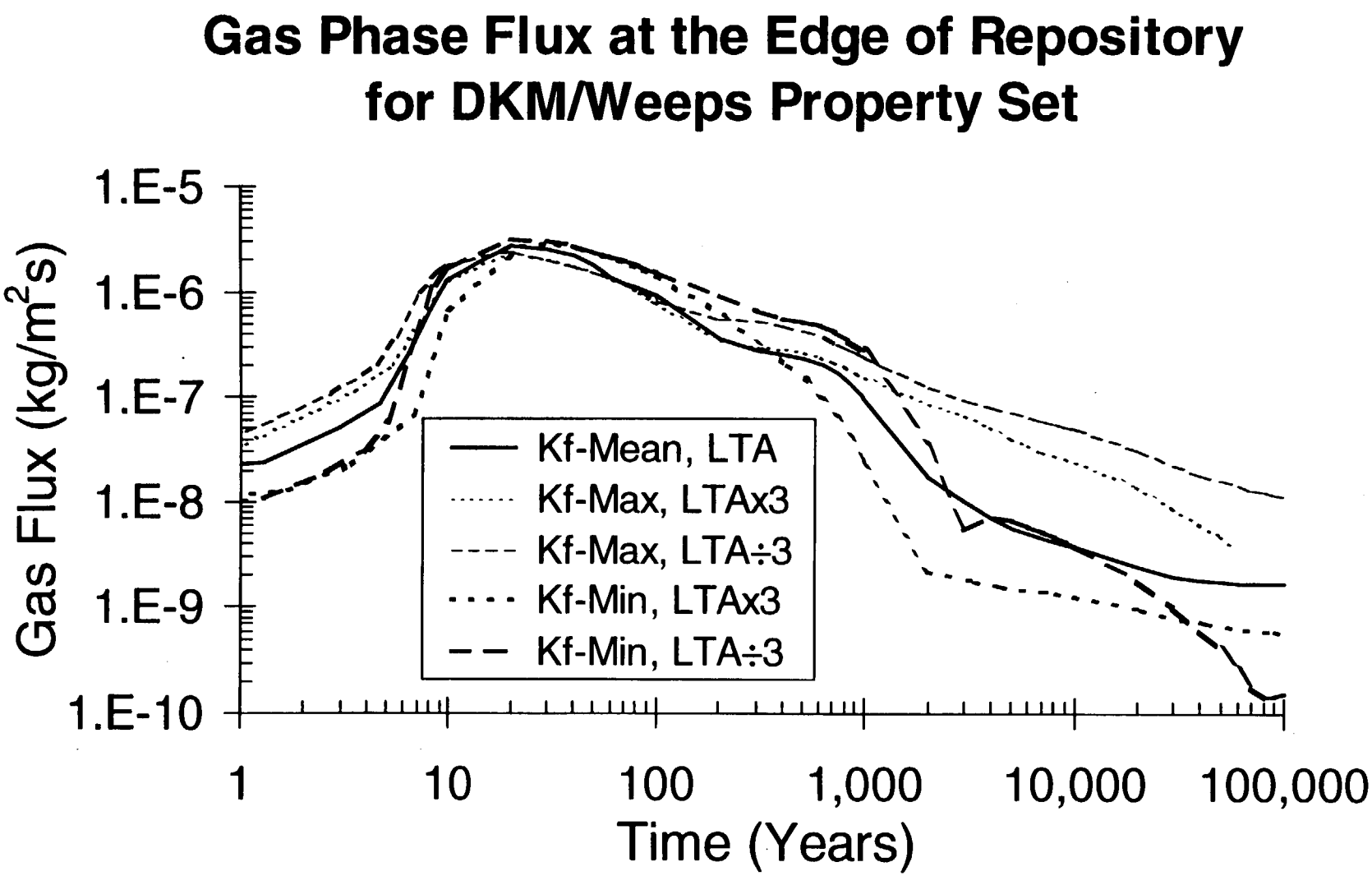

Figure 3-111. Gas flux at the edge of the repository for the DKM/Weeps property set at the long term average infiltration rate.

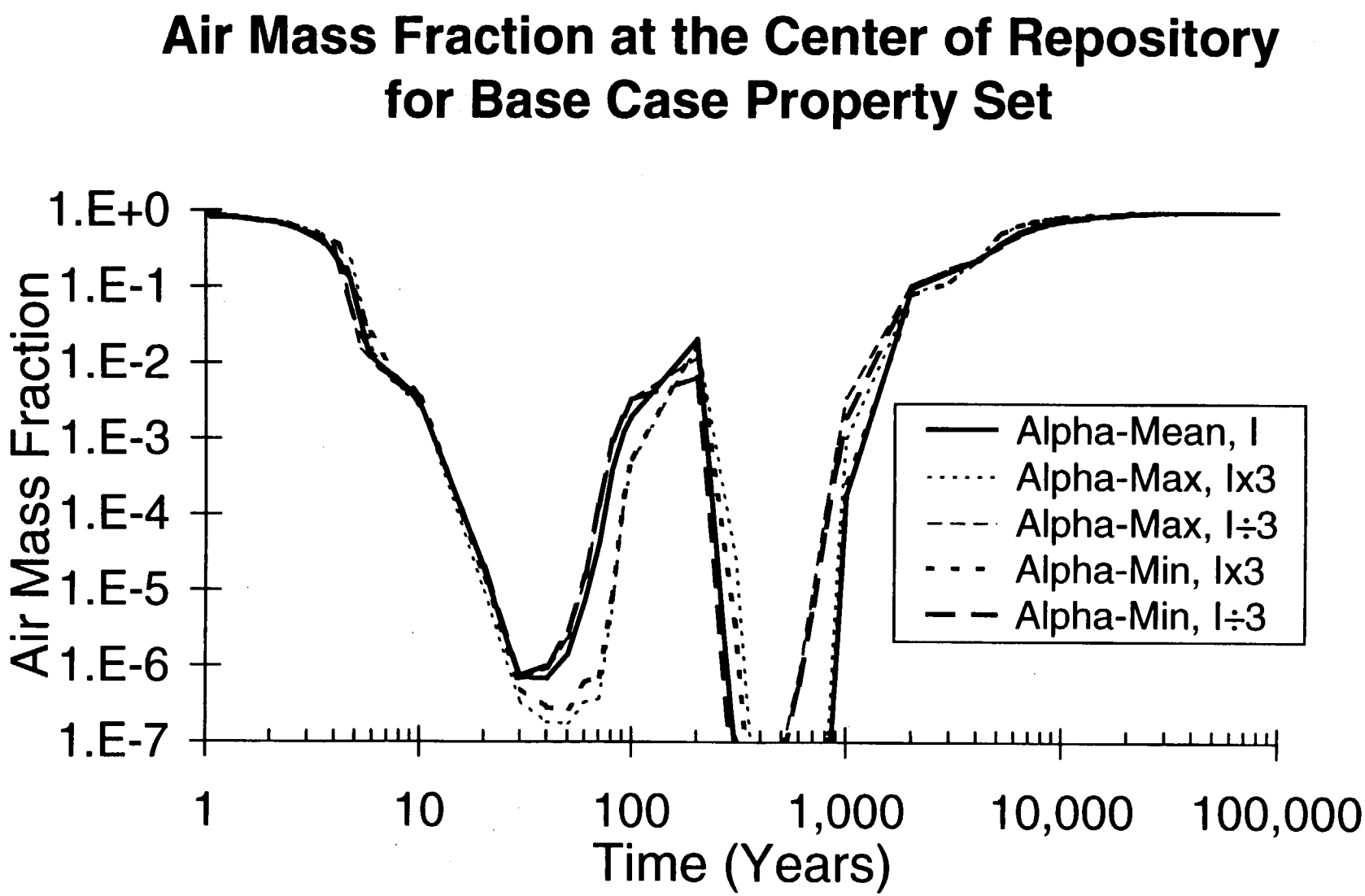

Figure 3-112. Air mass fraction at the center of the repository for the base case property set at the present day infiltration rate.